Measurement of the Double Beta Decay Half-Life of ^{100}Mo to the 0_1^+ Excited State, and ^{48}Ca to the Ground State in the NEMO 3 Experiment

Shiva King

University College London

Submitted to University College London in fulfilment of the requirements for the award of the degree of Doctor of Philosophy

October 2008

I, Shiva King, confirm that the work presented in this thesis is my own. Where information has been derived from other sources, I confirm that this has been indicated in the thesis.

Abstract

NEMO 3 is a double beta decay experiment situated in the Fréjus tunnel which runs between France and Italy. If neutrinoless double beta decay is observed it will prove the neutrino is a Majorana particle and may potentially become the most sensitive method of measuring the absolute neutrino mass. It would also have huge implications for not only particle physics, but also nuclear physics, astrophysics and cosmology. The study of two-neutrino double beta decay gives us a better understanding of the nuclear models used to calculate the nuclear matrix elements, which are so important in extracting new physics parameters from the neutrinoless double beta decay search.

The purpose of this thesis is primarily to report on the measurement of the two neutrino double beta decay of two isotopes, ^{100}Mo and ^{48}Ca, currently inside the NEMO 3 detector. The double decay of ^{100}Mo to the 0^+_1 excited state of ^{100}Ru is studied as well as the double beta decay of ^{48}Ca to the ground state of ^{48}Ti. The two neutrino half-life measurement for ^{100}Mo is found to be $T^{2\nu}_{1/2}(0^+ \rightarrow 0^+_1) = 5.70^{+1.15}_{-0.82}(stat.) \pm 0.77(syst.) \times 10^{20}$ yrs. This being the first result where all the final states have been measured. For ^{48}Ca, the two neutrino half-life is $T^{2\nu}_{1/2}(g.s. \rightarrow g.s.) = 4.44^{+0.49}_{-0.40}(stat.) \pm 0.29(syst.) \times 10^{19}$ yrs, which is the worlds most accurate measurement of this decay process. A limit on the neutrinoless double beta decay of ^{48}Ca has also been obtained.

Acknowledgements

Firstly I would like to thank Ruben Saakyan for his help and support throughout my Ph.D, I could not have asked for a better supervisor. My thanks go to Vladimir Vasiliev for his invaluable instruction in all things NEMO 3, including how to pronounce molybdenum (a crucial skill needed for my studies), to Jenny Thomas who introduced me to the NEMO 3 experiment and persuaded me to join the collaboration, and to Robert Flack to whom I gave the onerous task of proof reading this thesis. I would also like to thank all those at UCL for making my time there such an enjoyable experience, especially Simon Dean and Chris Target-Adams, not only for their assistance with ROOT, but also for their insight into life, the Universe, and everything, making them very entertaining office mates. Thanks also to Stuart Thomas and Maria Brook for their tenacious friendship; they have been such a motivational force throughout my time at UCL. And lastly my thanks go to my Mother, Father and Grandparents, especially to my Grandfather, who has always been, and continues to be a constant source of inspiration.

To Adrienne

Contents

List of Figures

List of Tables

Chapter 1

Introduction

Over the past few years the interest in neutrino physics has grown rapidly. There have been many successes, but there are still unanswered questions. One of the quests of neutrino physics is the absolute mass scale of the neutrino. Neutrinoless double beta ($0\nu\beta\beta$) decay is one of the most sensitive processes that can be used to measure the absolute mass of the neutrino, and the only practical process which can be used to determine whether the neutrino is a Majorana or Dirac particle. NEMO 3 is one of two currently running experiments searching for $0\nu\beta\beta$ decay.

The main aim of NEMO 3 is to search for the $0\nu\beta\beta$ decay process in seven different isotopes (^{100}Mo, ^{82}Se, ^{116}Cd, ^{130}Te, ^{96}Zr, ^{150}Nd and ^{48}Ca). If $0\nu\beta\beta$ decay is observed it implies that the neutrino is a Majorana particle i.e that it is its own antiparticle. It has important implications for the Standard Model of particle physics; $0\nu\beta\beta$ decay is a lepton number conservation violating process, which is forbidden by the standard model. The NEMO 3 experiment is designed to search for the effective neutrino mass down to a limit of 0.3 - 0.6 eV, which corresponds to a half-life of $\sim 2 \times 10^{24}$ yrs (90% C.L.) for ^{100}Mo.

As well as the study of $0\nu\beta\beta$ decay, it is also possible to study two-neutrino double beta ($2\nu\beta\beta$) decay with the NEMO 3 detector. The work in this thesis concentrates on the double beta ($\beta\beta$) decay of ^{48}Ca to the ground state and the $2\nu\beta\beta$ decay of ^{100}Mo to the 0_1^+ excited state. One motivation for these studies is the calculation of nuclear matrix elements for different $\beta\beta$ transitions, which have many uncertainties associated with them, in fact $0\nu\beta\beta$ experiments depend on the accurate calculation

of these parameters. Another important motivation is that the $2\nu\beta\beta$ decay of any $\beta\beta$ decaying isotope is the ultimate background for the $0\nu\beta\beta$ decay measurement, so a good knowledge of the $2\nu\beta\beta$ decay is essential for extracting the $0\nu\beta\beta$ decay half-life limit in future experiments.

1.1 Author's Contribution

- Monte Carlo simulation for several different background isotopes and different decay modes for both ^{100}Mo and ^{48}Ca.
- Reconstruction of different background isotopes and different decay modes for both ^{100}Mo and ^{48}Ca, and the measurement of internal backgrounds in ^{48}Ca.
- Co-authoring the first stage analysis programs.
- Writing all the front end results and plotting programs for the final analyses.
- Validating the external background model in the two-electron channel in the copper foil.
- Running the full analysis of ^{48}Ca, and extracting the $2\nu\beta\beta$, $0\nu\beta\beta$ decay half-lives and nuclear matrix element results.
- Running the full $2\nu\beta\beta$ analysis of ^{100}Mo to the 0^+_1 excited state and extracting the half-life and nuclear matrix element results.
- Running the $\beta\beta$ data acquisition shifts for NEMO 3.
- Running the calibration shifts for the UCL team, which take place every four weeks.

1.2 Thesis Overview

Chapter 2 contains an overview of the history of the neutrino, from its inception through to the experimental achievements of the present day. This leads on to Chapter 3 which describes neutrino nature, mixing, and oscillations and gives an overview of neutrino mass measurement experiments, including a more detailed look

at some of the experiments introduced in Chapter 2. Chapter 4 details the various modes of double beta decay and gives a review of some of the main double beta decay experiments: past, present and future.

Chapter 5 contains a description of the NEMO 3 detector. As well as the four main parts of the dectector, the tracker, calorimeter, source foils and passive shielding, it also includes a description of the electronics, and the energy and time calibration. Chapter 6 describes the types of backgrounds considered in the NEMO 3 experiment. Chapter 7 begins with an overview of the NEMO 3 data analysis process, it also includes a description of particle identification using the NEMO 3 detector and preselection criteria for various topological signatures. Details of the external background model, including the two electron channel analysis in the copper foils, follow.

Chapter 8 begins with an overview of ^{48}Ca $\beta\beta$ decay experiments and results, which is followed by internal background analysis. The last part of this chapter contains the $2\nu\beta\beta$ and $0\nu\beta\beta$ decay analysis of ^{48}Ca, including half-life and nuclear matrix element results. Chapter 9 also begins with an overview of previous experiments and results and after a discussion on the analysis, the $2\nu\beta\beta$ decay of ^{100}Mo to the 0_1^+ excited state half-life and nuclear matrix element results are given. And finally Chapter 10 contains a discussion and summary of results.

Chapter 2

The History of the Neutrino

2.1 Introduction

To explain the history of the neutrino, first we have to understand why scientists pondered its existence at all. Before the neutrino comes the beta decay problem; radioactivity had to be discovered before the neutrino was a twinkle in Wolfgang Pauli's eye.

This chapter is an overview of discoveries and experiments pertinent to the history of the neutrino, and as such many of the experiments introduced below will be discussed in further detail in the following chapters.

2.2 The History Before History

In March 1896 Henri Becquerel, spurred on by the research into X-rays by Wilhelm Roentgen, discovered radiation coming from uranium salts. He later showed the radiation emitted from uranium comes from charged particles. Two years later, in 1898, Pierre and Marie Curie (who coined the term radioactive) isolated radium, a much more potent radioactive source than uranium. In 1903 Henry Becquerel, and Pierre and Marie Curie were awarded the Nobel prize in physics for their work on radioactivity.

In 1899 Rutherford showed that two types of radiation exist, alpha (α) and beta (β) and one year later, Villard gave evidence of a third type of radiation coming

from radium, which he called gamma (γ) radiation. Finally three types radiation are defined:

- α - ^{4}He nucleus emitted from nucleus
- β - electrons emitted from nucleus
- γ - photons emitted from nucleus

For β decay scientists assumed the decay spectrum would be the same as the definite peaks seen in the α and γ decay spectra, but after studies by Lise Meitner and Otto Hahn, in 1914, James Chadwick showed the β decay spectrum is continuous. Charles Drummond Ellis then clearly established the behaviour of the β decay spectrum during several years of study from 1920-1927, ending all controversy.

Wolfgang Pauli postulated the existence of the neutrino in a letter dated 4th December 1930, stating that an electrically neutral particle would account for the continuous β decay spectrum. And in 1933 Enrico Fermi wrote down the correct theory for β decay, incorporating and naming the neutrino [1].

2.3 The Majorana Years

Maria Goeppert-Mayer was the first to consider $\beta\beta$ decay in her paper of 1935 [2], acknowledging Eugene Wigner with suggesting the problem. And in 1937 the young Ettore Majorana published his theory on neutrinos, stating that neutrinos and antineutrinos are the same particle and suggesting an experiment to test his theory [3]. There then followed a succession of papers from Racah, Furry and Primakoff formulating $0\nu\beta\beta$ decay theory.

Guilio Racah was the first to suggest using $0\nu\beta\beta$ decay to test Majorana's theory [4], and in 1939 Wendell Hinkle Furry calculated the transition probabilities for the decay [5]. In 1952 Henry Primakoff used Majorana's theory of neutrinos to calculate the electron-electron angular correlations and the electron spectra, making a clear distinction between the $2\nu\beta\beta$ decay and $0\nu\beta\beta$ decays [6].

2.4 The Neutrino Reines

After their first attempt in 1952 [7], Frederick Reines and Clyde Cowan made the first detection of a neutrino from the Savannah River Nuclear Plant, using a target of water and cadmium chloride in 1956 [8]. In 1957 Bruno Pontecorvo proposed neutrino-antineutrino oscillations [9], and then in 1962 Ziro Maki, Masami Nakagawa and Shoichi Sakata introduced the theory of neutrino flavour mixing and flavour oscillations [10].

1962 was a busy year for neutrinos as Leon Lederman, Melvin Schwartz and Jack Steinberger, proved more than one flavour of neutrino exists, by identifying the muon neutrino at the Brookhaven National Laboratory [11], for which all three won the Nobel Prize for Physics in 1988. Three years later in 1965, Reines did it again and observed the first atmospheric neutrinos in the East Rand gold mine in South Africa using a large area liquid scintillator detector [12]. At the same time, Goku Menon and colleagues make the same discovery in the Kolar Gold Fields Mine in India using a tracking detector with neon flash tubes and scintillators [13].

Using a 10,000 gallon tank filled with perchloroethylene, a common dry cleaning fluid, Ray Davis (with John Bahcall working on the theory behind the experiment) obtained the first radio-chemical results for solar neutrinos at the Homestake mine in South Dakota in 1968 [14]. Davis found a third of the expected neutrinos. This discrepancy between theory and experiment became known as the "solar neutrino problem" and remained a neutrino puzzle for many years to come.

2.5 Light at the End of the Tunnel

The early 80's saw the building of two atmospheric neutrino experiments; the Irvine Michigan Brookhaven (IMB) experiment and the Kamioka Nucleon Decay Experiment (KamiokaNDE). The IMB was built in the Morton salt mine, near Cleveland Ohio, and KamiokaNDE was built in the Mozumi mine in Japan. Both experiments observed the atmospheric anomaly in 1985, but final results of the experiments were not published till later [15], [16]. Later the same year KamiokaNDE was upgraded (to improve background rejection) to Kamiokande II, and within the

next two years had made the first direct counting observation of solar neutrinos, confirming the deficit seen by Ray Davis twenty years earlier [17]. Both Ray Davis and Matatoshi Koshiba, leader of the Kamiokande collaboration received the Nobel Prize in Physics in 2002 for their work on solar neutrinos.

On February 23rd 1987 the blue supergiant, Sanduleak-69d 202a, exploded in the Large Magellanic Cloud ∼50 kpc away from Earth. Four detectors claimed to observe the neutrino burst from the type-II Supernova: KamiokaNDE [18], [19], IMB [20], the Baksan detector [21], and the Mont Blanc detector [22]. The Mont Blanc observation was later discounted as it was recorded five hours before all of the other experiments. All in all 24 events were observed, 11 from KamiokanNDE, 8 from IMB and 5 from Baksan, essentially opening up the new field of research in neutrino astronomy, and providing valuable information on neutrino properties.

In 1989 both SLC (SLAC Linear Collider) [23] and LEP (Large Electron Positron collider) [24] produced almost simultaneous results from studying the Z boson, constraining the number of light neutrino families in the Standard Model of particle physics (SM) to three. The reference given here for LEP is from ALEPH (Apparatus for LEP PHysics), but all four of the LEP detectors produced very similar results.

Another experiment based in Kamioka, Japan is Super-Kamiokande (Super-K). Super-K is a large water Cerenkov detector located 1000 m underground at the Mozumi Mine. Beginning operation in 1996, after just two years in July 1998, the Super-K collaboration announced the first evidence that neutrinos have mass from the observation of atmospheric neutrinos [25].

DONUT (Direct Observation of NU Tau) was set up to search for the tau neutrino utilising the Tevatron beam at Fermilab. The detector began taking data in the summer of 1997, and although it only ran for a few months it was extremely successful. It took three years to trawl through the data, but in July 2000 the DONUT collaboration announced the discovery of the tau neutrino therefore confirming the third neutrino flavour predicted by LEP and SLC [26].

SNO (Sudbury Neutrino Observatory) was a solar neutrino experiment based in the Creighton Mine in Sudbury, Canada. SNO started taking data in 1999 and

by 2001 had published the results of the first convincing evidence of solar neutrino oscillations, providing the solution to the solar neutrino problem [27]. SNO finished taking data in 2006 and throughout its operation continued to improve and consolidate the published result in 2001.

The first detection of a deficit of reactor neutrinos was found by KamLAND (Kamioka Liquid scintillator AntiNeutrino Detector). KamLAND was built inside the old KamiokaNDE cavity at the Kamioka Observatory in Japan, and designed to detect electron antineutrinos from nuclear reactors surrounding it. KamLAND started in January 2002 and after just 145 days of data taking, the collaboration reported its first results [28]. This result was confirmed after only 515 days of data taking [29].

2.6 Are We There Yet?

The neutrino has been on quite a journey. From its unassuming beginnings in 1930, it has taken less than 100 years for this particle to captivate the minds of scientists, and has kept company with many Noble Prize winners.

We still know very little about this particle. It has transformed from a massless particle used to explain an apparent anomaly in the β decay spectrum, to become a main subject area of research all over the world. It has gained mass, and with it an unequivocal place in scientific history.

Are we there yet? Well not quite. We have gained valuable knowledge, but there is still so much to be discovered, and the next ten years of research will undoubtedly shed more light on this elusive particle.

Chapter 3

The Physics of Neutrino Masses

3.1 Introduction

Neutrinos are weakly interacting, spin 1/2 particles, with no charge and a very small mass. As mentioned in the previous chapter, the LEP and SLC analyses of the Z-boson width has shown that there are three types or flavours (ν_e, ν_μ, ν_τ) which are linear combinations of states with a well defined mass. It is possible that there are more massive neutrino states, but these states must be sterile (a neutrino that only interacts with matter through gravity) or have the neutrino mass $m_\nu > m_z/2$, so as not to disagree with the LEP and SLC results.

Oscillation experiments (solar, atmospheric, reactor and accelerator) have shown that neutrinos mix and therefore have mass. Experiments that make a kinematical measurement of the end point energy of the β decay spectrum, most typically tritium beta decay experiments, and, if the neutrino is a Majorana particle, $0\nu\beta\beta$ experiments, go a little farther into probing the absolute mass of the neutrino. These experiments, if successful, will also shed light on the possible mass hierarchies, not to mention new physics beyond the SM as we know it today. It is worth mentioning, as neutrinos are playing a larger role in cosmology, that another possible way to measure the total neutrino mass (and therefore complementary to the beta decay experiments) is through cosmological experiments such as WMAP (Wilkinson Microwave Anisotropy Probe).

This chapter reviews the properties of the neutrino, what is currently known

about the neutrino, and properties of the neutrino that have yet to be measured. Sec. 3.2 describes the possible nature of the neutrino; Sec. 3.3 neutrino masses, mixing and oscillations; and Sec. 3.4 reviews neutrino mass measurement experiments.

3.2 Neutrino Nature

The importance of different aspects of neutrino physics is somewhat subjective, but it seems that the two most fundamental issues facing neutrino physics at the moment are questions of the nature of the neutrino (whether it is a Dirac or Majorana particle) and its absolute mass scale (and connected to that the smallness of the neutrino mass compared to the masses of other particles). At this point it is important to note that $0\nu\beta\beta$ experiments could address both these issues. $0\nu\beta\beta$ experiments are also the only practical test of the nature of the neutrino. If $0\nu\beta\beta$ experiments are successful and the neutrino is proved to be a Majorana particle, it would have a profound effect on not just particle physics theory. A Majorana neutrino would have implications for GUTs, early Universe theories (i.e. leptogenesis) and supersymmetry [30].

The fundamental difference between Majorana and Dirac particles is that Majorana particles (such as the neutral pion) are identical to their own antiparticles, and Dirac particles are distinct from their antiparticles. The neutrino is the only fundamental fermion that can be a Majorana particle, as all other fermions having a charge and a magnetic moment have a distinct antiparticle.

3.3 Neutrino Mixing, Masses and Oscillations

In 1957 Pontecorvo first introduced the idea of neutrino oscillations [9]. He realised that if neutrinos have mass, there could be a process whereby neutrino flavour is not conserved. His theory has been extremely successful and will be discussed in more detail in the following section. Pontecorvo's work was followed by Maki, Nakagawa and Sakata in 1962 [10] who proposed the idea of *true neutrinos* (ν_1, ν_2) based on the two neutrino hypothesis, where the *weak neutrinos* (ν_e, ν_μ) are mixtures of true neutrinos, what is now known as neutrino mixing,

$$\nu_e = \cos\theta\nu_1 - \sin\theta\nu_2 \tag{3.1}$$

$$\nu_\mu = \sin\theta\nu_1 + \cos\theta\nu_2 \tag{3.2}$$

This two neutrino hypothesis has been extended to include the third neutrino species and any other addition to the neutrino family.

3.3.1 Neutrino Masses

The Dirac neutrino mass Lagrangian is written

$$\mathcal{L}_D = -\overline{\nu_R} M_D \nu_L + h.c. \tag{3.3}$$

Where M_D is a non-diagonal complex $n \times n$ matrix and

$$\nu_L = \begin{pmatrix} \nu_{eL} \\ \nu_{\mu L} \\ \nu_{\tau L} \end{pmatrix}, \nu_R = \begin{pmatrix} \nu_{eR} \\ \nu_{\mu R} \\ \nu_{\tau R} \end{pmatrix}. \tag{3.4}$$

The Dirac neutrino mass Lagrangian couples the ν_R flavour fields with ν_L flavour fields, where the L and R indices indicate left-handed and right-handed chirality states. These weak flavour eigenstates are connected to the mass eigenstates via equation 3.13 (which is explained in the next section).

The Majorana neutrino mass Lagrangian is written

$$\mathcal{L}_M = -\frac{1}{2} \left(\overline{\nu_L}\right)^c M_M \nu_L + h.c., \tag{3.5}$$

where M_M is an $n \times n$ symmetric matrix, and $\left(\overline{\nu_L}\right)^c$ is the charge conjugated $\overline{\nu_L}$, which satisfies the Majorana condition, $(\nu_L)^c = C\overline{\nu_L}^T$, where C is the charge conjugation matrix which obeys

$$C^T \gamma_\alpha C^{-1} = -\gamma_\alpha C^T \tag{3.6}$$

The Dirac-Majorana neutrino mass term is constructed from left- and right-handed fields

$$\begin{aligned}\mathcal{L}_{D-M} &= -\frac{1}{2}[(\overline{\nu_L})^c M_L^M \nu_L + \overline{\nu_R} M_R^M (\nu_R)^c \\ &+ \overline{\nu_R} M_D \nu_L + (\overline{\nu_L})^c M_D^T (\nu_R)^c] + h.c. \end{aligned} \tag{3.7}$$

where M_L^M and M_R^M are complex non-diagonal symmetrical 3×3 matrices. The Dirac-Majorana neutrino mass term, $\mathcal{L}_{D-M}$ can be used to explain the smallness of the neutrino (compared to other leptons) via the see-saw mechanism [31], [32]. If we assume one neutrino generation, $\mathcal{L}_{D-M}$ can be written

$$\mathcal{L}_{D-M} = -\frac{1}{2}((\overline{\nu_L})^c \overline{\nu_R}) \mathcal{M} \begin{pmatrix} \nu_L \\ \nu_R^c \end{pmatrix} + h.c., \tag{3.8}$$

where

$$\mathcal{M} = \begin{pmatrix} m_L^M & m_D \\ m_D & m_R^M \end{pmatrix}. \tag{3.9}$$

After diagonalisation of $\mathcal{M}$ we obtain the eigenvalues,

$$m_{1,2} = \frac{1}{2}(m_L^M + m_R^M) \pm \frac{1}{2}\sqrt{(m_L^M - m_R^M)^2 + 4(m_D)^2}, \tag{3.10}$$

and now four different scenarios can be considered:

- $m_L^M = m_R^M = 0 \Rightarrow m_{1,2} = \pm m^D$ - pure Dirac neutrino.
- $m^D \gg m_L^M, m_R^M \Rightarrow m_{1,2} \approx \pm m^D$ - pseudo Dirac neutrino.
- $m^D \to 0 \Rightarrow m_{1,2} = m_L^M, m_R^M$ - pure Majorana neutrino.
- $m_R^M \gg m^D$, and $m_L^M = 0$ - see-saw mechanism.

The see-saw mechanism results in two eigenvalues,

$$m_1 = \frac{(m^D)^2}{m_R^M} \tag{3.11}$$

$$m_2 = m_R^M \left(1 + \left(\frac{m^D}{m_R^M}\right)^2\right) \approx m_R^M \tag{3.12}$$

The right-handed mass is of the order of the GUT scale ($m_2 = m_R^M = m_{GUT} \approx 10^{12}\,\text{GeV}$) and m_1 is therefore the smaller mass, where the mass of m^D is of the order of charged leptons and quarks. If we expand this general case to take in the 3 flavour generations we get three very light masses and three heavy masses. The existence of the Majorana neutrino clearly has implications for leptogenesis and baryogenesis, and could explain the observed matter-antimatter asymmetry in the Universe [30].

3.3.2 Neutrino Mixing

Neutrino mixing is analogous to the Cabibbo-Kobyashi-Maskawa (CKM) mixing in the quark sector, where the three flavour eigenstates (ν_e, ν_μ and ν_τ) can be represented as a mixture of the three mass eigenstates (ν_1, ν_2 and ν_3) via the unitary Pontecorvo-Maki-Nakagawa-Sakata (PMNS) matrix, which is comparable to the CKM mixing matrix for quarks,

$$|\nu_\alpha\rangle = \sum_i U^*_{\alpha i} |\nu_i\rangle \tag{3.13}$$

where ν_α are the neutrino flavour eigenstates, ν_i are the neutrino mass eigenstates, and U is the PMNS matrix

$$U = \begin{pmatrix} c_{12}c_{13} & s_{12}c_{13} & s_{13}e^{-i\delta} \\ -s_{12}c_{23} - c_{12}s_{23}s_{13}e^{i\delta} & c_{12}c_{23} - s_{12}s_{23}s_{13}e^{i\delta} & s_{23}c_{13} \\ s_{12}s_{23} - c_{12}c_{23}s_{13}e^{i\delta} & c_{12}s_{23} - s_{12}c_{23}s_{13}e^{i\delta} & c_{23}c_{13} \end{pmatrix} \begin{pmatrix} e^{-i\phi_1/2} & 0 & 0 \\ 0 & e^{-i\phi_2/2} & 0 \\ 0 & 0 & 1 \end{pmatrix} \tag{3.14}$$

where c_{ij} and s_{ij} are the sine and cosine of the three mixing angles θ_{ij}. δ is the Dirac (CP violating) phase, and ϕ_1 and ϕ_2 are the Majorana phases, which only affect Majorana particles. Neutrino oscillations, discussed in the next section, are a natural progression from the idea that neutrinos mix.

3.3.3 Neutrino Oscillations

Neutrino oscillation is a process whereby a neutrino of one flavour evolves in time, changing into a neutrino with a different flavour. In a vacuum the probability of a

neutrino with flavour α changing into a neutrino with flavour β is

$$P(\nu_\alpha \to \nu_\beta) = \left| \sum_i U^*_{\alpha i} U_{\beta i} e^{\frac{-i m_i^2 L}{2E}} \right|^2 \tag{3.15}$$

where m_i are the neutrino mass eigenstates, $U_{\alpha,\beta}$ unitary PMNS matrices, L is the propagation length and E is the energy of the neutrino. In the simplified two flavour neutrino case the oscillation probabilities become

$$P(\nu_\alpha \to \nu_\beta) = \sin^2 2\theta \sin^2 \left[1.27 \frac{\Delta m^2 L}{E} \right] \tag{3.16}$$

$$P(\nu_\alpha \to \nu_\alpha) = 1 - \sin^2 2\theta \sin^2 \left[1.27 \frac{\Delta m^2 L}{E} \right] \tag{3.17}$$

where $\Delta m^2 = m_i^2 - m_j^2$ in eV^2, L is in km and E in GeV.

Now that we have the oscillation probabilities for the appearance and disappearance of neutrinos we can look more closely at the PMNS matrix in equation 3.14. The oscillation probabilities are independent of the two Majorana phases. The angles θ_{ij} correspond to neutrinos of different origins. θ_{23} governs atmospheric (atm) neutrinos; θ_{12} governs solar (sol) neutrinos and θ_{13} governs short baseline reactor (rtr) neutrinos, and can also be measured by accelerator neutrino experiments. For the differences in the masses squared we have,

$$\Delta m^2_{atm} = m_3^2 - m_2^2 \approx \Delta m^2_{rtr} = m_3^3 - m_1^2, \qquad \Delta m^2_{sol} = m_2^2 - m_1^2. \tag{3.18}$$

The next few sections will review neutrino oscillation experiments and their contribution to neutrino parameters, and other relevant neutrino mass measurements.

3.4 Neutrino Mass and Mixing Measurements

There are various different ways to measure neutrino masses, some more successful than others. There are direct kinematic techniques such as tritium beta decay, which is model independent, and particle decay measurements, which, for example, use pion decay to measure the muon neutrino mass. And the less straightforward indirect techniques such as $0\nu\beta\beta$ decay, which requires the non-conservation of lepton

number, and neutrino oscillations, which give us an insight into the difference of the squared masses and allow us to measure mixing parameters.

Secs. 3.4.1 - 3.4.7 discuss some of the most successful and interesting neutrino mass measurement techniques and experiments, and Sec. 3.4.8 reviews results from these experiments and explains some more aspects of mass measurements such as mass hierarchies.

3.4.1 Solar Neutrinos

Nuclear fusion reactions in the core of the sun provide us with the closest and most abundant source of neutrinos. These neutrinos are produced through two main cycles: the proton-proton (pp) chain and the Carbon-Nitrogen-Oxygen cycle.

Solar neutrinos were first detected by Ray Davis in the Homestake mine, with 100,000 gallons of tetrachloroethylene, in 1968 [14]. The ^{8}B, ^{7}Be and *pp* neutrinos were detected via the reaction

$$^{37}Cl + \nu_e \rightarrow ^{37}\ Ar + e^- \tag{3.19}$$

with a threshold of 814 keV. Davis extracted and counted the argon atoms by pumping helium through the massive tank. He consistently found a third of the ν_e that were expected from the calculations of John Bahcall, leading to the belief that either one, or both physicists had made a mistake somewhere, i.e. that there was something inherently wrong with the Standard Solar Model (SSM), or that there was an experimental error, or that there was new physics neither of them had taken into account.

The two gallium experiments SAGE [33] and GALLEX [34] and the water Cerenkov experiment Kamiokande II [17] confirmed the Homestake results. Super-K [35] and SNO [36] went one step further by providing the evidence of neutrino oscillations needed to explain the deficit of ν_e.

SAGE and GALLEX both detected *pp* neutrinos with the ^{71}Ga reaction

$$^{71}Ga + \nu_e \rightarrow ^{71}\ Ge + e^- \tag{3.20}$$

which has a low threshold of 233 keV.

Kamiokande II and Super-K detected the Cerenkov light produced in neutrino-electron interactions in the water. Neutrinos from the ^{8}B chain, with a threshold of $\sim$5 MeV were detected.

The SNO experiment used a heavy water target, and was able to distinguish signatures between ν_e and $\nu_x = \nu_e, \nu_\mu, \nu_\tau$ by measuring the processes:

$$\text{Charge-current (CC): } \nu_e + d \rightarrow e^- + p + p \tag{3.21}$$

$$\text{Neutral-current (NC): } \nu_x + d \rightarrow \nu_x + n + p \tag{3.22}$$

$$\text{Elastic scattering (ES): } \nu_x + e^- \rightarrow \nu_x + e^- \tag{3.23}$$

All three neutrino flavours are equally likely to be detected via the NC process. The neutrino interacts with the deuterium nucleus and breaks it apart. The neutron from this interaction is captured by another deuterium nucleus, and a γ-ray of $\sim$6 MeV is produced. The γ-ray scatters electrons which produce Cerenkov radiation; the Cerenkov light is then detected by the detector's PMTs. The ratio CC/NC is used to show the oscillation of ν_e to either ν_μ or ν_τ flavours

$$\frac{CC}{NC} = \frac{flux(\nu_e)}{flux(\nu_e + \nu_\mu + \nu_\tau)}. \tag{3.24}$$

Since ν_e are the only neutrinos produced in the sun, the fluxes from ν_μ and ν_τ are due to flavour oscillations. If there are no oscillations, the ratio CC/NC should be one.

The first results from SNO were published in 2001, putting an end to the speculation about the SSM, and providing evidence of neutrino masses. The most recent results from SNO for Δm^2_{sol} and θ_{sol} [37] are

$$\Delta m^2_{sol} = \Delta m^2_{21} = 8.0^{+0.6}_{-0.4} \times 10^{-5}\,\text{eV}^2,\ \theta_{sol} = \theta_{12} = 33.9^{+2.4}_{-2.2}\,^\circ. \tag{3.25}$$

3.4.2 Reactor Neutrinos

Nuclear reactors produce an immense source of $\bar{\nu_e}$ during the fission of heavy nuclei such as ^{235}U, which produces six $\bar{\nu_e}$ per fission, essentially allowing precision measurements of several oscillation parameters.

Reactor experiments typically use a liquid scintillator target, and neutrinos are detected via the inverse β decay process, where the $\bar{\nu_e}$ coming from the reactor interact with protons in the target to produce neutrons and positrons as in Eq 3.26.

$$\bar{\nu_e} + p \rightarrow n + e^+. \tag{3.26}$$

The positrons annihilate with electrons in the target creating two photons and the neutrons are captured by the target nuclei, which emit photons $\sim$15 μs after the positron photons. In this way experiments use a delayed coincidence technique to detect the neutron and positron signatures. The main background for this type of experiment are cosmic ray muons, which produce neutrons in the areas surrounding the detectors.

These experiments are searching for the disappearance of the emitted $\bar{\nu_e}$ at a distance L from the reactor via Eq. 3.17, so the number of $\bar{\nu_e}$ leaving the detector has to be known precisely. This is done by calculating the $\bar{\nu_e}$ spectra from the β decay of the fission products of the isotopes ^{235}U, ^{239}Pu and ^{241}Pu, with the less significant contribution from ^{238}U being calculated by summing all its possible β decay processes.

The first reactor experiment was carried out in 1953 by Reines and Cowan [7] at the Hanford reactor. The experiment was unsuccessful due to the large cosmic ray background, so in 1956 they tried again at the Savannah River reactor [8]. This shielded experiment allowed them to make the first ever detection of neutrinos. It was not until several decades and many different experiments later that KamLAND (Kamioka Liquid scintillator Anti-Neutrino Detector) managed to produce evidence of reactor neutrino oscillations [28].

Before KamLAND, the CHOOZ experiment [38] based at the CHOOZ reactor in the Ardennes, France, although not able to confirm reactor neutrino disappearance, did exclude a large area of oscillation parameter space, giving strong evidence that $\nu_\mu \rightarrow \nu_e$ oscillations were not the cause of the atmospheric neutrino deficit. Their results for θ_{13} ($\sin^2\theta_{13} < 0.2$ at $\Delta m^2_{31} = 2 \times 10^{-3}\,\mathrm{eV}^2$) are currently the best in the world [39]. The next generation experiment, Double CHOOZ [40] aims to improve on this result.

KamLAND is located at the site of the old KamiokaNDE experiment. The detector contains 1000 tonnes of liquid scintillator in a spherical balloon, made of a transparent material, which is suspended in oil. The sphere and oil are contained in a stainless steel tank, with photomultiplier tubes (PMTs) mounted on the inner surface. The gap between the detector and the cavity walls is filled with ultra-pure water surrounded by more PMTs, which acts as a Cerenkov detector for cosmic rays. The water also suppresses the radioactivity coming from the cavity walls.

The latest results from KamLAND are [41]

$$\Delta m^2_{21} = 7.58^{+0.14}_{-0.13}(stat.)^{+0.15}_{-0.15}(syst.) \times 10^{-5}\,\mathrm{eV}^2, \tag{3.27}$$

$$\tan^2\theta_{12} = 0.56^{+0.10}_{-0.07}(stat.)^{+0.10}_{-0.06}(syst.) \equiv \theta_{12} = 36.8^\circ. \tag{3.28}$$

3.4.3 Atmospheric Neutrinos

Atmospheric neutrinos are decay products from decays of muons, pions and other mesons that come from interactions between cosmic rays (typically protons) and nuclei in Earth's upper atmosphere. The dominant process that produces these neutrinos is

$$\pi^+ \rightarrow \mu^+ + \nu_\mu \tag{3.29}$$

$$\mu^+ \rightarrow e^+ + \bar{\nu_\mu} + \nu_e \tag{3.30}$$

and their charge conjugates. This gives the expected ratio of $\nu_\mu(\bar{\nu_\mu})$ to $\nu_e(\bar{\nu_e})$ (ν_μ/ν_e) of 2:1. This ratio is well understood and has been calculated with great precision [42], [43], [44].

The ν_μ/ν_e flux ratio is obtained by observing the flavour of the final state leptons (μ or e) which are produced via charge-current reactions, to determine the flavour of the neutrino which initiated the charge-current reaction. Experiments use the double ratio $\mathcal{R}$ of experimental values verses MC predictions of μ/e to verify their results,

$$\mathcal{R} = \frac{(N_\mu/N_e)_{data}}{(N_\mu/N_e)_{MC}}. \tag{3.31}$$

This ratio has the effect of cancelling out experimental and theoretical uncertainties. If the physics in the MC simulations is accurate and models the data well, then the ratio $\mathcal{R} = 1$ is expected.

For these experiments (which are located near the surface of the Earth) the probability of a neutrino of one flavour oscillating to a neutrino of another flavour is given by Eq. 3.16. This equation is a function of the zenith angle of the incident neutrino's direction and is related to the distance L it travels to get to the detector. For neutrinos travelling vertically downwards $L \sim 15\,\text{km}$, neutrinos travelling vertically upwards travel a distance $L \sim 13,000\,\text{km}$ before reaching the detector.

A ν_μ deficit was first measured in 1983 by the IMB experiment [45] which was verified by KamiokaNDE [16] (both water Cerenkov detectors). During the mid 1980's a couple of results followed from experiments that did not see a deficit. Although NUSEX (Nucleon Stability Experiment), located in the Mont Blanc tunnel [46] and Fréjus, a steel-calorimeter experiment based in the same location as NEMO 3 [47] produced results which did not seem to back up the findings of IMB and KamiokaNDE, the experiments that followed, Soudan-2, an iron-calorimeter experiment [48] and MACRO, a liquid scintillator experiment [49], did verify them with higher statistics. These combined results pointed to a value of $\mathcal{R} \sim 0.6$. The experiment that followed these (Super-K) ended all speculation.

The Super-K water Cerenkov experiment was set up to search for proton decay, and solar and atmospheric neutrinos, and provided the first concrete evidence of neutrino oscillations through the study of atmospheric neutrinos. Super-K was able to measure the zenith angle of an incident neutrino, and hence the distance it had travelled to the detector enabling the oscillation probability hypothesis to be fully tested. The results from Super-K are consistent with $\nu_\mu \rightarrow \nu_\tau$ oscillations. The allowed regions for Δm^2_{32} and $\theta_{23}$are, at 90% C.L. [50]:

$$1.9 \times 10^{-3} < \Delta m^2_{32} < 3.0 \times 10^{-3}\,\text{eV}^2 \tag{3.32}$$

$$\sin^2 2\theta_{atm} = \sin^2 2\theta_{23} > 0.9. \tag{3.33}$$

3.4.4 Accelerator Neutrinos

Another source of terrestrial neutrinos are neutrinos from high energy accelerators. Neutrino beams are typically produced by firing a high energy proton source at a target. This generates secondary pions and kaons, which decay and give predominantly ν_μ. The ν_μ are detected by means of a charged current weak interaction

$$\nu_\alpha + N \rightarrow \alpha + X \tag{3.34}$$

where N is a nucleon and X is a hadronic state.

Neutrino accelerator experiments are able to control the energy, flavour and flux of the neutrinos, which puts them at a distinct advantage over other neutrino oscillation experiments. Short baseline experiments have detectors of $\sim$1 km from the neutrino source, whereas long baseline experiments have distances from source to detector of hundreds of kilometres.

The first accelerator experiment was carried out in 1962 by Danby et al. [11], which confirmed the existence of two neutrino flavours, ν_e and ν_μ. The short baseline experiments that followed, such as NOMAD (Neutrino Oscillation MAgnetic Detector) [51], CHORUS (Cern Hybrid Oscillation Research apparatUS) [52] and KARMEN (KArlsrue-Rutherford Medium Energy Neutrino) [53], although not successful in observing neutrino oscillation, put very stringent limits on oscillation parameters. The LSND (Liquid Scintillator Neutrino Detector) experiment claimed to see neutrino oscillations [54], which would have confirmed the existence of sterile neutrinos. This claim needed to be verified, and MiniBooNE (Mini Booster Neutrino Experiment) [55] was set up for this purpose. The results from MiniBooNE did indeed refute the simple two neutrino oscillation LSND claim [56], although low energy events are still being studied.

The first operating long baseline experiment was K2K (KEK to Kamioka) [57]. The K2K detector was the Super-K detector based in the Kamioka mine, about 250 km from the KEK accelerator. It was designed to observe the disappearance of ν_μ. The average energy of the ν_μ leaving KEK was $\sim$1.3 GeV. K2K claimed an observation of neutrino oscillation, and obtained the results [58]

$$\Delta m^2_{32} = 2.8^{+0.1}_{-0.7} \times 10^{-3}\,\mathrm{eV}^2,\ \sin^2\theta_{23} = 1. \tag{3.35}$$

One of the most successful long baseline experiments is MINOS [59]. NuMI (Neutrinos at the Main Injector) the main injector at Fermilab generates a beam of mostly ν_μ, which is sent through the near detector also based a Fermilab, where the beam is sampled. The beam then travels 735 km through the Earth to the far detector in Minnesota, at the Soudan Mine, where it is tested again. The latest results from MINOS are [60]

$$\Delta m^2_{32} = 2.43 \pm 0.13 \times 10^{-3}\,\mathrm{eV}^2\ (68\%\ \mathrm{C.L.}),\ \sin^2\theta_{23} > 0.9\,(90\%\ \mathrm{C.L.}). \tag{3.36}$$

The CNGS (CERN Neutrinos to Gran Sasso) experiment is a ν_τ appearance experiment, set up specifically to observe $\nu_\mu \to \nu_\tau$ oscillations. The CNGS ν_μ beam produced at the CERN SPS accelerator will travel 730 km from CERN to Gran Sasso, where there are two detectors, OPERA (Oscillation Project with Emulsion tRacking Apparatus) [61] which is the main detector, and ICARUS (Imaging Cosmic And Rare Underground Signals) [62].

T2K [63], a next generation appearance experiment based in Japan, will be the world's first oscillation experiment to use an off-axis neutrino beam. Although T2K will be measuring the parameters Δm^2_{32} and θ_{23}, its main focus is on a measurement of θ_{13} and improving on the sensitivity reached by the CHOOZ experiment. The ν_μ beam will travel 295 km from JPARC in Tokai to the far detector, which is the Super-K water Cerenkov detector. The first phase of T2K will begin in 2009 with the near detector, which is placed 280 m from the beam at JPARC. Another next generation off-axis appearance experiment which aims to improve on the θ_{13} measurement is the NOνA (NuMI Off-axis ν_e Appearance) experiment [64]. The far detector will be based in Northern Minnesota, and will be designed to detect ν_e from Fermilab's NuMi beam.

If θ_{13} is measured by these next generation experiments, it would be possible for future generation experiments such as neutrino factories to address CP violation in the neutrino sector and also the hierarchy of neutrino masses.

3.4.5 Cosmological Mass Measurements

A limit on the sum of the neutrino masses ($\sum_i m_i = \Sigma$) can be obtained by using data from astrophysical experiments. These limits are based on a specific cosmological model, which assumes the universe is flat, homogeneous, isotropic, and made up of ordinary matter, radiation, dark matter and dark energy.

In the early universe, not only was there a large scale production of photons, but also of neutrinos. Massive neutrinos may therefore make up considerable contribution to the energy density of the universe. This contribution depends on Σ,

$$\sum_i m_i = 94(eV)\Omega_\nu h^2, \tag{3.37}$$

where Ω_ν is the energy density of the Universe in neutrinos and h is the normalised Hubble constant.

The measurement of Σ depends on the neutrino mass hierarchy (see section 3.4.8). If there is a degenerate hierarchy (i.e. $m_{\nu_1} \approx m_{\nu_2} \approx m_{\nu_3}$) there would be an observable neutrino signature in the Cosmic Microwave Background angular power spectrum, and neutrinos would also have played a signifiant role in the large scale structure (LSS) formation of galaxies. Calculations of Σ are model dependent, as there are different models used to explain the formation of the LSS giving different values of the neutrino mass. To date a number of different data sources have been used to obtain limits on Σ. These typically include WMAP data, Large Scale Structure constraints, Lyman-α forest data, and the 2dF Galaxy Redshift Survey data. Results for an upper limit on Σ (using different combinations of data) range from 0.7 - 2 eV at 2σ (see [65] and references therein).

3.4.6 Tritium Beta Decay

Tritium decays into ^{3}He via the reaction in Eq. 3.38, with a half-life of 12.3 yrs

$$^3H \rightarrow ^3 He^+ + e^- + \bar{\nu_e} \tag{3.38}$$

As the decay is super-allowed the spectral shape is independent of the matrix elements, and calculations of initial and final states of the decay are far less complicated

than for those of the heavier elements and have smaller errors. The effective neutrino mass from tritium β decay experiments is then defined as

$$\langle m_\beta \rangle = \left| \sum_i U_{ei}^2 m_i^2 \right|^{1/2} \tag{3.39}$$

The technique of the tritium β decay experiments is to measure the distortion of the endpoint E_0 of the tritium β decay spectrum caused by the finite neutrino mass. The spectrum being measured is defined as

$$\frac{dN}{dE} = N(E) = CFp_eE(E_0 - E)^2 \sqrt{1 - \frac{m_{\bar{\nu}_e}^2 c^4}{(E_0 - E)^2}} \tag{3.40}$$

where constant C is

$$C = G_F^2 \frac{m_e^5 c^4}{2\pi^3 \hbar^2} \cos^2 \theta_c |M|^2 \tag{3.41}$$

where G_F is the Fermi coupling constant, θ_c is the Cabibbo angle, and $|M|$ is the relevant matrix element. F is the Fermi function, p_e is the momentum of the electron, E is the energy of the electron and E_0 is the endpoint energy of the electron or Q_β value. $E_0 - E$ is therefore the energy of the neutrino. To see this possible distortion in the spectrum, $N(E)$ is transformed to the Kurie plot spectrum

$$K(E) = \sqrt{\frac{N(E)}{Fp_eE}} \propto (E_0 - E) \left[1 - \left(\frac{m_{\bar{\nu}_e} c^2}{E_0 - E} \right)^2 \right]^{1/4} \tag{3.42}$$

This is illustrated in Fig. 3.1 If the neutrino mass is zero, the slope is a straight line, but if the neutrino has a finite mass, the spectrum will be modified to go to zero with a vertical slope.

One of the main difficulties associated with tritium β decay experiments is the low counting rate at the end point of the decay spectrum. The measurement of the mass from the decay spectrum is also limited by the energy resolution of the spectrometer, luminosity and background considerations. The final electronic states should also be known with some degree of accuracy.

The first measurement of the shape of the tritium β decay spectrum was carried out by Curran, Angus and Cockcroft in 1948 [66]. They obtained a very conservative upper limit of $\sim 1\,\mathrm{keV}$ [67]. The best (and most precise) results to date come from

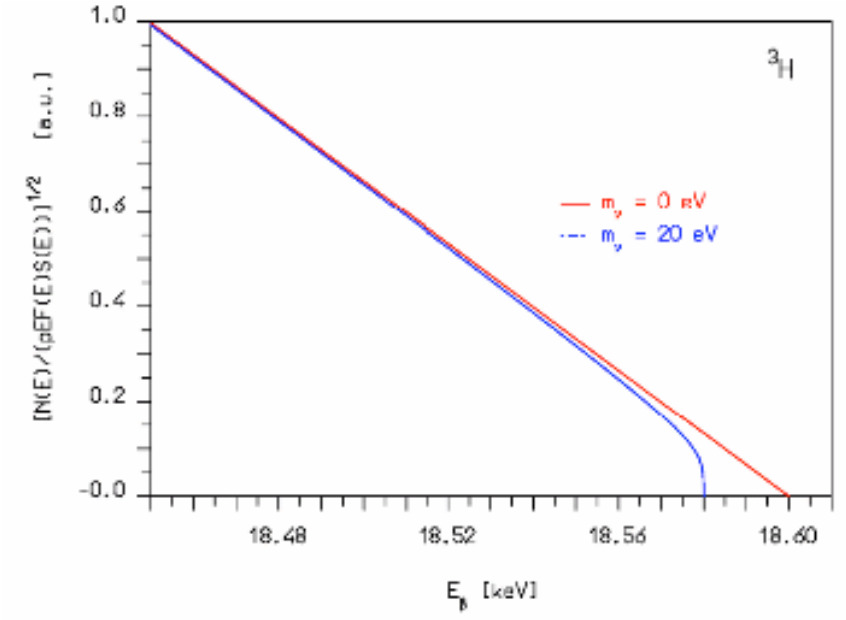

Figure 3.1: A Kurie plot showing the end point of tritium β decay. If the neutrino has a finite mass a distorted plot will be observed as shown for $m_{\bar{\nu_e}} = 20\,\text{eV}$ [71].

the Mainz [68] and Troitsk [69] experiments with a combined limit of $m_{\bar{\nu_e}} < 2.2\,\text{eV}$ at 2σ. The Karlsruhe TRItium Neutrino experiment (KATRIN) is a next generation experiment designed to reach a sensitivity to the neutrino mass of $\sim$0.3 eV. KATRIN is currently being built in Forschungszentrum Karlsruhe in Germany, and is expected to start taking data in 2009 [70].

3.4.7 Neutrinoless Double Beta Decay

$0\nu\beta\beta$ decay is only relevant to neutrino mass searches if the neutrino is a Majorana particle, and if lepton number conservation is violated. Experiments searching for this rare decay obtain upper limits on the effective neutrino mass ($\langle m_{\beta\beta}\rangle$) which is defined as

$$\langle m_{\beta\beta}\rangle = \left|\sum_i U_{ei}^2 m_i\right| = \left|c_{12}^2 c_{13}^2 m_1 + s_{12}^2 c_{13}^2 m_2 e^{i\phi 2} + s_{13}^2 m_3 e^{i\phi 3}\right|. \tag{3.43}$$

$0\nu\beta\beta$ decay will be discussed in more detail in the next chapter.

3.4.8 Summary

The results from the above experiments are summarised in Table 3.4.8. The data from these experiments are consistent with an extension to the standard electroweak model where the three (known) neutrino flavour states mix with the three neutrino mass states.

Parameter	**Value**	**C. L.**	**Reference**
$\sin^2 2\theta_{12}$	$0.86^{+0.03}_{-0.04}$	68%	[37]
$\sin^2 2\theta_{23}$	> 0.92	90%	[50]
$\sin^2 2\theta_{13}$	< 0.19	90%	[38]
Δm^2_{21}	$8.0^{+0.4}_{-0.3} \times 10^{-5}\,\mathrm{eV}^2$	68%	[37]
Δm^2_{32}	$2.4^{+0.6}_{-0.5} \times 10^{-3}\,\mathrm{eV}^2$	90%	[50]
$\langle m_\beta \rangle$	$< 2\,\mathrm{eV}$	95%	[68], [72]
$\langle m_{\beta\beta} \rangle$	$< 0.7\,\mathrm{eV}$	90%	[73], [74]
Σ	$< 2\,\mathrm{eV}$	95%	[75]

Table 3.1: Current best results for neutrino measurements [76]. The neutrino mixing parameters references are taken from the Particle Data Book [77], all other results are from individual references.

With $\Delta m^2_{21} << \Delta m^2_{32}$ there are three different scenarios for neutrino mass ordering. The normal hierarchy (NH) is where $m_1 < m_2 < m_3$, the inverted hierarchy (IH) is where $m_3 < m_1 < m_2$, which are illustrated in Fig. 3.2. Neutrino masses may also be quasi degenerate, where $m_1 \approx m_2 \approx m_3$. The NH and IH are linked to the sign of Δm^2_{32} ($sgn(\Delta m^2_{32})$) where the NH corresponds to $sgn(\Delta m^2_{32}) > 0$ and the IH corresponds to $sgn(\Delta m^2_{32}) < 0$. To date experiments have not been able to determine $sgn(\Delta m^2_{32})$, and therefore cannot discriminate between the NH and IH.

The $sgn(\Delta m^2_{32})$, θ_{13}, the CP-violating phases, the absolute neutrino mass and the nature of neutrino mass are all unsolved problems, which could be tackled by next generation experiments. θ_{13} can only be measured by oscillation experiments. If θ_{13} is measurable (i.e. it is greater than zero) then it may be possible to search for the Dirac CP-violating phases and determine $sgn(m^2_{32})$, and therefore the mass

hierarchy. This may be tackled by future super beam projects and neutrino factories. It may also be possible to determine the mass hierarchy with next generation $0\nu\beta\beta$ decay experiments (if the neutrino is a Majorana particle) and tritium β decay experiments. One can see from Fig. 3.3 how different mass hierarchies lead to different effective Majorana neutrino masses. The absolute neutrino mass could also be measured by $0\nu\beta\beta$ decay experiments as well as the tritium β decay experiments. And finally the nature of the neutrino mass can only be found by $0\nu\beta\beta$ decay experiments. These four main unanswered questions on the neutrino are summarised in Table 3.4.8 with the mixture of experiments which can determine the answers.

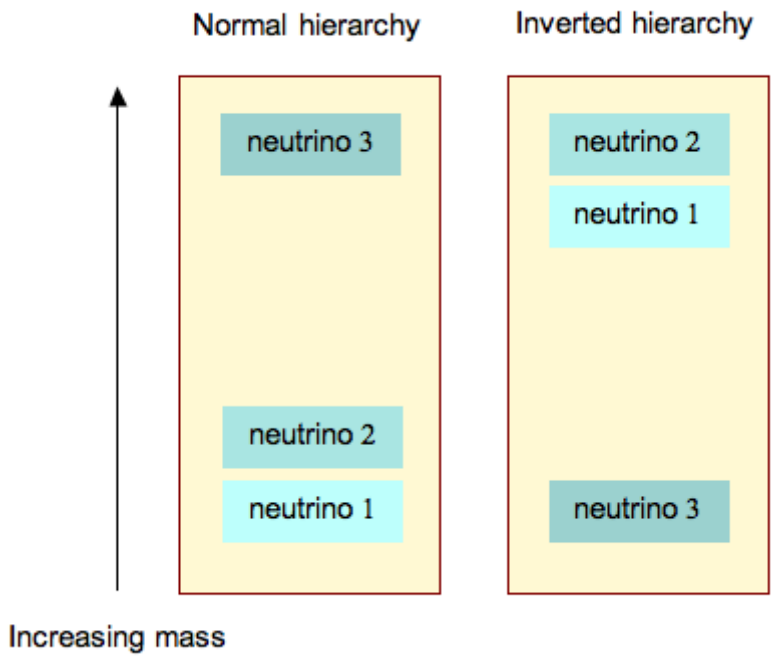

Figure 3.2: The neutrino mass hierarchy model, showing the normal and inverted schemes.

If the next generation neutrino oscillation experiments, and the β and $0\nu\beta\beta$ decay experiments are successful, the results can also be combined to gain a more profound insight into neutrino physics and physics beyond the standard model. If a positive result for $\langle m_\beta \rangle$ is obtained, and all the mixing angles are known, as well as the differences in the masses squared, then values of m_1, m_2 and m_3 can be extracted.

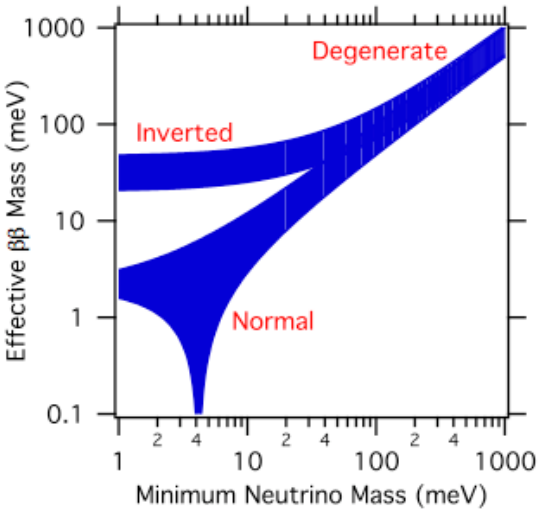

Figure 3.3: The effective Majorana mass vs the mass of the lightest neturinos.

By measuring the effective mass from $0\nu\beta\beta$ decay experiments, the Majorana phases can be calculated. Thus each next generation experiment has an important role to play in determining the nature of the neutrino and the neutrino masses themselves.

Experiment	β **Decay**	$0\nu\beta\beta$ **Decay**	**Super Beams**	ν **Factories**
Abs. neutrino mass	X	X		
Neutrino nature		X		
Majorana CP		X		
Dirac CP			X	X
Mass hierarchy		X	X	X

Table 3.2: The four main unanswered neutrino questions and the next generation experiments which may be able to answer those questions. Note that $0\nu\beta\beta$ decay experiments will only be successful if the neutrino is found to be a Majorana particle, and that the Super beam and neutrino factory experiments will only be successful if θ_{13} is measurable.

Chapter 4

Double Beta Decay Theory and Experiment

The double beta decay theory chapter begins by describing several different beta decay processes. Sec. 4.2 discusses nuclear structure theory and nuclear matrix elements, Sec. 4.3 discusses experimental criteria and reviews a range of experiments studying double beta decay past, present and future.

$\beta\beta$ decay is a rare nuclear process which occurs spontaneously between two nuclei with the same mass number A, in which the proton number Z is changed by two units, leaving A unchanged. This process occurs when the first-order beta decay is either energetically forbidden or suppressed by selection rules.

In first-order β decay, there are three different modes of decay: β^- decay where a neutron changes into a proton while emitting an electron and an antineutrino,

$$n \rightarrow p + e^- + \bar{\nu}_e, \tag{4.1}$$

β^+ decay where a proton changes into a neutron, while emitting a positron and a neutrino,

$$p \rightarrow n + e^+ + \nu_e, \tag{4.2}$$

and the final mode is electron capture (EC). Electron capture occurs when the nucleus does not have enough energy to emit a positron. An electron (usually from

the K shell) is absorbed into the nucleus, a proton changes into a neutron and emits a neutrino. This leaves the atom in an excited state, and the process is accompanied by the emission of X-rays and/or Auger electrons,

$$p + e^- \rightarrow n + \nu_e \tag{4.3}$$

These processes cannot occur unless the mass of the parent nuclei is greater than that of the daughter nuclei, this is illustrated in Fig. 4.1.

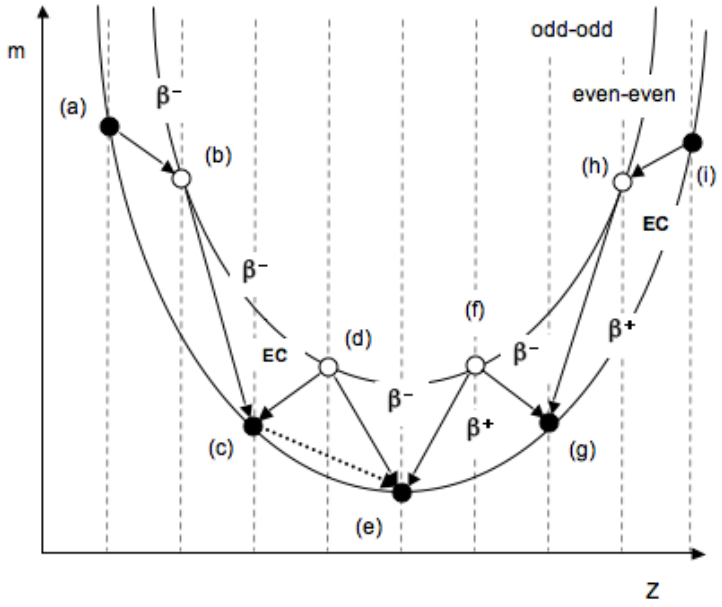

Figure 4.1: The parabola shows energetically possible single and double beta decays. (e) is stable having the lowest mass. (c) cannot decay to (d) as the mass of (d) is greater than that of (c). Double beta decay is possible between (c) and (e).

For even A nuclei, both even-even and odd-odd nuclei can occur. They can decay either by $\beta^{\pm}$ or EC decay towards the one stable isotope (e) at the bottom of the parabola. In this hypothetical case (c) cannot decay to (d) as the mass of (d) is greater than that of (c). However, although this is the case, (c) could decay to (e) (as (e) has a lower mass) via $\beta\beta$ decay. $\beta\beta$ decay only occurs in even A nuclei, and can go from the ground state (0^+) of the parent nucleus to the ground state (0^+) nucleus of the daughter nucleus, and in some cases where energetically allowed, the

excited states (0^+, 2^+) of the daughter nucleus.

$\beta\beta$ decay is a second-order weak semileptonic process. Two-neutrino beta decay conserves electric charge, lepton number, and is an allowed process in the standard electroweak model (see Fig. 4.2). During this process two electrons and two antineutrinos are emitted.

$$(A, Z) \rightarrow (A, Z + 2) + e_1^- + e_2^- + \bar{\nu}_{e1} + \bar{\nu}_{e2} \tag{4.4}$$

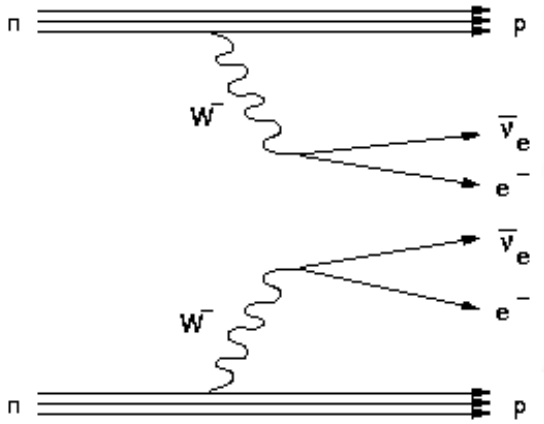

Figure 4.2: Feynman diagram for the $2\nu\beta\beta$ decay process.

Neutrinoless double beta decay violates lepton number conservation and is forbidden in the standard electroweak model. During this process only two electrons are emitted.

$$(A, Z) \rightarrow (A, Z + 2) + e_1^- + e_2^- \tag{4.5}$$

The $0\nu\beta\beta$ decay process is illustrated in Fig.4.3 showing this process can only occur if $\nu_e = \bar{\nu_e}$, i.e if the neutrino is a Majorana particle. A virtual right-handed neutrino is emitted from one vertex and a virtual left-handed neutrino is absorbed by the second vertex, essentially the virtual right-handed neutrino flips helicity to a virtual left-handed antineutrino. This helicity flip (although unlikely) can only occur if the

neutrino is massive; it would be impossible if the neutrino were massless, as there would be no reference frame where the direction of momentum is reversed.

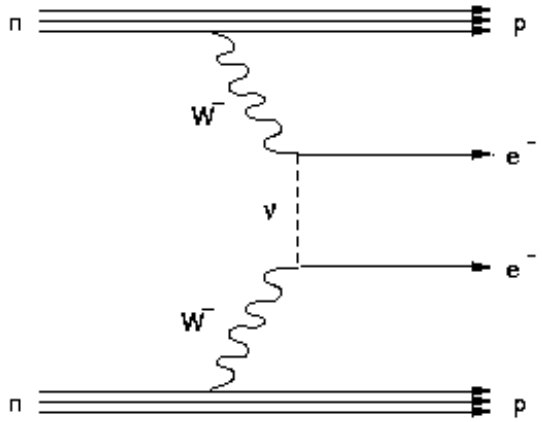

Figure 4.3: Feynman diagram for the $0\nu\beta\beta$ decay process.

A third mode is also possible: double beta decay with Majoron emission [78].

$$(A, Z) \rightarrow (A, Z + 2) + e_1^- + e_2^- + \chi \tag{4.6}$$

This is also a lepton number violating process involving the Majoron, a hypothetical scalar particle. Although double beta decay with Majoron emission is an interesting and important process, it will not be discussed further in this thesis along with the other possible mechanisms mentioned in Sec. 4.1.2.

We can see that from Fig. 4.4 that if the energy of the two emitted electrons is measured it is easy to distinguish between each of the modes described above by the shape of the electron energy sum spectrum. In the $0\nu\beta\beta$ decay process, the emitted electrons carry all the kinetic energy, and the electron energy sum spectrum is a sharp peak at the endpoint $Q_{\beta\beta}$ value of the decay process. In the other two modes the neutrinos take away some of the kinetic energy from the electrons and therefore have a continuous spectrum. A list of the main $\beta\beta$ decaying isotopes, their isotopic abundance and $Q_{\beta\beta}$ values is given in Table 4.1.

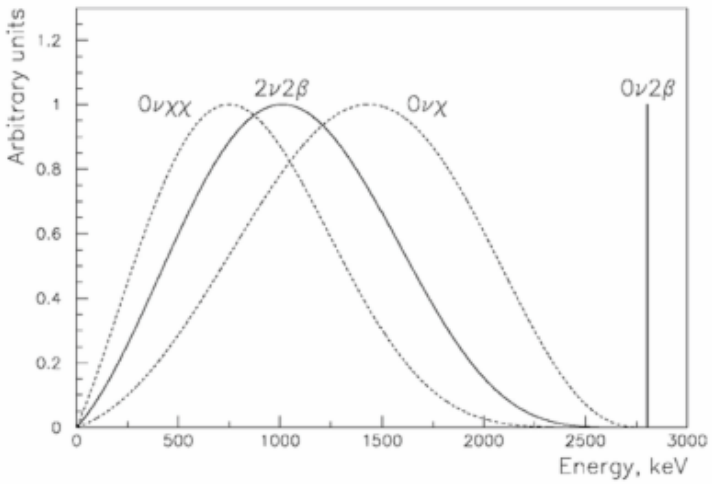

Figure 4.4: Electron sum energy spectra of $2\nu\beta\beta$ decay, $0\nu\beta\beta$ decay, double Majoron and Majoron decay [79].

4.1 $\beta\beta$ Decay Rates

4.1.1 $2\nu\beta\beta$ Decay Rate

The general equation for the ground state to ground state ($0^+_{g.s} \rightarrow 0^+_{g.s}$) decay rate for $2\nu\beta\beta$ decay is given by

$$(T^{2\nu}_{1/2})^{-1} = G^{2\nu} \mid M_{2\nu} \mid^2, \tag{4.7}$$

where $G^{2\nu}$ is the phase-space factor and $M_{2\nu}$ is the nuclear matrix element (NME) for $2\nu\beta\beta$ decay.

For the excited states transitions, the decay rate is

$$((T^{2\nu}_{1/2}(0^+))^{-1} = G^{2\nu}(0^+_1) \mid M_{2\nu}(0^+_1) \mid^2, \tag{4.8}$$

where $G^{2\nu}(0^+_1)$ is the phase-space factor and $M_{2\nu}(0^+_1)$ is the nuclear matrix element (NME) for excited state $2\nu\beta\beta$ decay.

These decay rates do not depend on neutrino masses and there is no distinction made between Majorana and Dirac neutrinos. Thus, from the above equations one

can calculate the NME using experimentally obtained measurements of the $2\nu\beta\beta$ decay half-lives.

4.1.2 $0\nu\beta\beta$ Decay Rate

The $0^+_{g.s} \rightarrow 0^+_{g.s}$ decay rate for $0\nu\beta\beta$ decay is

$$(T^{0\nu}_{1/2})^{-1} = G^{0\nu} \mid M_{0\nu} \mid^2 \eta^2, \tag{4.9}$$

where $G_{0\nu}$ is the specific phase space factor for $0\nu\beta\beta$ decay, $M_{0\nu}$ is the NME for the $0\nu\beta\beta$ transition, and η is the lepton number violating parameter. η has different forms for different $0\nu\beta\beta$ decay mechanisms. These mechanisms include light Majorana neutrino exchange, heavy Majorana neutrino exchange, right handed currents, and R-parity violating supersymmetry exchange modes, and others. We can now see how important it is to make an accurate calculation of the NME, because if lepton number conservation violation is observed, i.e. $0\nu\beta\beta$ decay is observed, without the NME we cannot extract η and any new physics. And although there may be different mechanisms responsible for the neutrino mass the Schechter-Valle theorem [80] states that if the $0\nu\beta\beta$ decay is observed, we will definitely know the neutrino is a Majorana particle. Currently the favoured mechanism is the light Majorana neutrino exchange. Studying electron energies and angular correlations can shed some light on the underlying mechanism, and NEMO 3 can provide such topological information, however only the mass mechanism was considered in this thesis, so η is therefore, in this case, the effective Majorana neutrino mass $\langle m_\nu \rangle \equiv \langle m_{\beta\beta} \rangle$. Eq. 4.9 therefore becomes,

$$(T^{0\nu}_{1/2})^{-1} = G^{0\nu} \mid M_{0\nu} \mid^2 \langle m_\nu \rangle^2. \tag{4.10}$$

4.2 Nuclear Structure Theory and Nuclear Matrix Elements

If we observe $0\nu\beta\beta$ decay it will confirm the Majorana nature of neutrinos, but if we have not understood the underlying nuclear structure fully (i.e. the NME)

then we cannot extract accurate values for the effective neutrino mass, make any conclusions about neutrino mass hierarchies, or indeed extract any new physics.

Within nuclear theory, in the past, the nuclide chart was divided into regions according to different types of nuclei, i.e. whether the nuclei are spherical, deformed, or exhibit more complex behaviour, and each of these regions treated by different nuclear models. Now with the huge increase in computing resources these models have been deserted and a new approach adopted. There are now essentially two lines of research: ab initio and mean-field calculations. With the increase in computing power, areas in nuclear theory that have remained unsolvable for years are now being unravelled, and although this has fuelled research in ab initio and mean-field areas, there has been progress in $\beta\beta$ decay theory due to a large extent to the European scientific framework, Ilias [81]. There are currently two $\beta\beta$ decay models (with variations) in use: the quasiparticle random phase approximation (QRPA) and the shell model.

4.2.1 QRPA

Work on the QRPA was started in 1967 by Hableib and Sorenson [82]. It was subsequently first used in terms of $\beta\beta$ decay by Huffman in 1970 [83].

The QRPA is used to calculate the NME connecting the initial and final 0^+ states with the intermediate 1^+ states, where the initial and final states are based on BCS states. (A BCS state is an approximation of the quantum mechanical state of the nuclear system [84].) The QRPA matrices contain two two-body interaction matrix elements. One, a particle-hole (ph) matrix element, is correlated to the repulsive particle-hole interaction, the other is the particle-particle (pp) matrix element, correlated to the attractive particle-particle interaction. Both matrices contain independent interaction constants g^{ph} and g^{pp} [85].

The constant g^{ph} can be left alone as it mostly only affects the giant Gamow-Teller (GT) resonance. The g^{pp}, however, although not affecting the giant GT resonance, has a significant effect on the NME and $\beta\beta$ decay (particularly $2\nu\beta\beta$ decay) and largely within the QRPA framework. In fact, an increase of the g^{pp} past its realistic value can cause the QRPA to become unstable and collapse. Much of the work into

the QRPA has been focused on the g^{pp} problem. Some lines of research have looked at the possibility of fixing a value for the g^{pp} using experimental observables such as $2\nu\beta\beta$ decay, other possibilties are perhaps to look at reducing the sensitivity of the QRPA to the g^{pp}.

There are many variations of the QRPA in competition with each other (such as the renormalised quasiparticle random phase approxmation, the RQRPA), that have tried to address the latter issue, which are summarised in [76].

4.2.2 Shell Model

A good reference source for the first modern shell model calculations is Haxton and Stephenson Jr. [86]. As large scale shell model calculations are difficult and time consuming, work has primarily been restricted to ^{48}Ca, ^{76}Ge, ^{82}Se and ^{136}Xe, with much earlier work focused on ^{48}Ca because it is a doubly magic nucleus and has the least complex nuclear structure to study in terms of $\beta\beta$ decay.

A disadvantage of the shell model is that it includes fewer single particle states than the QRPA. Because of this, correlations of arbitrary complexity within the single particle space can be included [76], but because of these correlations, shell model calculations are harder to carry out.

4.2.3 What Now?

As reported by Alfredo f in the 5th Ilias Annual Meeting held in Jaca, Spain, large scale shell model calculations are now available and soon there will be NME results for all the $0\nu\beta\beta$ decay isotopes with a $Q_{\beta\beta}$ value $> 2\,\mathrm{MeV}$, excepting ^{150}Nd [87]. The QRPA NME results are now compatible (using the same short range correlations) and in general the shell model and QRPA results are now starting to converge. The current status of QRPA and shell model calculations are shown in Fig. 4.2.3. Now there are much smaller discrepancies between the shell model and the QRPA, and there is much more uniformity within certain theoretical frameworks. In fact now the uncertainties in these calculations are dominated by the experimental, rather than theoretical uncertainties, indicating the importance of precise measurements of the $2\nu\beta\beta$ decay half-life. Avignon, Engel and Elliot [76] suggest that an improve-

ment on the shell model calculations would be the best way to reduce differences in approaches. The work on other $\beta\beta$ decay searches, such as excited states decays, will undoubtably provide invaluable results to aide this area of research.

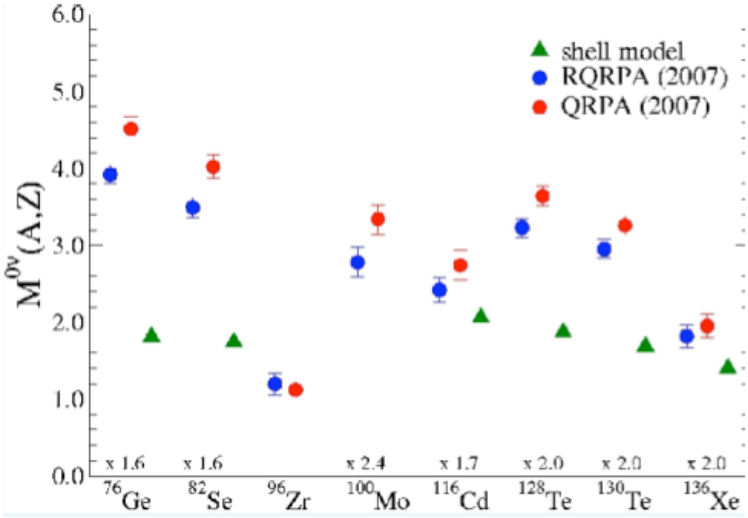

Figure 4.5: Plot of NME values for some of the main $0\nu\beta\beta$ isotopes. The shell model data is from [87] and the QRPA data is from [88].

4.3 Experimental Criteria and Techniques

Searching for $0\nu\beta\beta$ (and $2\nu\beta\beta$) decay is an extremely sensitive process. As experiments are looking for a peak in the energy spectrum within a sea of backgrounds, they concentrate on background suppression. To put this more quantitatively, $0\nu\beta\beta$ lifetimes are $> 10^{25}$ yrs, whereas the lifetimes of the natural radioactivity we want to suppress are $\sim 10^{10}$ yrs, giving 10^{15} more events.

The experimental criteria for $0\nu\beta\beta$ decay experiments have been discussed most recently by [76] and [89]. Below is a comprehensive list outlining these criteria.

- Approximately 1 tonne of isotope is needed to search in the 50 meV region of interest indicated by oscillation experiments. Because of the difficulties in suppressing backgrounds with larger and larger masses, the scaling of experiments up to 1 tonne should be done by incrementing the mass in steps. The next goal

of experiments is to reach a mass of ∼100 kg.

- Low contamination of source and detector components is key and this requirement leads onto other specific criteria.
- As backgrounds scale with the size of detector, a small detector would help to minimise backgrounds.
- A small detector would also minimise the amount of external background shielding, and possible contamination associated with these components.
- Minimising the need for maintenance and easy operation of the detector is important, as these experiments are situated in underground laboratories and are in continuous operation for at least five years, sometimes longer.
- Energy resolution is an important factor. Good detector resolution prevents the tail end of the $2\nu\beta\beta$ decay spectrum from becoming a background itself and produces a good s/b ratio.
- Event reconstruction provides a powerful tool for background rejection by event topology.
- Isotopes with a high $Q_{\beta\beta}$ value provide a natural suppression of backgrounds and have a larger phase space.
- The natural isotopic abundance of the isotope is also important in terms of isotopic enrichment.
- A good knowledge of the nuclear theory of the isotope is also a requirement, as some calculations associated with these, such as the NME, are better known for some isotopes.

No experiments dedicated to the search for $0\nu\beta\beta$ decay, past or present, have managed to include all these experimental criteria in their detector design. A list of average $2\nu\beta\beta$ decay half-life values is given in Table 4.1 and $0\nu\beta\beta$ half-life results are given in Table 4.2.

Double beta decay rates can be measured by either indirect methods or direct methods. A complete chronological order (up to 2001) of double beta decay measurements, for all modes and methods, for each of the isotopes mentioned in Tables 4.1 and 4.2 can be found in [90] and a list of the status of $0\nu\beta\beta$ experiments is given in Table 4.3.

Isotope	**%**	$Q_{\beta\beta}$ **(keV)**	$T^{2\nu}_{1/2}$ **(yrs)**
^{48}Ca	0.19	4271	$4.2^{+2.1}_{-1.0} \times 10^{19}$
^{76}Ge	7.4	2039	$1.5 \pm 0.1 \times 10^{21}$
^{82}Se	8.73	2995	$0.9 \pm 0.7 \times 10^{20}$
^{96}Zr	2.8	3350	$2.0 \pm 0.3 \times 10^{19}$
^{100}Mo	9.6	3034	$7.1 \pm 0.4 \times 10^{18}$
^{100}Mo(*)	9.6	1904	$6.8 \pm 1.2 \times 10^{20}$
^{116}Cd	7.49	2802	$3.0 \pm 0.2 \times 10^{19}$
^{128}Te	31.69	868	$2.5 \pm 0.3 \times 10^{24}$
^{130}Te	33.8	2533	$0.9 \pm 0.1 \times 10^{21}$
^{150}Nd	5.6	3367	$7.8 \pm 0.7 \times 10^{18}$
^{238}U	99.3	1145	$2.0 \pm 0.6 \times 10^{21}$

Table 4.1: $2\nu\beta\beta$ decay results showing each isotope with it's natural abundance (%) $Q_{\beta\beta}$ value and average $T_{1/2}$ values [91]. This table does not include the latest results from NEMO 3 (including the results in this thesis) which are being prepared for publication.

4.3.1 Indirect Experiments

Indirect methods include geochemical and radiochemical measurements. In fact the first evidence of $\beta\beta$ decay was found by both these types of experiment. Geochemical and radiochemical experiments do have similar elements, but utilise slightly different aspects of nuclear decay to achieve their results.

Geochemical Experiments

Geochemical experiments involve studying mineral ores billions of years old. The theory behind the experiment is that the nuclei inside the ore will have undergone $\beta\beta$ decay, and the daughter nuclei will have accumulated inside the ore since it was formed. The mineral ores should therefore contain an excess of the daughter isotope, which can then be measured. This method is extremely sensitive because of the long 'experimental time'. The great disadvantage of the geochemical method lies in the fact that it is not possible to determine the underlying $\beta\beta$ decay mode that formed the daughter isotopes, i.e. whether the parent isotope has undergone $0\nu\beta\beta$ decay or $2\nu\beta\beta$ decay. Another factor which affects these experiments is that before any measurement is taken, it must be established the mineral ore did not contain any of the daughter isotope when it was first formed. To address this issue the chemical nature of the daughter isotope must be different from that of the parent isotope. This restricts the choice of mineral ore to be studied, and to date there have been experiments with positive results only from ^{82}Se, ^{128}Te and ^{130}Te, where the daughter isotope is a noble gas. These processes are outlined in Eqs. 4.11 - 4.13.

$$^{82}Se \rightarrow^{82} Kr + 2e + 2\bar{\nu_e} \tag{4.11}$$

$$^{128}Te \rightarrow^{128} Xe + 2e + 2\bar{\nu_e} \tag{4.12}$$

$$^{130}Te \rightarrow^{130} Xe + 2e + 2\bar{\nu_e}. \tag{4.13}$$

A good reference for geochemical experiments from first results to 1991 can be found in [92].

Geochemical experiments have had a mixed success record, and in some cases have been extremely successful. The first experiment was carried out as far back as 1949 by Inghram and Reynolds with ^{128}Te and ^{130}Te [93] with a first result for ^{130}Te given by the same team in 1950 of $T_{1/2} = 1.4 \times 10^{21}$ yrs [94]. Problems have been associated with this measurement in general, due to the possibility of the xenon gas escaping from the sample or later alteration of the ore itself. And there is still a

discrepancy between geochemical results and nuclear theory calculations.

More successful have been the geochemical measurements of ^{82}Se. The first attempt was made in 1967 by Kirsten, Gentner and Shaeffer [95], with a positive result obtained in 1969 [96]. In fact the geochemical result of 1986 [97] was confirmed by the direct experiment of Michael Moe [98], these results showing that the dominant $\beta\beta$ decay mode for ^{82}Se is $2\nu\beta\beta$ decay.

Radiochemical Experiments

Radiochemical experiments use the fact that some $\beta\beta$ decay daughter nuclei are themselves radioactive, and are also so rare that they can only be produced by $\beta\beta$ decay. These daughter isotopes are short lived, this means that the atmosphere surrounding the experiment will not contain any of the daughter isotope, and will be free of contamination, it is also a great advantage compared to the geochemical measurements, as the age of the sample is no longer an important factor. Typical candidates are ^{232}Th, ^{238}U and ^{244}Pu.

If we take ^{238}U as an example (which was first measured in 1950 by Levine, Ghiorso and Seaborg [99]). The daughter isotope, plutonium, is first chemically isolated, and then measured for the presence of α-particles. The number of α-particles then indicates the number of plutonium atoms present in the original sample.

4.3.2 Direct Experiments

Direct methods of detection involve: semiconductor and cryogenic type detectors, which have excellent energy resolution, but and very limited particle recognition capabilities, scintillator experiments, which have good resolution and some particle recognition capabilities, and tracker experiments, which have poor energy resolution compared to the various types of experiments mentioned above, but excellent particle recognition capabilities.

Semiconductor Experiments

The Claimed Observation of $0\nu\beta\beta$ Decay

The Heidelberg-Moscow experiment is the most sensitive $0\nu\beta\beta$ decay experiment

to date. In 2001 a small group of the Heidelberg-Moscow collaboration claimed to have observed $0\nu\beta\beta$ decay [74], [100], and obtained the result, $T^{0\nu}_{1/2}(^{76}\mathrm{Ge}) = 1.19^{+2.99}_{-0.50} \times 10^{25}$ yrs, with $\langle m_{\beta\beta}\rangle = 0.24 - 0.58$ eV (using one particular NME) [101], but they have received some criticism (not least from another subset of the same collaboration [102]) due to the background being underestimated and systematic problems with identifying certain backgrounds. All five of the Heidelberg-Moscow Ge detectors, enriched to 86% in ^{76}Ge and weighing 11.5 kg, were finally installed in 1995, although the experiment began taking data in 1990. IGEX (International Germanium EXperiment) used a similar experimental technique to that of the Heidelberg-Moscow experiment, and produced a very competitive result of $T^{0\nu}_{1/2}(^{76}\mathrm{Ge}) > 1.57 \times 10^{25}$ yrs [73], [103].

Isotope	**Technique**	$T^{0\nu}_{1/2}$ **(yrs)**	$\langle m_{\beta\beta}\rangle$ **(eV)**	**Ref.**
^{48}Ca	CaF_2 scintillating crystals	$> 1.4 \times 10^{22}$	$< 7.2 - 44.7$	[104]
^{76}Ge	^{enr}Ge detector	$1.19^{+2.99}_{-0.50} \times 10^{25}$ (3σ)	$0.24 - 0.58$	[101]
^{76}Ge	^{enr}Ge detector	$> 1.57 \times 10^{25}$	$< 0.33 - 1.35$	[73]
^{82}Se	Foils and tracking	$> 2.1 \times 10^{23}$	$< 1.2 - 3.2$	[105]
^{100}Mo	Foils and tracking	$> 5.8 \times 10^{23}$	$< 0.6 - 2.7$	[105]
^{116}Cd	$CdWO_4$ scintillating crystals	$> 1.7 \times 10^{23}$	< 1.7	[106]
^{128}Te	Geochemical	$> 7.7 \times 10^{24}$	$< 1.1 - 1.5$	[107]
^{130}Te	TeO_2 Bolometers	$> 1.8 \times 10^{24}$	$< 0.2 - 1.1$	[108]
^{136}Xe	Liquid Xe scintillator	$> 4.5 \times 10^{23}$	$< 0.8 - 5.6$	[109]
^{150}Nd	Foils and tracking	$> 3.6 \times 10^{21}$		[110]

Table 4.2: $0\nu\beta\beta$ decay results.

It is vital that these results are either confirmed or disproved, and another Ge experiment would be the ideal choice to do this, as apart from the excellent energy resolution, many of the backgrounds have already been studied.

Two experiments that aim to study the region highlighted by the Heidelberg-Moscow claim are GERDA (GERmanium Detector Array) [111] and MAJORANA [112]. Both experiments will be using detector segmentation, pulse shape discrimi-

nation, and Ge enriched to 86% in ^{76}Ge.

GERDA will use an array of naked Ge detectors completely immersed in liquid argon. There will be two phases (with a possible third phase) of the experiment. In the first phase GERDA will use 5 detectors from the Heidelberg-Moscow experiment, and 3 detectors from IGEX, totalling 17.9 kg of enriched Ge, and giving a half-life sensitivity of $\sim 3 \times 10^{25}$ yrs. In the second phase an additional 37.5 kg of enriched Ge will be installed, giving a half-life sensitivity of $\sim 1.4 \times 10^{26}$ yrs, which corresponds to a $\langle m_{\beta\beta} \rangle$ of $\sim$124 meV.

MAJORANA will consist of 8 modules, each containing 57, 1.1 kg of Ge detectors contained in cryostats. The final design of the experiment has not yet been completed. MAJORANA's eventual half-life sensitivity may reach $\sim 5.5 \times 10^{26}$ yrs after an exposure of 0.46 tonne-yrs, corresponding to $\langle m_{\beta\beta} \rangle \sim 61$ meV [76]. It is possible that both the GERDA and MAJORANA experiments will join forces to increase the sensitivity even further. As they are using different technologies, whichever experimental technology performs better will then be used in the combined experiment.

COBRA (Cadmium telluride 0-neutrino Beta decay Research Apparatus) [113] is currently in the R&D stage with one running prototype. COBRA uses CdZnTe semiconductor crystals (CZT detectors). These CZT detectors contain 9 isotopes and can be used for studying β decay modes other than $0\nu\beta\beta$ decay. ^{116}Cd, ^{130}Te, ^{114}Cd, ^{70}Zn and ^{128}Te all decay via the $\beta^-\beta^-$ mode, whereas ^{76}Zn, ^{106}Cd, ^{108}Cd, ^{120}Te decay via $\beta^+\beta^+$, β^+ EC and EC EC modes. ^{116}Cd is the favoured isotope for the $0\nu\beta\beta$ decay search as it has the highest $Q_{\beta\beta}$ value. The finished detector will hold 64,000 1 cm^3 CZT detectors, having a total mass of 418 kg, with 183 kg of Cd enriched to 90% in ^{116}Cd. The experiment aims to reach a half life sensitivity $> 10^{26}$ yrs.

Cryogenic Experiments

The cryogenic technique for $0\nu\beta\beta$ decay searches was first proposed in 1984 by Fiorini and Ninikoski [114] and involves using bolometers containing decay isotope, running at extremely low temperatures where the crystals have very small specific heats. According to the Debye law the dependence of the heat capacity of the

crystals at low temperature is proportional to $(T/T_\Theta)^3$ where T_Θ is the Debye temperature of the crystal. So an energy deposit of a few keV inside a crystal (i.e. from electrons emitted during $\beta\beta$ decay) would result in a measurable temperature rise T. As T is very small, sensitive thermistors are required to measure the change in temperature. This type of experiment has very good energy resolution. The first experiment to use this technique was MIBETA [115], essentially the precursor to the CUORE (Cryogenic Underground Observatory of Rare Events) and CUORICINO experiments.

CUORICINO is a running experiment using bolometers made from crystals of TeO_2 (each crystal is 38% ^{130}Te) operating at temperatures of 10 mK [108]. Each bolometer measures $5 \times 5 \times 5\,\mathrm{cm}^3$ and is fixed into a layered tower structure, the total weight of the crystals is 41 kg. The most recent lower limit is $T^{0\nu}_{1/2}(^{130}\mathrm{Te}) \geq 3.0 \times 10^{24}$ yrs [116].

CUORE is the next generation experiment currently in the R&D phase [117]. It will consist of an array of 19 CUORICINO-type towers. All in all it will hold 988 760 g bolometers, containing 750 kg of TeO_2 and 200 kg of ^{130}Te. Their expected sensitivity is of the order $T^{0\nu}_{1/2}(^{130}\mathrm{Te}) \approx 2.5 \times 10^{26}$ yrs corresponding to $\langle m_{\beta\beta} \rangle$ limits in the range 45-53 meV according to the selected NME.

Scintillator Experiments

The CANDLES (CAlcium fluoride for studies of Neutrinos and Dark matter by Low Energy Spectrometer) experimental technique [118] is based on that of ELEGANTS VI (ELEctron GAmma-ray NeuTrino Spectrometer VI), which used europium-doped CaF_2 crystals. ELEGANTS VI obtained a new limit on the $0\nu\beta\beta$ decay of ^{48}Ca of $T^{0\nu\beta\beta}_{1/2} > 1.4 \times 10^{22}$ yrs, which corresponds to $\langle m_{\beta\beta} \rangle < 23$ eV. This experiment is also mentioned in Sec. 8.2.5. CANDLES will use un-doped CaF_2 scintillators immersed in liquid scintillator. CANDLES III, the current incarnation, will use 60 of these crystals totalling 191 kg. The finished detector will hold several tonnes of CaF_2 and will aim to reach a sensitivity of $\langle m_{\beta\beta} \rangle \approx 0.1$ eV.

Two other scintillator experiments that are at the proposal stage are SNO+ [119] and XMASS [120]. SNO + proposes to use SNO by replacing the heavy water with

isotope loaded liquid scintillator, which would allow the newly formed collaboration to study low energy solar neutrinos, geoneutrinos, long baseline reactor neutrinos and $0\nu\beta\beta$ decay. The favoured isotope for this is ^{150}Nd. Because of issues with low energy resolution, $2\nu\beta\beta$ decay will be one of the main background considerations, but it may be possible to separate the two signals if $\langle m_{\beta\beta}\rangle$ is in the degenerate mass-scale region.

XMASS (Xenon detector for weakly interacting MASSive particles) is a dark matter search experiment using 100 kg of natural Xe in liquid form. There is currently a proposal to expand the experiment to 1-20 tonnes. Studies with the current detector have shown that a re-configuration of the detector would be needed for a $0\nu\beta\beta$ decay search and so the experiment will be used to study dark matter and solar neutrinos.

Tracker Experiments

These types of experiments generally have the source separate from the detector and come in the form of TPCs and tracking-calorimeter experiments, where the emitter is either a filling gas or in the form of thin foils. They normally have good particle recognition capabilities and in some cases can extract kinematic properties of particles, which is a very powerful tool for background rejection. Generally the energy resolution of these experiments is poor compared to germanium and bolometer type experiments .

The first measurement of $2\nu\beta\beta$ decay using a direct experimental technique was carried out in 1987 [98]. Michael Moe and colleagues measured the $2\nu\beta\beta$ decay of ^{82}Se with a TPC and obtained a half-life result of $T^{2\nu}_{1/2}(^{82}\text{Se}) = 1.8^{+0.8}_{-0.3} \times 10^{20}$ yrs (68% C.L.).

The ELEGANTS V (ELEctron GAmma-ray NeuTrino Spectrometer V) detector [121] consisted of drift chambers filled with a mixture of He gas and CO_2, scintillators, PMTs, NaI detector arrays and ^{100}Mo and ^{116}Cd source foils. The proposed MOON (Molybdenum Observatory of Neutrinos) [122] experimental technique is based on the ideas behind ELEGANTS V.

MOON is a dual purpose detector. Not only will it be used to search for the

$\beta\beta$ decay of ^{100}Mo, it will also be used to detect solar neutrinos. It is made up of modules, each containing a thin foil of enriched Mo, which is placed between two position sensitive detector planes and two plastic scintillator planes. Backgrounds are rejected because of the localisation of the β tracks, and so the main background for this experiment is the tail of the $2\nu\beta\beta$ decay process. Because of this, improving the energy resolution is the main consideration of the current R&D programme. The MOON collaboration aims to achieve a measurement of $\langle m_{\beta\beta} \rangle$ down to 50 meV with 1 tonne of ^{100}Mo.

Experiment	**Isotope**	**Technique**	**Status**
CANDLES	^{48}Ca	CaF_2 scintillating crystals	Prototype
COBRA	^{116}Cd	CZT semiconductor detector	Prototype
CUORE	^{130}Te	TeO_2 bolometer	Prototype
CUORICINO	^{130}Te	TeO_2 bolometer	**Running**
DCBA	^{150}Nd	^{enr}Nd foils with tracking	Development
EXO	^{136}Xe	Liquid ^{enr}Xe TPC/scintillator	Construction
GERDA	^{76}Ge	^{enr}Ge semiconductor detector	Construction
MAJORANA	^{76}Ge	^{enr}Ge semiconductor detector	Proposal
MOON	^{100}Mo	^{enr}Mo foils and scintillator	Proposal
NEMO	^{100}Mo/^{82}Se	^{100}Mo/^{82}Se foils with tracking	**Running**
SNO+	^{150}Nd	^{150}Nd loaded liquid scintillator	Proposal
SuperNEMO	^{150}Nd or ^{82}Se	^{150}Nd or ^{82}Se foils with tracking	Development
XMASS	^{136}Xe	Liquid Xe	Prototype

Table 4.3: $0\nu\beta\beta$ decay experiments: status and techniques [76]

The DCBA (Drift Chamber Beta Analyser) experiment [123] will be searching for the $0\nu\beta\beta$ decay of ^{150}Nd. It will consist of tracking chambers filled with He gas, a solenoid magnet, cosmic-ray veto detector and source foils. It will be able to obtain information on the momentum of the β particles and event vertex. The experiment will be run in two phases: DCBA-I will contain natural Nd and DCBA-II will contain Nd_2O_3 enriched to 90% ^{150}Nd. The DCBA collaboration aim to reach

a sensitivity for $\langle m_{\beta\beta} \rangle$ of 0.12 eV.

EXO (Enriched Xenon Observatory) [124] will be searching for the $0\nu\beta\beta$ decay of ^{136}Xe. EXO is a TPC experiment that will use between one and ten tonnes of enriched (80%) ^{136}Xe. The EXO experiment will have two phases. EXO-200 is a 200 kg R&D phase and EXO will be a scaled up version of EXO-200 with the addition of a system to trap and identify the daughter ^{136}Ba ion using laser spectroscopy thus reducing backgrounds dramatically. EXO-200 plans to reach a sensitivity to $\langle m_{\beta\beta} \rangle$ of 0.3 eV.

NEMO 3 is the only running experiment of this kind at the moment, and will be discussed in greater detail in the following chapter. SuperNEMO [125] on the other hand, is a next generation experiment with an experimental technique based on that of NEMO 3. SuperNEMO is a tracking-calorimeter experiment with a modular design. Each module will hold 5 kg of either enriched ^{150}Nd or ^{82}Se. A separate detector, BiPo, is being developed to measure the activity of ^{214}Bi in the source foils, which will be instrumental in background rejection. SuperNEMO's expected sensitivity to the effective neutrino mass is $\langle m_{\beta\beta} \rangle < 0.05 - 0.1$ eV.

Chapter 5

The NEMO 3 Experiment and Detector

5.1 General Description

NEMO 3 is based in the Laboratoire Souterrain de Modane (LSM) on the French Italian border in a tunnel linking Modane to Bardonnecchia. The NEMO 3 detector is cylindrical, and divided into twenty equal sectors. It is ∼6 m in diameter and 4 m high. Particle identification is possible through information from the tracker, and energy and time measurements are given by the calorimeter. A schematic of a section of the detector is shown in Fig. 5.1. The detector has four main components: the tracker, calorimeter, source foils and shielding. This chapter contains descriptions of these four components, and also describes the detector electronics and calibration.

5.2 Tracker

The tracking chamber contains 6180 octagonal, vertical wire drift cells, which operate in geiger mode. The gas used to fill the wire chamber is a mixture of 95% helium, 4% ethyl alcohol, and 1% argon at 10 mbar above atmospheric pressure. The proportion of helium and ethyl alcohol/argon in the tracking chamber was chosen carefully. Helium is light and has a low density allowing the electrons to lose as little energy as possible (∼30 keV). The ethyl alcohol/argon component acts as a

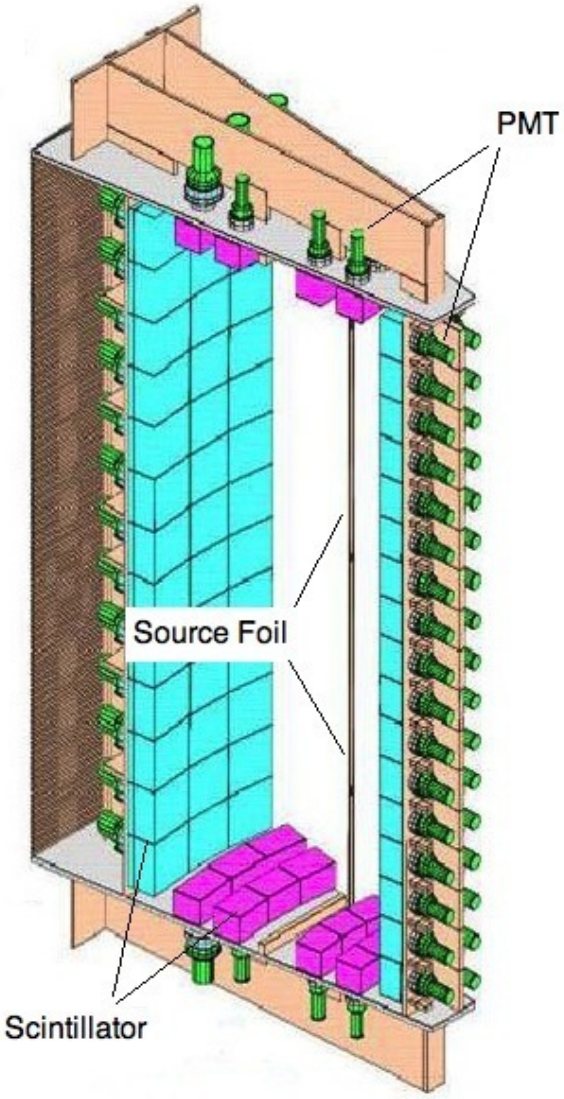

Figure 5.1: A cut-away schematic of a section of the NEMO 3 detector, showing the position of the PMTs, scintillators and source foils.

quencher to absorb UV photons.

The drift time and plasma propagation times are recorded from the geiger cells. Each cell has a central anode wire surrounded by eight ground wires. Each cell shares wires from another cell to minimise the wires required to make up the chamber. A cathode ring circles the end of each cell, with the anode running through the centre and the ground wires outside of the ring. The chamber is set out in a 4-2-3 layer configuration on each side of the source foils, with four layers of cells near to the

source foils (to give accurate vertex information) two layers in the middle of each tracker section and then three layers near to the scintillators. A diagram of the Geiger cell layout for one sector is shown in Fig. 5.2.

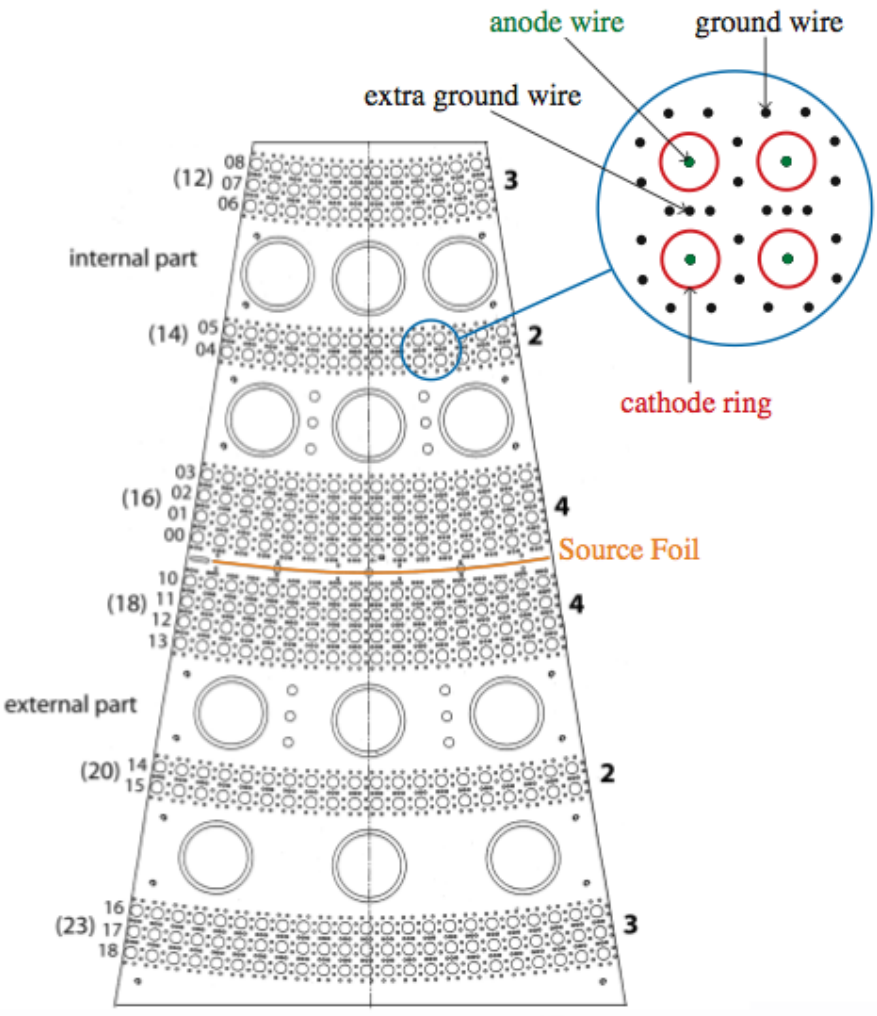

Figure 5.2: The top view of the Geiger cell layout for one sector with a detail of four Geiger cells [126]. The diagram highlights the 4-2-3 layer configuration of the internal and external parts of the sector. A basic Geiger cell consists of an anode wire surrounded by 8 ground wires, with the cathode ring circling the end of each cell. The large circles in the diagram relate to the positions of the calorimeter counters on the end caps of the sector (coloured pink in Fig. 5.1).

The operating voltage of the anode wires is 1800 V. When a charged particle passes through the gas mixture, the ionised gas yields approximately 6 electrons/cm. These ionisation electrons drift towards the anode wire in the centre of the wire cell. The drift time for these electrons is used to calculate the transverse position of the particle in the cell. A geiger plasma, which develops from the avalanche of ionisation electrons close to the anode wire, propagates along the anode wire (at ∼6-7 cm/μs) and is then detected by the cathode rings at both ends of the cell. These propagation times are used to calculate the particle's longitudinal position.

5.3 Calorimeter

Each of the 1940 calorimeter counters is made up of a block of plastic scintillator, light guide and PMT (3-inch and 5-inch). The counters cover the cylindrical walls surrounding the tracking volume of the detector and partially cover the top and bottom end caps. They are used to obtain particle energy measurements (up to 12 MeV), time of flight (TOF) measurements and also act as a trigger. To minimise energy losses, the scintillator blocks are situated inside of the helium gas mixture of the tracking chamber. PMTs can age dramatically when in contact with helium, so to minimise this aging effect, the PMTs are fixed outside of the gas mixture.

5.3.1 Scintillator Blocks and Light Guide

There are 480 end-cap scintillators and 1460 wall scintillators. Each block is 10 cm thick. This gives a high efficiency (50% at 500 keV) for detecting γ-rays and aids in background rejection. They have different shapes, seven in all, depending on which part of the detector they are situated, to fit the cylindrical design of the detector.

The polystyrene scintillators are doped with a solid solution of scintillation agent, p-Terphenyl (PTP) and a wavelength shifter, 1.4-di-(5-phenyl-2-oxazoly)benzene (POPOP). The end-cap scintillators are 98.75% polystyrene, 1.2% PTP and 0.5% POPOP. The wall scintillators are 98.49% polystyrene, 1.5% PTP and 0.01% POPOP. The composition of the end-cap and wall scintillators is different because of political and economic reasons, rather than any scientific criteria. The INR Kiev-Kharkov

collaboration manufactured the end-cap scintillors, and JINR (based in Russia) manufactured the wall scintillators. To improve light collection, five layers of teflon are wrapped around the lateral faces of each of the blocks. Each block is then covered with aluminised mylar, this protects it from ambient light and plasma from the tracker, it also further improves on the light collection.

The light guides are made of polymethylmethacrylate, and have the dual purpose of acting as the interface between the scintillator and the PMTs, and also protecting the PMTs from the helium inside the tracking chamber.

5.3.2 PMTs

The 3-inch and 5-inch PMTs were specially manufactured for NEMO 3 by Hamamatsu. They are made of glass with low radioactivity, and other components with a low level of contamination. Each PMT has a μ-metal shield surrounding it to protect it from the Earth's magnetic field. The average radioactivity measurements for these PMTs are given in Table 5.1, whereas the total radioactivity of the PMTs are given in Table 5.2. The 3-inch and 5-inch PMTs were made to fit the different shapes of the scintillator blocks. For example, 5-inch PMTs are coupled to the scintillator blocks on the edge of the sector walls and the outside layer of the end caps, 3-inch PMTs are coupled to the inside layers of the end caps, and some parts of the sector walls.

PMT	^{40}**K (Bq/PMT)**	^{214}**Bi (Bq/PMT)**	^{208}**Tl (Bq/PMT)**
3" PMT (R6091)	0.34	0.083	5×10^{-3}
5" PMT (R6594)	0.53	0.24	0.014

Table 5.1: Average radioactivity measurements for NEMO 3 Hamamatsu 3" and 5" PMTs measured using HPGe (High Purity Germanium) detectors [126].

PMT	^{40}K (Bq)	^{214}Bi (Bq)	^{208}Tl (Bq)
3" PMTs	354	86	5.2
5" PMTs	477	216	12.6
ΣPMTs	831	302	17.8

Table 5.2: Total radioactivity measurements for NEMO 3 Hamamatsu 3" and 5" PMTs measured using HPGe detectors [126].

5.4 Source Foils

The detector contains 10 kg of $\beta\beta$ isotopes distributed throughout the detector in source foils, which are fixed vertically between the two tracking volumes of the detector. Fig. 5.3 illustrates how the sources are distributed in the detector. There were several parameters that were taken into account for selecting the NEMO 3 isotopes, the collaboration used a mixture of these criteria, not basing their choice on any one specific parameter:

- The $Q_{\beta\beta}$ value of the isotope.
- The nuclear matrix elements for both the $0\nu\beta\beta$ and $2\nu\beta\beta$ decay.
- The amount by which the radioactivity of the isotope could be reduced.
- The natural isotopic abundance of the isotope.
- The type of background expected in the area around the $Q_{\beta\beta}$ value of the isotope.

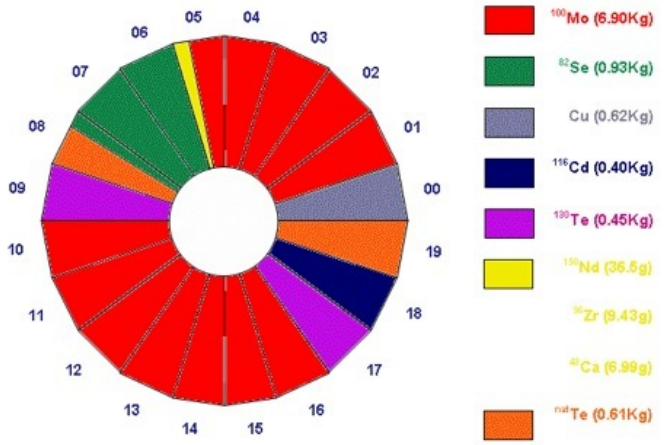

Figure 5.3: The 'Camembert' plot of NEMO 3 sources.

^{116}Cd, ^{82}Se, ^{100}Mo, ^{96}Zr, and ^{150}Nd were chosen because they all have natural isotopic abundances above 2%. They also have $Q_{\beta\beta}$ values above the 2.615 MeV γ-ray from the decay of ^{208}Tl, one of the most troublesome backgrounds for all $\beta\beta$ decay experiments. More emphasis was placed onto the choice of ^{100}Mo; it was the focus of attention for the previous incarnation of NEMO 3, NEMO 2 [127], and was a practical choice in that the enrichment of ^{100}Mo is a tried and tested process, and also as ^{100}Mo has the shortest half-life, the $2\nu\beta\beta$ decay can be measured precisely, as well as the decay to the excited states.

^{48}Ca was included as it has the highest known $Q_{\beta\beta}$ value of 4.27 MeV, but a low natural abundance of 0.187% [128]. ^{130}Te was also added, primarily for $2\nu\beta\beta$ study, because although it has a $Q_{\beta\beta}$ value of 2.53 MeV, it has a high natural abundance of 33% [128]. There are also two sectors inside NEMO 3 which house 621 g of copper and 166 g of natural tellurium. These sectors are virtually free from any internal backgrounds and therefore provide an invaluable insight into external background sources. The external background measured with the copper foils is further discussed in Sec. 7.5. The isotopes and their $Q_{\beta\beta}$ values are listed in Table 5.3.

Isotope	Q value (Mev)
^{100}Mo	3.03
^{82}Se	3.00
^{116}Cd	2.81
^{130}Te	2.53
^{96}Zr	3.35
^{150}Nd	3.37
^{48}Ca	4.27

Table 5.3: $Q_{\beta\beta}$ values of different isotopes used in NEMO3 [129].

5.4.1 Characteristics of the ^{100}Mo Source Foils

Using an enrichment process developed in Russia, 10 kg of Mo samples were enriched to 95.14 - 98.95 ± 0.5% in ^{100}Mo. These samples were found to be too high in radioactive impurities and it was decided to use two purification methods (a physical process and a chemical process) to further purify the samples. These methods resulted in two different types of foils inside the detector: metallic and composite. For both methods the enriched Mo powder was used as a starting point.

The physical process was used to make the metallic foils. It involved transforming the Mo powder into ultrapure mono crystals. The crystals were then rolled out to make metallic strips of between 44 and 63 μmm thick and between 64 and 1445 mm long. These short strips were then cut to 63-65 mm wide, and roughly three to five strips (depending on their length) were attached end to end to produce longer strips ∼2500 mm long. The metallic strips were placed in sectors 2-4 with five strips in sector 1 and another two strips in sector 5. The total weight of the metallic ^{100}Mo in the detector is 2479 ± 5 g.

The chemically purified ^{100}Mo was used to make the composite strips inside the detector. After the purification process, the purified powder was mixed with water and PVA glue, put into a syringe, and heated using ultrasound to form a paste. This paste was then spread onto mylar backing film and dried. These strips were then trimmed to the required size. The composite foils were put into sectors 1 and

5 and then sectors 10-16. The total weight of the composite ^{100}Mo in the detector is 4435 ± 22 g. The activities of the radioactive impurities were measured using HPGe (High Purity Germanium) detectors inside the LSM and are given in Table 5.4.

			^{238}U chain		^{232}Th chain	
Isotope	^{40}**K**	^{235}**U**	^{234}**Th**	^{214}**Bi**	^{228}**Ac**	^{208}**Tl**
^{100}**Mo (Met) 2479 g**	< 5	1.5 ± 0.3	< 15	< 0.39	< 0.5	< 0.11
^{100}**Mo (Com) 4435 g**	< 6	< 0.3	< 15	< 0.34	< 0.3	< 0.10
^{48}**Ca 6.99 g**	< 50	< 2	< 15	< 4	< 6	< 2

Table 5.4: Radioactivity measurements in mBq/kg for ^{100}Mo and ^{48}Ca [126]. All measurements were taken with HPGe detectors.

5.4.2 Characteristics of the ^{48}Ca Source Sector

The $CaCO_2$ sample obtained for NEMO 3 is enriched to $73.2 \pm 1.6\%$ in ^{48}Ca, and was produced by electromagnetic methods in Russia. An additional purification process was also developed by JINR in Russia and the Kurchatov Institute which removes impurities such as ^{226}Ra, ^{228}Ra, ^{60}Co and ^{152}Eu as well as isotopes from the uranium and thorium decay chains. Using this process JINR produced 42.1 g of enriched CaF_2 powder. 24.6 g of the powder was used to make radioactivity measurements with HPGe detectors in the LSM - the results are given in Table 5.4. The rest of the powder (17.5 g) was used to make nine 40 mm diameter discs. The discs form part of the source foils in sector 5 inside the detector. Fig. 8.10 in Sec. 8.4.2 shows the ^{48}Ca discs, just below the ^{96}Zr sample inside the detector. In total there are 6.99 g of ^{48}Ca inside the detector.

5.5 Passive Shielding

The suppression of external backgrounds is imperative for reaching the required sensitivity for this type of experiment. These external backgrounds are significantly reduced by the shielding surrounding the detector. The sources of these backgrounds

are cosmic rays, neutrons released through spontaneous fission from uranium and thorium present in the rocks surrounding the LSM, and γ-rays from natural radioactivity and neutron capture. Fake $\beta\beta$ signals can be produced by γ-rays in several different ways, such as pair creation, the Compton effect, Möller scattering and the photoelectric effect; these are discussed further in Sec. 6.4.

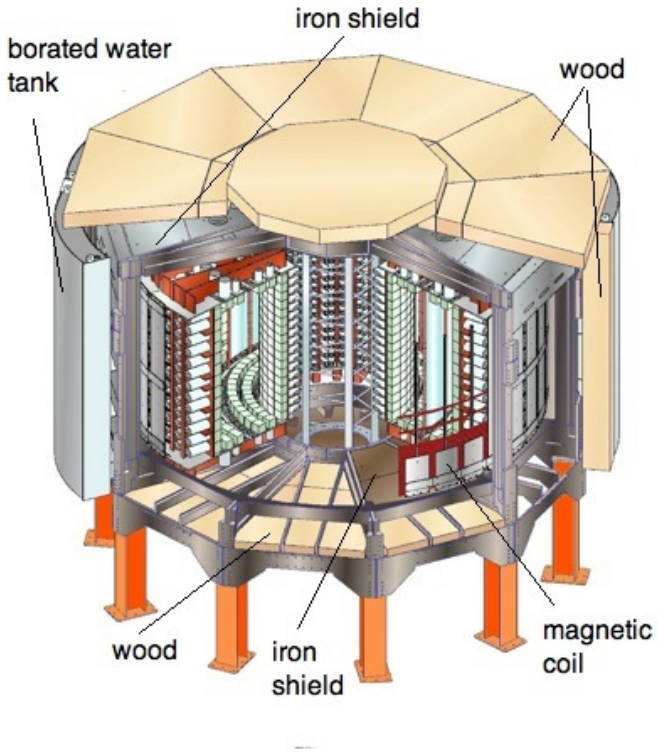

Figure 5.4: A cut-away schematic of the NEMO 3 detector, showing the position of the shielding.

The simplest form of shielding comes from the mountains surrounding the LSM, which give natural shielding against cosmic rays. The 'purpose built' shielding is comprised of tanks containing borated water, an iron shield (which are illustrated in Fig. 5.4), and radon trapping factory.

The iron shield surrounding the detector reduces the γ-ray and thermal neutron backgrounds from the LSM. It is made up of 20 cm thick (radiopure iron) plates attached to the external frame of the detector. Although the iron shielding absorbs thermal neutrons, it is not an effective shield for fast and epithermal neutrons. These neutrons can pass though the iron shield, and can be captured by the copper nuclei

of the NEMO 3 frame and emit high energy photons. The borated water tanks which cover the outside of the iron shield stop fast neutrons and suppress thermal and epithermal neutrons, which reduces the neutron flux reaching the iron shield. This borated water shield is comprised of ten vertical water tanks, 35 cm thick. The detector is then capped top and bottom by 25 cm thick wooden blocks.

5.5.1 Radon Trapping Factory

Three of the main $0\nu\beta\beta$ backgrounds come from radioactive impurities in the source foils (^{214}Bi and ^{208}Tl being the main culprits), the $2\nu\beta\beta$ decay tail, and from radon. Radon decays into the isotopes ^{214}Bi ($T_{1/2} = 19.7\,\text{min}$, $Q_\beta = 3.27\,\text{MeV}$) which is a beta emitter with a β decay energy above that of the $\beta\beta$ decay energy of ^{100}Mo ($Q_{\beta\beta} = 3.03\,\text{MeV}$) and is therefore a very troublesome background.

After one year of data taking the radon deposit on the source foils was found to be $\sim$1 mBq/m^2, fifty times greater than the internal radon contamination, and showing the radon inside the detector to be the main source of background.

The design of the NEMO 3 anti-radon factory [130] is based on that of the Super-Kamiokande air purification system [131]. The fist step for the NEMO 3 anti-radon factory was to install an airtight tent around the detector, Fig. 5.5 is a photograph of the tent around the detector. This was fully closed in May 2004. The next step was the installation of the radon trapping factory. The factory provides a continuous flow of air with a radon level better than 18 mBq/m^3. It consists of a compressor drier, cooling unit (output air $\sim$-50 °C) and two charcoal tanks with 450 g of charcoal in each unit and a heater on the output. The main principle of the trapping facility is the trapping of radon by cooled charcoal. The trapped radon then decays in the charcoal.

The trapping facility along with the tent reduces the amount of radon around the NEMO 3 detector by two orders of magnitude from 15 Bq/m^3 to 0.17 Bq/m^3. The level of radon inside the detector is $\sim$1-2 mBq/m^3, which corresponds to less than 1 event/year in the ^{100}Mo $0\nu\beta\beta$ region of interest, and is quite an acceptable level.

Figure 5.5: Photograph of the radon tent surrounding NEMO 3 after installation.

5.6 Magnetic Coil

The ability to discriminate charged particles is also an important consideration, as high energy photons from neutron captures can produce electron-positron (e^- e^+) pairs (as well as a few $\beta\beta$ events) inside the NEMO 3 source foils, which contribute to $0\nu\beta\beta$ backgrounds. The magnetic coil surrounding the detector allows the identification of e^- e^+ pairs through studying the curvature of the tracks. The vertical 25 Gauss field provided by the coil, rejects 95% of e^- e^+ pairs. The coil is situated between the iron shield and the external wall of the detector (see Fig. 5.4).

To allow access to the detector the coil is made up of 10 sections. Each section is made up of copper rods, connected with copper rings. The cylindrical coil is 5.32 m in diameter, and 2.71 m high, and weighs 5 tonnes. Of its total weight, around 3 tonnes is made up of radiopure copper.

5.7 Electronics

The NEMO 3 electronics, trigger and data acquisition (DAQ) system are designed in a way that enables tests and calibration to be carried out as well as $\beta\beta$ runs. The

calorimeter and tracking detector have separate electronic readouts, meaning the DAQ and triggering can be dependent on both the calorimeter and tracking, or either one or the other.

5.7.1 Calorimeter Electronics

Three large power supplies are used to supply the high voltage (HV) for the PMTs. Three PMTs share one HV channel via a distribution board, each board having four channels which supply twelve PMTs. There are nine distribution boards per sector, making 180 in all.

The analogue signal from the PMTs goes straight to acquisition boards. Each sector has two DAQ cards, one for the 51 exterior PMTs, and one for the 46 interior PMTs. In total there are forty DAQ cards, which are housed in three VMEbus crates.

There are two thresholds - a low and a high threshold. Once the low threshold has been reached the TDC measurements and charge integration begin for 80 ns. When the high threshold is reached, a signal that a PMT has been fired is sent to the first level trigger. The trigger logic then sends a stop signal to the DAQ cards, which stops the TDCs and stores the charge integration. It is only then that the digital conversion begins.

5.7.2 Tracking Detector Electronics

For the tracking detector electronics there are two types of boards, the distribution boards for the secondary voltage distribution, which receive the HV from the three power supplies, and also receive the analogue signals from the anode and cathode rings, and the acquisition board, which receives the analogue signals coming from the distribution board and converts them to digital form. In this way time measurements are acquired for the anode and cathode rings of each cell.

Firstly a signal from an anode wire starts the anode and cathode TDCs. The propagation of the Geiger plasma is then detected by the cathode rings. This signal stops the cathode TDCs to give two values, one from the top ring and one from the bottom.

The anode signal is stopped with a signal from the trigger (STOP-A). There are two distinguishable cases: β events where the STOP-A signal is sent 6.4 μs after the start signal, and α-type events, where the Geiger cells can register delayed hits for up to 704 μs after the STOP-A signal has been sent, which was introduced to exploit the delayed α-particle from ^{214}Po, the daughter isotope of ^{214}Bi (see Sec. 6.2).

5.7.3 Trigger

The trigger system has three levels: T1, T2 and T3. The first level trigger, T1, is based on the number of PMTs required for a readout. T2 is based on the track recognition in the wire chamber. For a normal data taking mode T1 and T2 are used (a two level system). T3 is only used during calibration runs and checks the coincidence between track and scintillator hits. An overview of the NEMO 3 trigger system is shown in Fig. 5.6.

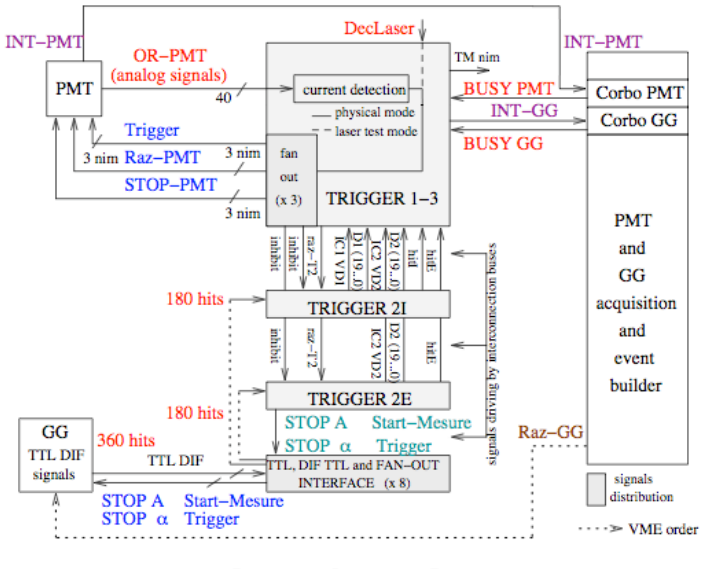

Figure 5.6: The NEMO 3 trigger system [126].

5.8 Energy and Time Calibration

To obtain absolute energy and time measurements, NEMO 3 uses radioactive sources in dedicated calibration runs. These runs are carried out every four weeks. Also daily laser surveys are carried out to test the stability of the PMTs.

5.8.1 Dedicated Calibration Runs

Each sector of the detector has a copper calibration tube fixed on the edge of the source foil, with three pairs of kapton windows. Of each pair, one window is orientated towards the internal wall of the detector and one towards the external wall. The sources are placed in the top of the calibration tube in a long narrow delrin rod, supporting three source holders.

The two sources used for the energy calibration are ^{207}Bi and ^{90}Sr. For low energies, ^{207}Bi provides two conversion electrons of 482 and 976 keV. ^{90}Sr provides electrons of 2.28 MeV from the end of the β spectrum through its daughter ^{90}Y. This fit to three energy points gives an energy calibration up to 3 MeV.

^{60}Co sources are used for timing calibration, which emit two γ-rays in coincidence with energies of 1332 and 1773 keV.

5.8.2 Laser Surveys

The laser surveys are carried out daily to check the absolute energy and time calibration, and to measure the linearity of the PMTs between 0 and 12MeV.

The laser beam is wavelength shifted by a small sphere of scintillator, wrapped in teflon and aluminium, which simulates an electron signal. This signal is sent via optical fibre to the NEMO 3 PMTs, and also six reference PMTs, which are fitted with ^{207}Bi sources. These reference PMTs are used to monitor the stability of the laser light.

Chapter 6

Backgrounds in the NEMO 3 Experiment

6.1 Introduction

The main consideration for this type of low energy experiment is background elimination. Natural radioactivity from isotopes such as potassium (K), uranium (U) and thorium (Th) are carefully considered. Such backgrounds can produce two electron events which mimic $\beta\beta$ decay events. In fact the ability to discriminate between particle types is a unique feature of NEMO 3, and so potentially the only background comes from two electron type events.

NEMO 3 backgrounds are categorised as either *internal* or *external*. Internal background events are defined as events which originate inside the source foil. External events are defined as background events that are generated everywhere else, inside the detector itself and also surrounding the detector.

In terms of the $0\nu\beta\beta$ search, there are three main sources of backgrounds:

- The tail of the $2\nu\beta\beta$ distribution.
- The Interaction of external photons with the detector and source foils.
- The natural radioactivity of the materials used in the construction of NEMO 3, including the source foils.

For the $2\nu\beta\beta$ decay half-life measurement, external photons and natural radioactivity are obviously the only background concerns.

This chapter discusses natural radioactivity, internal and external backgrounds, their origins and, where possible, the techniques used to suppress them.

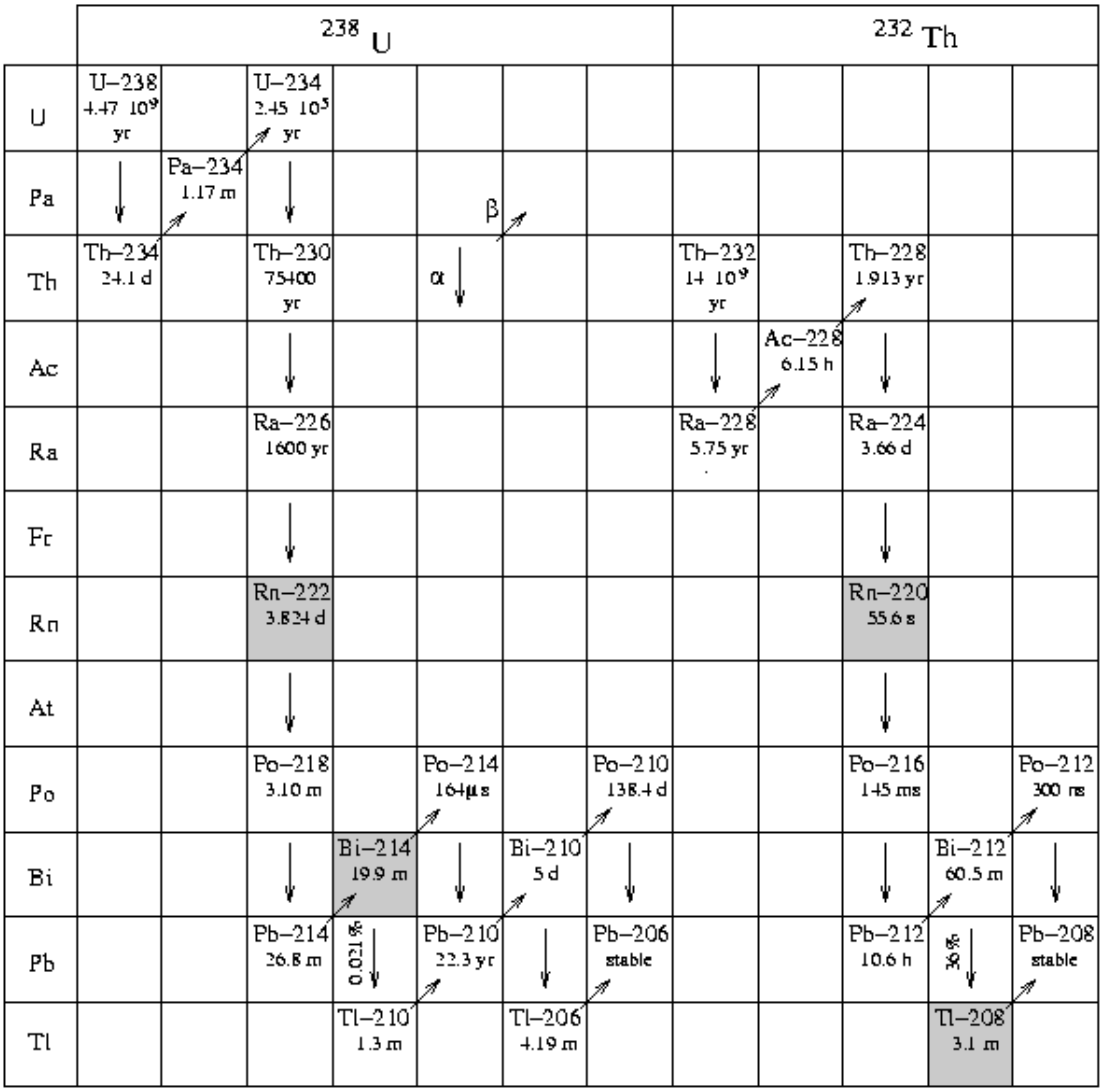

Figure 6.1: The decay chains of ^{238}U and ^{232}Th. The decays of ^{222}Rn to ^{214}Bi, and ^{220}Rn to ^{208}Tl are highlighted in grey.

6.2 Natural Radioactivity

As already mentioned, natural radioactivity comes from isotopes such as potassium, uranium, and thorium. These isotopes have very long half-lives and are present in small amounts in materials that make up the NEMO 3 detector. For the $0\nu\beta\beta$ decay search, the natural decay chain of ^{235}U is discounted as it has a low natural abundance (0.7%) and its family of daughter isotopes do not generate enough energy to be a concern in the $0\nu\beta\beta$ energy region of interest. For the same reason, ^{40}K is another isotope that is not taken into account in the $0\nu\beta\beta$ decay search. For the study of $2\nu\beta\beta$ decay, all these natural radioactivity backgrounds are taken into account, as we are looking at energies from ∼200 keV up to ∼4.3 MeV (in the case of ^{48}Ca).

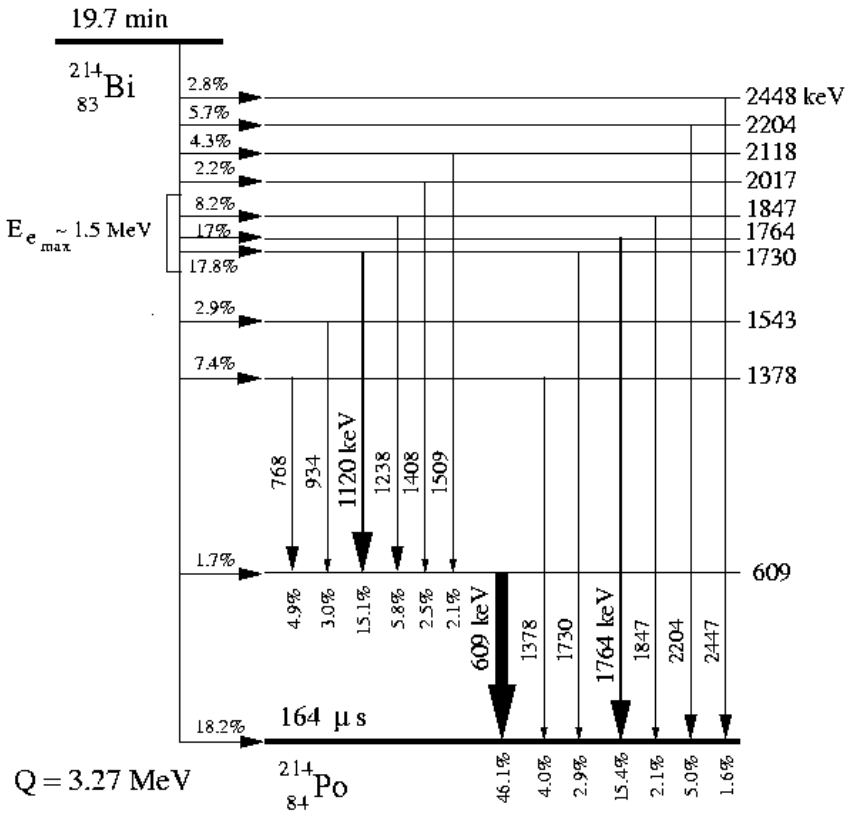

Figure 6.2: Decay scheme of ^{214}Bi. The horizontal arrows are β decays and the vertical arrows are γ decays; the percentages and thickness of the arrows (in the case of the γ decays) indicate the probability of decay.

The natural decay chains of ^{238}U and ^{232}Th are shown above in Fig. 6.1. Of all of their family of daughter isotopes, it is ^{214}Bi and ^{208}Tl that are the most dangerous backgrounds for $0\nu\beta\beta$ searches. Both isotopes are beta emitters with a $Q_\beta > 3\,\text{MeV}$ (^{214}Bi: $Q_\beta = 3.27\,\text{MeV}$, $T_{1/2} = 19.9\,\text{mins}$; ^{208}Tl: $Q_\beta = 4.992\,\text{MeV}$, $T_{1/2} = 3.05\,\text{mins}$). The decay schemes for ^{214}Bi and ^{208}Tl are shown in Fig. 6.2 and Fig. 6.3 respectively.

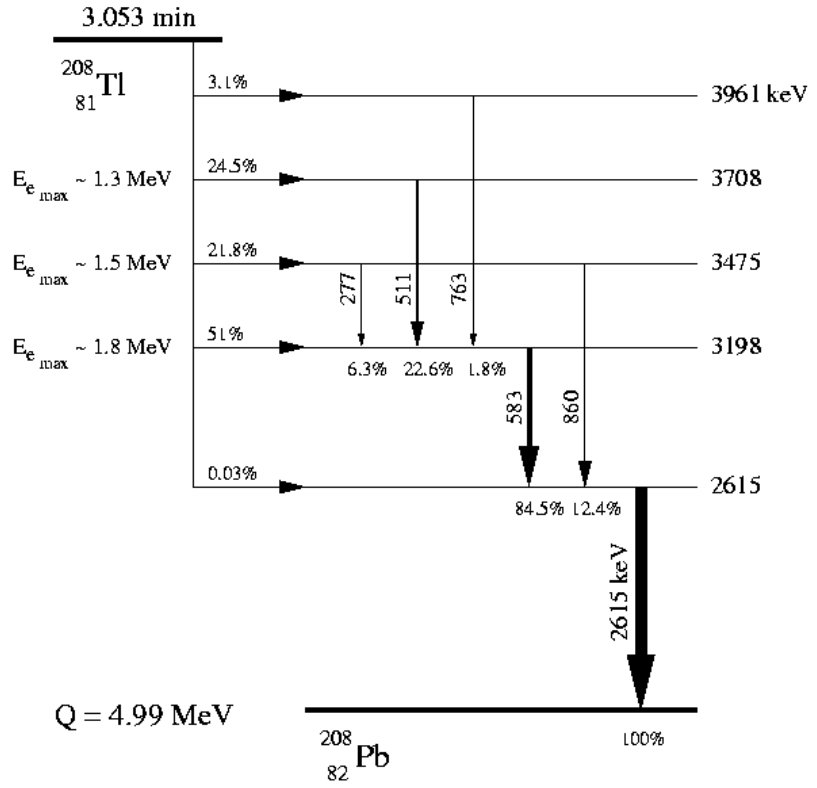

Figure 6.3: Decay scheme of ^{208}Tl. The horizontal arrows are β decays and the vertical arrows are γ decays; the percentages and thickness of the arrows (in the case of the γ decays) indicate the probability of decay.

Radon (^{222}Rn, $T_{1/2} = 3.82\,\text{days}$) and thoron (^{220}Rn, $T_{1/2} = 55.6\,\text{s}$) are the decay products of ^{226}Ra and ^{228}Ra, daughters of the ^{238}U and ^{232}Th decay chains respectively. Subsequent decays of ^{222}Rn and ^{220}Rn produce ^{214}Bi and ^{208}Tl, which have already been mentioned as difficult backgrounds. ^{222}Rn and ^{220}Rn are very diffuse rare gases and are present in the rocks surrounding the NEMO 3 laboratory. These

gases can penetrate concrete walls of the lab and get into the detector, contaminating it. Radon is by far the most troublesome background source for the NEMO 3 experiment, and the NEMO 3 radon trapping facility is employed to reduce its presence inside the detector, as described in Sec. 5.5.1.

Another important background consideration is the Bi-Po decay chain. ^{214}Po is the daughter isotope of ^{214}Bi, which emits α-particles with a 164 μs half-life. The electronics described in Sec. 5.7 are designed to tag these α-particles, which can then be rejected during analysis. This suppresses the ^{214}Bi background.

6.3 Internal Backgrounds

6.3.1 The Tail of the $2\nu\beta\beta$ Distribution

The tail of the electron sum energy spectrum of the $2\nu\beta\beta$ decay of any isotope being studied overlaps with the $Q_{\beta\beta}$ value where the $0\nu\beta\beta$ decay signal is expected. The level of separation of both these signals depends on the energy resolution of the detector, and as it has the same signature as the $0\nu\beta\beta$ decay signal, topological cuts cannot eliminate it, consequently it is the main background consideration for the $0\nu\beta\beta$ decay search. It is therefore treated as an internal background, and a precise knowledge of the $2\nu\beta\beta$ decay half-life of the isotope is used to estimate the number of $2\nu\beta\beta$ events expected in the energy region of interest.

6.3.2 ^{214}Bi and ^{208}Tl Inside the Source Foils

There are three main ways in which a two electron event can be generated inside the source foils:

1. Internal conversion: a nucleus emits a beta particle and its daughter nucleus goes into an excited state. The excitation energy is then transferred to one of the orbital electrons, which is then ejected from the nucleus. This is the most common process.

2. Möller scattering: an emitted beta particle scatters in the source foil and ejects another electron.

3. Compton effect: an emitted beta particle is followed by a de-excitation photon. This photon undergoes Compton scattering in the foil and generates a Compton electron. The double Compton effect can also occur, but is a less likely process.

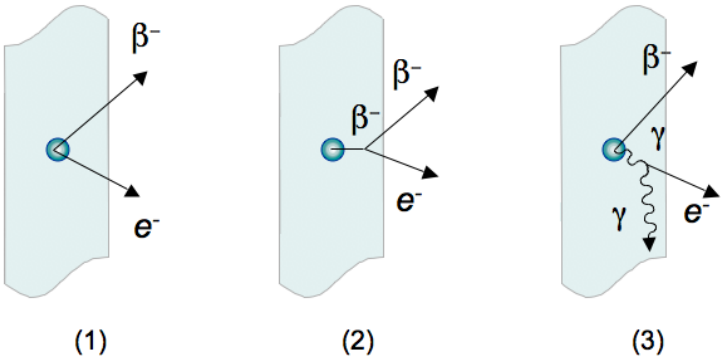

Figure 6.4: The three main ways a two electron event can be generated inside a source foil: (1) Internal conversion (2) Möller Scattering (3) Compton scattering.

These internal background events cannot be rejected during data analysis using any TOF criteria, or vertex cuts, but can be eliminated, only partially, with energy and angular distribution cuts. Because of this, attention is focused on the radio purity of the sources, during manufacture and the enrichment process.

6.4 External Backgrounds

External background events are produced by γ-ray sources. γ-rays interact with the source foils producing $\beta\beta$ type events in five different ways (illustrated in Fig. 6.5):

There are five main ways in which two electron events can be produced by photons in the lab:

1. Pair creation after interaction with a high energy photon.

2. Compton effect followed by Möller scattering.

3. Double Compton effect in the foil.

4. Photoelectric effect followed by Möller scattering.

5. Compton effect followed by the photoelectric effect.

The sources of these photons are natural radioactivity, neutrons via n-γ reactions, and (indirectly) cosmic rays. There are also internal events from crossing electrons. This type of event can be eliminated by TOF cuts and is discussed further in Sec. 7.4.

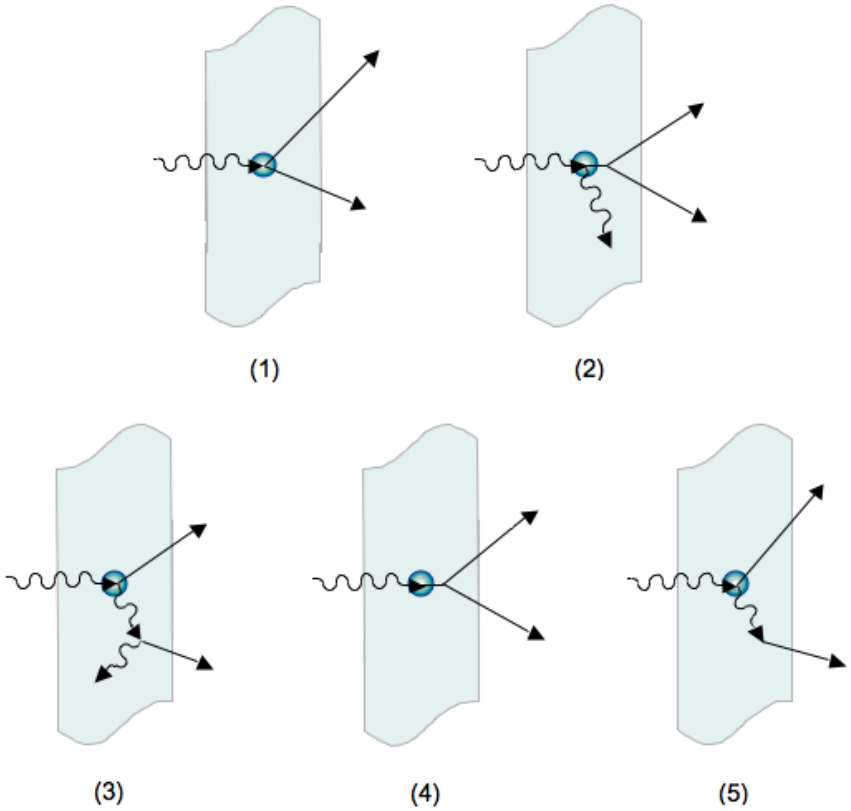

Figure 6.5: The five main ways a two electron event can be generated via an external γ-ray inside the source foils: (1) pair creation after interaction of a high energy photon (2) Compton effect followed by Möller scattering (3) Double Compton effect in the foil (4) Photoelectric effec followed by Möller scattering (5) Compton effect followed by the photoelectric effect. The photons are denoted by wavy arrows and electrons by straight arrows.

6.4.1 Natural Radioactivity in the Detector Components

Traces of natural radioactivity in the detector components cannot be avoided, but can be suppressed by choosing materials with low radioactivity. Table 6.1 lists some of the main detector components and their radioactivity, which were measured by an HPGe detector. The activities of the NEMO 3 PMTs are given in Table 5.1 in Sec. 5.3.2.

Detector Element	**Weight (kg)**	**^{214}Bi (Bq)**	**^{208}Tl (Bq)**
PMTs	600	300	18
Scintillators	5000	<0.7	<0.3
Copper Frame	25000	<25	<10
Steel Frame	10000	<6	<8
μ-metal	2000	<2	<2.7
Wires	1.7	$<10^{-3}$	$<6\text{x}10^{-4}$
Iron Shield	180000	<300	<300

Table 6.1: Activities measured by an HPGe detector, of some of the main detector components of NEMO 3.

6.4.2 Neutrons

Neutrons are released through spontaneous fission from Uranium and Thorium present inside the rock surrounding the lab and the detector components as well as α-n reactions on light nuclei inside the detector components (such as the scintillators). As already discussed in Sec. 5.5 there are several levels of neutron shielding surrounding the tracking volume of the detector, which suppress this type of background.

6.4.3 Cosmic Rays

Another source of background is from cosmic ray muons, although the mountains surrounding the LSM act as a shield against cosmic rays to sufficiently suppress this background source. There is, however, one main source of external background from

cosmic rays which can be very troublesome. This is via spallation reactions, where a muon knocks out a neutron from nuclei from the detector components. This is considered troublesome because unlike the neutrons from the α-n reactions, these neutrons cannot be slowed down by the detector shielding, as they are typically very energetic ($\sim$GeV) and are impossible to stop, although unlikely to create a $\beta\beta$ signature.

Chapter 7

NEMO 3 Analysis - a General Description

7.1 Data Analysis

The NEMO 3 reconstruction and simulation programs discussed in the data analysis are written in FORTRAN code. The front end analysis programs are written in C/C++ and ROOT.

7.1.1 Simulation Software

At the very basic level, the NEMO 3 simulation program (NEMOS) simulates particle tracks in the detector; however, it is extremely versatile. The geometry of the detector and the propagation of particles through matter are created with GEANT 3.2.1 [132], and the event generator is genBB [133], which contains all the kinematics of all the $\beta\beta$, β, γ and α decaying isotopes. NEMOS can therefore be used to simulate $0\nu\beta\beta$, $2\nu\beta\beta$ and Majoron emission events to the ground and excited states in all of the isotopes inside of the NEMO 3 detector. It can also be used to simulate all possible internal and external backgrounds associated with the experiment. NEMOS can also generate postscript files of event displays, which contain energy information, Geiger cell hits, and track curvature.

7.1.2 Reconstruction Software

The reconstruction program (NEMOR) uses information (such as calibration constants) from the NEMO 3 database to convert ADC and TDC signals to particle energies and times, and reconstructs particle tracks and, in the case of electrons and positrons, associates them with scintillators. Both the raw data and Monte Carlo (MC) files are run through the NEMOR program. There are two separate NEMOR executables used for the reconstruction process. *Nemor1e+* selects events with at least one electron track + anything else (this could be extra scintillator hits, or hits on the Geiger wires). The files that are produced using nemor1e+ can be analysed for any combination of particles. *Nemor1e* selects events that have only one reconstructed electron track associated with a scintillator hit. The files that are produced using nemor1e are used for the single electron (1e) channel analysis only and solely for background studies. The different stages of data analysis (from reconstruction to obtaining half-life results) are illustrated in a block diagram in Fig. 7.1.

7.1.3 Analysis Software

There are three stages of programs. In the first stage the preselection program 'slims' down the reconstructed ROOT files by applying preselection cuts mentioned in Sec. 7.4. The program also reconstructs the TOF hypotheses before applying the specific TOF cuts (see Sec. 7.4.1). This is also where topological cuts are made to select events from specific decay channels. These generic ROOT files contain events from all parts of the detector that have passed the preselection cuts.

In the next stage, the isotope analysis program selects events from specific parts of the detector. It contains more stringent energy cuts, kinematic cuts (angular distribution cuts) and α-particle rejection cuts. In the final stage the resultant ROOT files, which contain histograms rather than single events, are then analysed by several different programs which carry out background normalisation and subtraction, signal fitting, and obtain half-life results and plots such as the energy spectra.

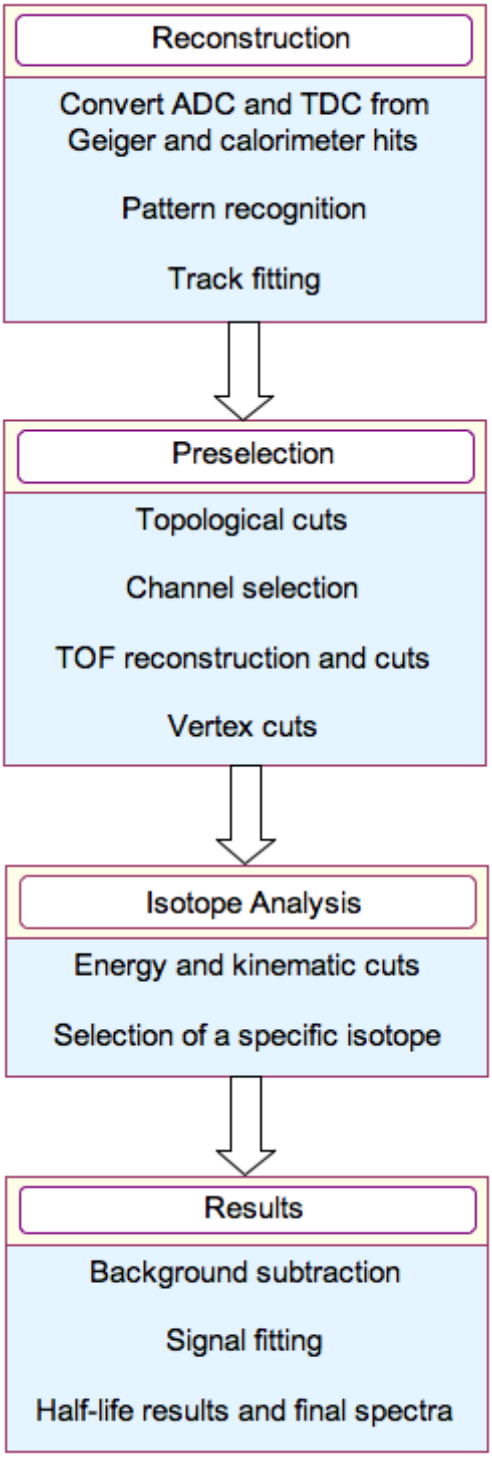

Figure 7.1: Block diagram explaining the different stages of data analysis, from event reconstruction to results stage.

7.2 NEMO 3 Phases

NEMO 3 data taking is divided into two phases. Phase 1 is known as the 'high radon phase' and ran from February 2003 to September 2004. Phase 2, known as the 'low-radon phase', started running after the installation of the radon trapping factory described in Sec. 5.5.1, and runs from October 2004 to December 2006. (Phase 2 is still in operation, but the data from 2007 onwards were not studied for the final analyses in this thesis.)

There are different NEMO 3 run statuses which are used to describe the quality of the recorded data. For instance run status 1 is used to label runs which are of a very good quality, whereas runs with run status 100000 have a high radon rate. For the ^{100}Mo excited states analysis only runs with run status 1 were selected and also for technical reasons, only phase 1 was studied. This gives the total experimental runtime of 7979 hrs (0.91 yrs).

For the ^{48}Ca analysis Phase 1 and Phase 2 were studied using a list of runs approved by the NEMO 3 analysis group, which included run statuses other than run status 1, for example runs where some PMT high voltage boards were switched off, and runs taken less than 24 hours after a calibration run. As discussed in Sec. 8.3 the radon background in the tracking gas is negligible, so the final $2\nu\beta\beta$ and $0\nu\beta\beta$ analyses use data from both phases without distinction, this gives the overall experimental runtime of 22638 hrs (2.58 yrs).

7.3 Particle Identification

7.3.1 Electrons and Positrons

An electron (positron) is defined as a track which originates from a source foil and travels through the wire chamber and is then associated with a fired scintillator. The track is reconstructed from fired Geiger cells and has a curvature consistent with that of an electron (positron).

7.3.2 Photons

Fired scintillators not associated with a track are selected as γ-scintillators. However, there are two possible scenarios where this might not be the case. The first scenario is where an electron back-scatters from one scintillator and is then detected by another. This type of event is identified through fired Geiger cells close to the fake γ-scintillator which are not associated with the electron track. The second scenario is where an electron hits the edge of one scintillator and fires the one adjacent to it. This type of event is identified through the proximity of the fake γ-scintillator to the scintillator associated with the electron track.

7.3.3 α-Particles

NEMO 3 is able to identify α-particles as short straight tracks. The suppression of Bi-Po type events described in Sec. 6.2, which are characterised by an emitted α-particle, are further discussed in Sec. 7.4.3.

7.4 Selection Criteria

The selection criteria section describes the preselection criteria for two electrons, one electron, photons and also the suppression of ^{214}Bi. With its powerful topological selection criteria NEMO 3 has very efficient particle identification capabilities. NEMO 3 can distinguish between electrons, positrons, α-particles and photons allowing a whole range of $\beta\beta$ decay modes and channels to be studied, and also allowing precise background measurements.

7.4.1 Two Electron and One Electron Event Preselection Criteria

In the two-electron (2e) channel, $\beta\beta$ type events are required to have two reconstructed tracks with a curvature consistent with a negatively charged particle, and be associated with an isolated calorimeter hit with energy > 200 keV. The tracks must have an event vertex reconstructed inside the source foil and go through the first two layers of the Geiger cells. The event vertex is the average position of the track vertices, and the track vertices are where the track intersects the source foil.

The transverse distance between the track vertices should be $\Delta XY < 2\,\text{cm}$, and the longitudinal distance $\Delta Z < 4\,\text{cm}$. These values are set by the resolution of the tracking chamber. The sum of the track lengths is also required to be $> 60\,\text{cm}$, which improves the TOF separation between the internal and external hypotheses discussed in the following paragraphs. Fig. 7.2 is a NEMO 3 event display of a $\beta\beta$ type event.

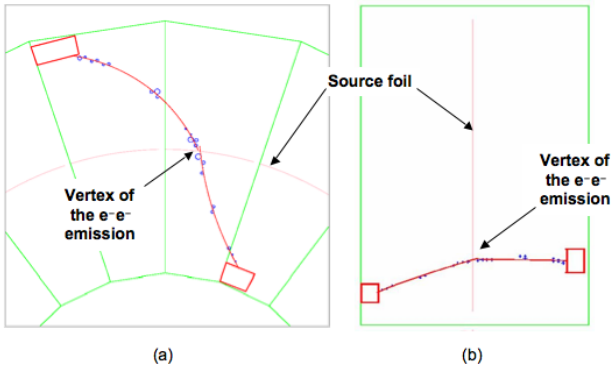

Figure 7.2: NEMO 3 event display of a $\beta\beta$ type event: two tracks with a curvature consistent with that of an electron, and associated with two isolated scintillator hits. (a) Transverse view (b) longitudinal view.

To establish whether the two electrons originate inside or outside of the source foil, the TOF of the electrons is compared with the time measured by a PMT associated to one of the electron tracks. The internal hypothesis assumes the electrons are generated at the same time inside the source foil, go through the Geiger chamber and are detected by different scintillators. The external hypothesis assumes that a particle enters the tracking volume via one of the scintillators, crosses through the source foil and is then detected by another scintillator. The TOF or χ^2 probability (discussed in the following subsections) that the event comes from inside the source foil is required to be $> 4\%$, and the TOF or χ^2 probability for an external crossing electron is required to be $< 1\%$. A χ^2 time of flight test is used to discriminate between the internal and external hypotheses. Both these scenarios are illustrated in Fig. 7.3.

The Internal Two Electron Hypothesis (χ^2_{int})

For the internal two electron hypothesis, the two tracks are characterised by their length, L_i $(i = 1, 2)$ the trigger time of its associated scintillator, t_i, and the energy deposited in the scintillator E_i. The time it takes for the particle to leave the foil and be detected by the scintillator (the particle's time of flight) is

$$\Delta t_i = \frac{L_i}{\beta_i c} \tag{7.1}$$

where c is the speed of light in a vacuum and β_i is

$$\beta_i = \frac{\sqrt{E_i(E_i + 2m_e c^2)}}{E_i + m_e c^2} \tag{7.2}$$

The time of the emission of each particle is therefore,

$$t_i^{int} = t_i - \Delta t_i = t_i - \frac{L_i}{\beta_i c}, \tag{7.3}$$

and the χ^2_{int} time of flight variable is written as

$$\chi^2_{int} = \frac{\left(\left(t_2 - \frac{L_2}{\beta_2 c}\right) - \left(t_1 - \frac{L_1}{\beta_1 c}\right)\right)^2}{\sigma^2_{tot}}, \tag{7.4}$$

where σ^2_{tot} is the sum of errors on the time $\sigma_{(t)}$, energy $\sigma_{(E)}$ and distance $\sigma_{(L)}$ and is given by

$$\sigma^2_{tot} = \sigma^2_{tot1} + \sigma^2_{tot2} = \sigma^2_{tot(t)} + \sigma^2_{tot(E)} + \sigma^2_{tot(L)} \tag{7.5}$$

which has the more explicit form,

$$\sigma^2_{tot} = \sum_{i=1}^{2} \sigma^2_{tot(t)i} + \sum_{i=1}^{2} \left(\frac{\Delta t_i^{int} (m_e c^2)^2}{E_i(E_i + m_e c^2)(E_i + 2m_e c^2)} \right)^2 \sigma^2_{Ei} + \sum_{i=1}^{2} \left(\frac{1}{\beta_i c} \right)^2 \sigma^2_{Li} \tag{7.6}$$

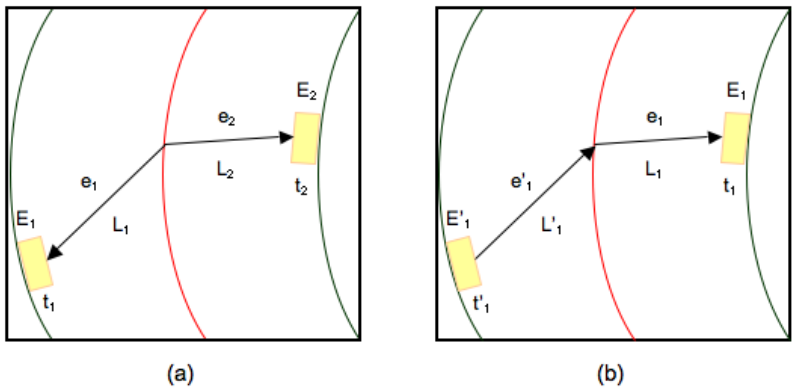

Figure 7.3: Diagram showing the two different TOF hypotheses: (a) The internal hypothesis where both the electrons are generated in the source foils and (b) the external hypothesis where an electron crosses the detector through the source foil.

The External Electron Crossing Hypothesis (χ^2_{cross})

The time of flight for a particle crossing the detector (illustrated in Fig. 7.3) is given by,

$$t^{cross} = \frac{L_1}{\beta_1 c} + \frac{L'_1}{\beta c}, \tag{7.7}$$

where β_1 and β have the same form as Eq. 7.2. β differs from β_1 as it takes into account the corrections to E_1 due to the energy loss of the particle after it has crossed though the foil and the gas inside the tracking chamber. The χ^2_{cross} time of flight variable is written as

$$\chi^2_{cross} = \frac{((t_1 - t'_1) - t^{cross})^2}{\sigma^2_{tot}}, \tag{7.8}$$

where σ^2_{tot} in this case is

$$\sigma^2_{tot} = \sum_{i=1'}^{1} \sigma^2_{tot(t)i} + \left(\frac{t^{cross}(m_e c^2)^2}{E_1(E_1 + m_e c^2)(E_1 + 2m_e c^2)}\right)^2 \sigma^2_{E_1} + \left(\frac{1}{\beta_1 c}\right)^2 (\sigma^2_{L'_1} + \sigma^2_{L_1}) \tag{7.9}$$

One Electron Events

One-electron events are required to have one reconstructed track with a curvature consistent with a negatively charged particle, and be associated with an isolated calorimeter hit with energy $> 200\,\text{keV}$. The track vertex must originate in the source foil and go through the first two layers of Geiger cells, and the track length is required to be $> 30\,\text{cm}$. In the case of the 1e channel used to estimate backgrounds, the threshold energy for the electron is > 500 keV, which eliminates a larger amount of unwanted low energy events to reduce file sizes.

7.4.2 Photons

Photons are selected (or rejected) by requiring a single unassociated scintillator hit with an energy $> 200\,\text{keV}$. The photon selection criteria can be used in conjunction with the single electron selection criteria to select events for the one-electron one-γ ($1e1\gamma$) channel which is useful to check the consistency of background activity measurements. In conjunction with the 2e selection criteria, channels such as the two-electron two-γ ($2e2\gamma$) channel can be studied (which is the channel studied for the $\beta\beta$ decay measurement of the 0_1^+ excited state half-life of ^{100}Mo). The TOF hypotheses for these $e\gamma$ channels are worked out in a similar way to the 2e TOF hypotheses. For the $1e1\gamma$ channel, the internal TOF probability is $> 1\%$ and the external probability assuming an incoming photon is $< 1\%$. For the $2e2\gamma$ channel, the internal TOF probability for the two photons is $> 1\%$ and the external probability is $< 1\%$.

7.4.3 Suppression of the ^{214}Bi Background

^{214}Bi is suppressed by removing Bi-Po type events, which are events accompanied by an α-particle (see Fig. 7.4 for an event display of a Bi-Po type event). These are discarded by looking for single Geiger cell hits with a delay $> 70\,\mu\text{s}$, or group hits (one or more hits within $2.6\,\mu\text{s}$ of each other and correlated in space) with a delay $> 20\,\mu\text{s}$. The required track length for electrons is also a way to discriminate between α-particles and electrons.

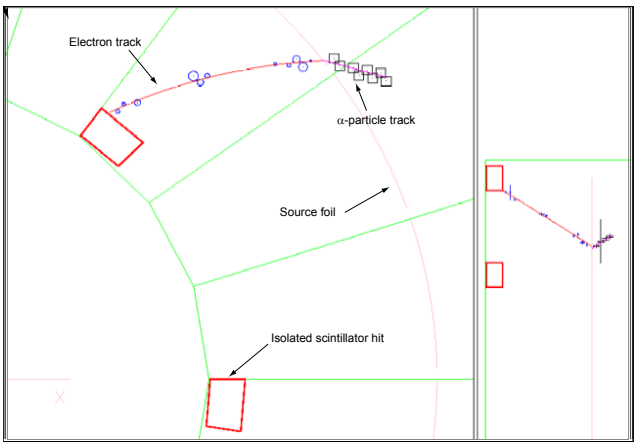

Figure 7.4: NEMO 3 event displays (transverse and longitudinal views) of a ^{214}Bi radon type event, showing one electron track, an α-particle track and an isolated scintillator hit from a photon.

7.5 External Background Model

The external background model used in this thesis is the work of V. Vasiliev, who produced several internal NEMO 3 notes outlining his approach to measuring the backgrounds and the results [134], [135].

The model was determined by studying the 1e1γ channel in various parts of the detector. For backgrounds such as radon, the choice of studying events with an electron + a delayed α-particle + anything else was not used as the main channel for this analysis because the exact location of the ^{214}Bi in the detector is unknown; it could be in the gas, near the Geiger wires or on the surface of the source foils, and this affects the α-particle detection efficiency. The statistics for the 1e1γ channel are lower than the α channel, however the latter is not sensitive to the systematics due to the uncertainty in the location of the α-particles. The α channel was used in this instance as a cross check for the 1e1γ channel, both methods were found to agree within 10-15% [135]. The model is also cross checked with the impurities found by the HPGe measurements of detector components such as the PMTs and iron frame. The activities for Phase 1 and Phase 2 are given in Tables 7.1 and 7.2 respectively.

Background Component	Activity (Bq)
^{228}Ac pmt	515
^{208}Tl pmt	67
^{214}Bi pmt	374
^{40}K pmt	954
Rn	702
^{60}Co iframe	50.7
^{214}Bi swire	$(598 \pm 6) \times 10^{-3}$
^{214}Pb swire	$(598 \pm 6) \times 10^{-3}$
^{208}Tl swire	2.8×10^{-3}
^{210}Bi swire	5.05 ± 1
^{214}Bi sfoil	$(19.5 \pm 3.5) \times 10^{-3}$
^{214}Pb sfoil	$(19.5 \pm 3.5) \times 10^{-3}$
^{210}Bi sfoil	$(17.4 \pm 5) \times 10^{-3}$

Table 7.1: Activities for the external background model for Phase 1. iframe is an abbreviation for the iron frames.

7.5.1 PMTs

Although extensive work was carried out to reduce the radioactivity of the NEMO 3 PMTs, the glass of the PMTs is still contaminated, which can be seen in Tables 5.1 and 5.2 (Sec. 5.3.2) which lists the activity in the PMTs for ^{40}K, ^{214}Bi and ^{208}Tl. As well as ^{208}Tl, ^{228}Ac is also a member of the ^{232}Th radioactive family. The chain between these two isotopes is in equilibrium and is related by the the ratio 36:100. Therefore ^{228}Ac is also added as a background component to give four PMT components in the model. The background activities were found by finding the relative contributions from each of these components by looking at the 1e1γ channel in the copper foil. The result from ^{228}Ac is out of equilibrium with ^{208}Tl, and the model also requires higher PMT activities than those in the HPGe measurements for all of the components, which suggests that other contributions exist at low energies that are not included in the model, but this does not affect the overall background

prediction from the model as a whole.

Radon in the Air Surrounding the Detector

As already discussed in Sec. 5.5.1 during Phase 1 the air surrounding the detector was contaminated with radon. This contamination is found inside the gap between the passive shielding and the detector. When the activities measured by NEMO 3 in Phase 2 are applied to Phase 1 there is a surplus of 1e1γ external events, this surplus of events is assumed come from the radon contamination. Using fixed measurements in the 1e1γ channel, the difference in the external background between both phases is used to find the radon activity for Phase 1.

7.5.2 ^{60}Co in the Iron Frame

The NEMO 3 iron frame was measured with HPGe detectors and found to be contaminated with ^{60}Co [126]. It can be detected with the 1e1γ channel as it β decays to the stable isotope ^{60}Ni and emits two photons during the process, each with an energy $\sim$1 MeV. This component of the background was also estimated from the 1e1γ channel in the copper foil.

7.5.3 Natural Radioactivity and Radon in the Tracking Gas

For the external background model there are two separate components to the radon and natural radioactivity found inside the detector tracking volume: activity on the surface of the Geiger wires (swire) and the surface of the source foils (sfoil). The contamination from ^{214}Bi and ^{214}Pb inside the detector is (most probably) due to ^{222}Rn daughters (such as ^{218}Po) which are positive ions >90% of the time. These positive ions migrate towards the effective negative charge of the wire chamber cathodes and the metallic foils, and are deposited there. The decays from radon daughters such as ^{214}Bi are then localised in these areas of the detector. This is seen as being the most likely scenario, although the mechanism is still not really understood.

It is possible to detect radon using the 1e1γ channel, as a large proportion of ^{214}Bi decay is accompanied by a high energy γ-ray with energy of 1.76 MeV. There

could be other 1e1γ contributions from Compton scattering from external γ-rays, but these events can be suppressed by selecting events with a γ-ray energy greater than 1 MeV. The activity from ^{214}Pb is set equal to that of ^{214}Bi assuming there is equilibrium in the thorium chain and that the Bi-Po-Pb ions are not mobile.

Background Component	**Activity (Bq)**
^{228}Ac pmt	515
^{208}Tl pmt	41.6
^{214}Bi pmt	374
^{40}K pmt	954
Rn	/
^{60}Co iframe	50.7
^{214}Bi swire	$(84 \pm 6) \times 10^{-3}$
^{214}Pb swire	$(84 \pm 6) \times 10^{-3}$
^{208}Tl swire	2.8×10^{-3}
^{210}Bi swire	5.05 ± 1
^{214}Bi sfoil	$(8.5 \pm 1.9) \times 10^{-3}$
^{214}Pb sfoil	$(8.5 \pm 1.9) \times 10^{-3}$
^{210}Bi sfoil	$(17.4 \pm 5) \times 10^{-3}$

Table 7.2: Activities for the external background model for Phase 2.

Natural Radioactivity on the Surface of the Geiger Wires

For the 1e1γ events coming from the surface of the Geiger wires the electron tracks are required to start from a particular Geiger layer. The ^{214}Bi activity was found from the gamma energy spectrum in the region between (1 - 4) MeV. In addition to the preselection criteria discussed in Sec. 7.4 the following cuts were also added. The track is required to have a Geiger cell hit in one of the four layers closest to the source foils. The internal TOF probability of the γ-ray has to be greater than 5%, and the sum of the energies of all other γ-rays has to be less than 150 keV. The cosine of the angle between the electron and gamma ($\cos\theta_{e\gamma}$) has to be less than

0.9, this is to suppress contributions from bremsstrahlung.

Contributions from ^{208}Tl and ^{210}Bi were also obtained. ^{208}Tl is also measured using the 1e1γ channel as the β decay of ^{208}Tl is accompanied by a γ-ray of $\sim$2.6 MeV from the first excited state decay of ^{208}Pb. ^{210}Bi is a β decay daughter of ^{210}Pb from the ^{238}U decay chain, and is measured using the 1e channel.

Natural Radioactivity on the Surface of the Source Foils

There are a number of 1e1γ events coming from the source foils, so extra cuts on the electron and gamma were introduced:

- $E_e > 0.3$ MeV
- 1.1 MeV $< E_\gamma <$ 2.8 MeV
- $\cos\theta_{e\gamma}$ <-0.2

Tracks starting from the first Geiger cell layer were selected and the swire activities were fixed. This measurement does not distinguish between those events coming from the surface of the source foil and those from inside the source foil, so activities differ for each isotope. The background component from ^{210}Bi was also measured.

7.5.4 2e Analysis in the Copper Foil

As discussed in Sec. 7.5.1 some of the activities in the external background model are not in agreement with the activities from HPGe measurements, and some isotopes in the model (such as ^{228}Ac and ^{208}Tl in the PMTs) are not in equilibrium, this is because the model is an effective background model which is used to describe the 2e channel correctly. The 2e channel in the copper foil is therefore used to cross check the model. 2e events in the copper foil are are selected using the 2e preselection criteria in Sec. 7.4.1. All the external background MC components are included, plus the internal copper backgrounds given in Table 7.3 which were measured using the 1e channel in the copper foil. Plots of 2e events in the copper foil for Phase 1 and Phase 2 are shown in Figs. 7.5 and 7.6, which show that the external background model is a good fit to the data. A total list of backgrounds and their contributions for Phase 1 and Phase 2 are in Tables 7.4 and 7.5.

Component	Activity (Bq)
^{228}Ac	9×10^{-5}
^{212}Bi	6×10^{-5}
^{234m}Pa	1.22×10^{-3}
^{208}Tl	3×10^{-5}

Table 7.3: Internal activities for the copper foil measured by NEMO 3 using the 1e channel. The activities are the same for Phase 1 and Phase 2.

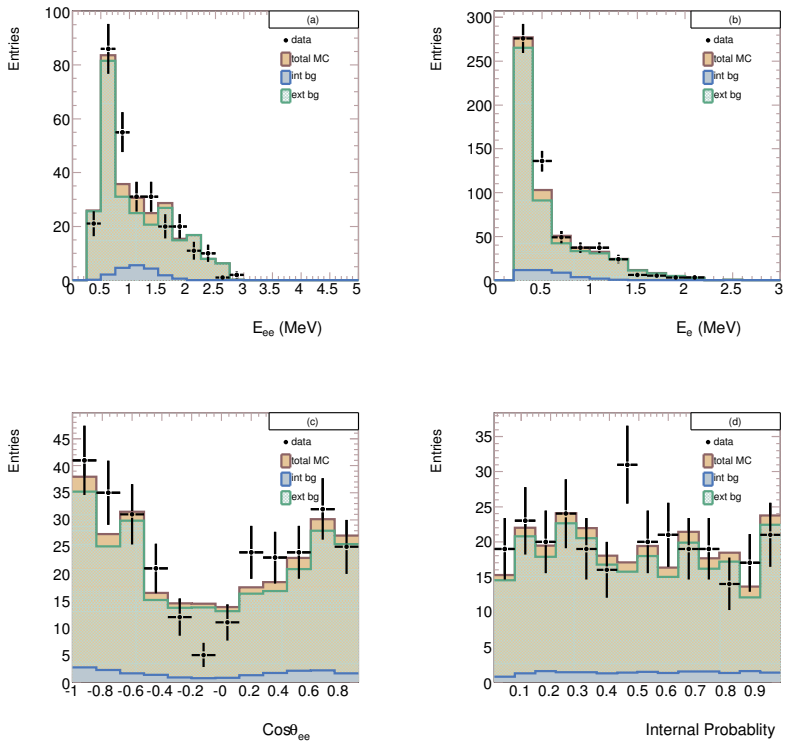

Figure 7.5: 2e events in the copper foil (Phase 1). (a) Electron sum energy spectrum. (b) Single electron spectrum. (c) Cosine of the angle between two electrons. (d) Internal χ^2 probability.

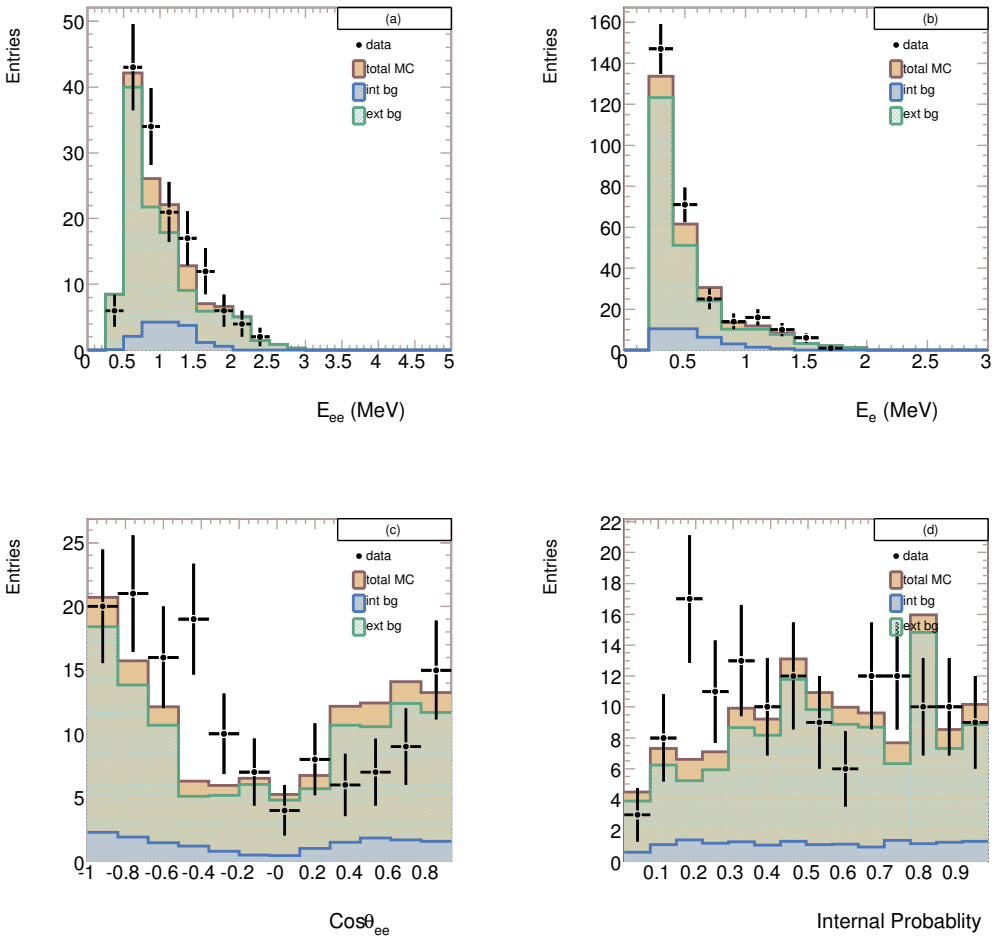

Figure 7.6: 2e events in the copper foil (Phase 2). (a) Electron sum energy spectrum. (b) Single electron spectrum. (c) Cosine of the angle between two electrons. (d) Internal χ^2 probability.

Component	**Efficiency**	**Expt. Events**
^{210}Bi sfoil	1.66×10^{-7}	0.10 ± 0.05
^{214}Bi sfoil	3.34×10^{-5}	22.70 ± 1.23
^{214}Pb sfoil	2.03×10^{-5}	13.80 ± 0.52
^{210}Bi swire	6.43×10^{-8}	11.30 ± 3.02
^{214}Bi swire	3.68×10^{-6}	76.57 ± 6.96
^{214}Pb swire	3.50×10^{-6}	72.91 ± 4.55
^{208}Tl swire	2.93×10^{-6}	0.29 ± 0.05
^{214}Bi air	8.86×10^{-10}	21.65 ± 4.51
^{228}Ac pmt	8.41×10^{-11}	1.51 ± 1.51
^{214}Bi pmt	1.02×10^{-9}	13.29 ± 2.83
^{40}K pmt	1.89×10^{-10}	6.26 ± 1.44
^{208}Tl pmt	5.80×10^{-9}	13.52 ± 2.06
^{60}Co iframe	1.53×10^{-9}	2.70 ± 1.35
^{228}Ac intBgr	5.65×10^{-5}	0.18 ± 0.02
^{212}Bi intBgr	5.22×10^{-5}	0.11 ± 0.01
^{234m}Pa intBgr	4.44×10^{-4}	18.90 ± 0.66
^{208}Tl intBgr	1.44×10^{-4}	0.15 ± 0.01
MC Total		275.93 ± 10.92
Data		**288**

Table 7.4: 2e events in the copper foil (Phase 1).

Component	**Efficiency**	**Expt. Events**
^{210}Bi sfoil	3.40×10^{-7}	0.28 ± 0.08
^{214}Bi sfoil	3.40×10^{-5}	13.48 ± 0.62
^{214}Pb sfoil	1.95×10^{-5}	7.73 ± 0.26
^{210}Bi swire	7.53×10^{-8}	17.76 ± 3.79
^{214}Bi swire	3.29×10^{-6}	12.89 ± 1.07
^{214}Pb swire	3.80×10^{-6}	14.90 ± 0.77
^{208}Tl swire	2.66×10^{-6}	0.35 ± 0.05
^{228}Ac pmt	4.39×10^{-10}	10.55 ± 3.99
^{214}Bi pmt	9.69×10^{-10}	16.91 ± 3.20
^{40}K pmt	1.11×10^{-10}	4.95 ± 1.28
^{208}Tl pmt	4.83×10^{-9}	9.37 ± 1.35
^{60}Co iframe	3.13×10^{-9}	7.41 ± 2.24
^{228}Ac intBgr	5.42×10^{-5}	0.18 ± 0.02
^{212}Bi intBgr	4.81×10^{-5}	0.10 ± 0.10
^{234m}Pa intBgr	3.68×10^{-4}	16.09 ± 0.60
^{208}Tl intBgr	1.00×10^{-4}	0.12 ± 0.01
MC Total		133.05 ± 7.17
Data		**145**

Table 7.5: 2e events in the copper foil (Phase 2).

7.6 Half-Life Results

After all events are selected and the signal and background has been identified, the results can then be interpreted. To calculate the half-life we start by looking at the following well known equation,

$$N = N_0 e^{-\lambda t}, \tag{7.10}$$

where N is the number of remaining nuclei, N_0 is the number of nuclei at the beginning of the experiment, $\lambda = \frac{ln2}{T_{1/2}}$ and t is the run time of the experiment. The number of decayed nuclei N_{dec} is therefore,

$$N_{dec} = N_0 - N \tag{7.11}$$

which gives

$$N_{dec} = N_0(1 - e^{-\lambda t}). \tag{7.12}$$

Because we know the half-lives of the isotopes we are studying are long, we can Taylor expand the exponential in Eq. 7.12 to give

$$N_{dec} = N_0 t \frac{ln(2)}{T_{1/2}}. \tag{7.13}$$

We can calculate N_0 from the mass m_i and atomic weight A_r of the isotope being studied and Avagadros number N_A, and so from knowing the number of decays that have taken place during the time t, we can calculate the half-life:

$$T_{1/2} = \frac{m_i N_A}{A_r N_{dec}} ln(2) t. \tag{7.14}$$

As we are dealing with an experimental situation, i.e. we are not assuming perfect conditions, the detector efficiency ε should be taken into account, and so Eq. 7.14 becomes

$$T_{1/2} = \varepsilon \frac{m_i N_A}{A_r N_{dec}} ln(2) t. \tag{7.15}$$

For $2\nu\beta\beta$ analysis we select two electron events, and from this obtain the energy spectrum and other interesting information such as the angular distribution. The signal is found by subtracting the background from the data; the shape of the $2\nu\beta\beta$ decay is then fitted to the signal, which returns a normalisation of the data events. This gives us the value for N_{dec} which is entered into Eq. 7.15 giving the final half-life result.

Chapter 8

Double Beta Decay of ^{48}Ca

8.1 Introduction

The study of $2\nu\beta\beta$ decay has been used extensively in nuclear physics to probe theories of the nuclear structure of double beta decay isotopes, and ^{48}Ca offers a unique opportunity for this study. It is the lightest known double beta decay candidate, and can be treated with nuclear shell model calculations, thus giving an insight into complicated nuclear matrix element calculations, which are needed for the $0\nu\beta\beta$ decay search. It has the largest energy release, $Q_{\beta\beta} = 4.27$ MeV, giving a natural suppression of external backgrounds from Radon and Thoron. All of these properties make it an excellent candidate for the $0\nu\beta\beta$ decay search, although it has a low natural abundance of 0.187%.

The decay scheme for ^{48}Ca is shown in Fig.8.1. The $\beta\beta$ decay to the ground state of ^{48}Ti is accompanied by the simultaneous emission of two electrons.

8.2 Previous Experiments

8.2.1 Mateosian and Goldhaber Experiment

The Mateosian and Goldhaber experiment of 1966 was proposed primarily for the study of lepton number conservation and the nature of the neutrino [136]. The experiment used CaF_2 scintillating crystals enriched to 96.59% and which contained 11.4g of ^{48}Ca.

Unusually it was housed in a section of a naval gun with 14-in thick walls. After 28.7 days of data taking the results were, $T_{1/2}^{(2\nu)} > 5\times10^{18}$ yrs and $T_{1/2}^{(0\nu)} > 2\times10^{20}$ yrs

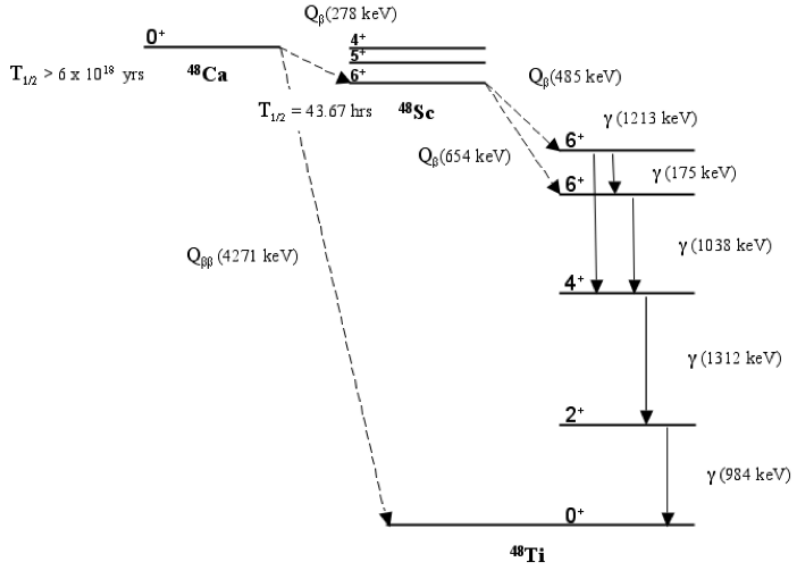

Figure 8.1: ^{48}Ca decay Scheme. The β decay to ^{48}Sc is highly-forbidden.

8.2.2 The Beijing Experiment

The Beijing $0\nu\beta\beta$ decay experiment was located in a coal mine just outside of Beijing [137] underneath 512 m of rock, the equivalent of about 1300 m of water. Unactivated CaF_2 crystals were used for this experiment, which were found to have a better energy resolution than the enriched CaF_2 crystals used in 1966 by Mateosian and Goldhaber [136]. After 7588.5 hrs (0.87 yrs) of data taking the published results were$T_{1/2}^{(0\nu)} > 9.5 \times 10^{21}$ yrs (at 78% C.L.).

Although the total experiment time was 7588.5 hrs, it was split into two periods. For the first period (1700 hrs) two CaF_2 crystals were used and for the second period another two were added, giving a total of four crystals. Each crystal was 12 cm long, 17.8 cm wide, with a conical part 3.8 cm long, 10 cm wide, and differed in weight, the heaviest being 10140.1 g and the lightest 8828.6 g. Altogether, the crystals contained 43 g of ^{48}Ca. The crystals were sealed in an atmosphere of pure argon and enclosed in an oxygen-free copper can. Purified MgO powder was used as a reflective layer

between the crystals and the can. Each crystal was coupled to a PMT, XP-2041Q, which were made with a quartz window. These were used to collect UV light, thus avoiding the natural radioactivity found in glass. For an anti-coincidence veto they used plastic scintillator, NE110, which surrounded the crystals. For the hard shielding, steel plates, 2 cm thick were used, which were enclosed by lead bricks, 8-10 cm thick.

8.2.3 Balysh Experiment

The Balysh [138] Experiment was a TPC experiment based in a tunnel in the Hoover Dam. The result of the experiment: $T^{(2\nu)} = (4.3^{+2.4}_{-1.1}(stat.) \pm 1.4(syst.)) \times 10^{19}$ yrs was obtained with 42.2 g of finely powdered $CaCO_3$ enriched to 76% in ^{48}Ca. This was the first experiment to obtain a positive result $2\nu\beta\beta$ decay of ^{48}Ca, giving the first evidence that experimental results are consistent with shell model calculations.

Two different methods of background estimation were used. Method A was a direct method using MC in the 2e channel, and Method B used information from the 1e channel to eliminate events with poor energy resolution. Method A was used to obtain the final published results, and the difference between the results from Method A and B was included in the systematic error.

8.2.4 TGV Experiment

The TGV (Telescope Germanium Vertical) experiment [139] is based in Modane in France, and is a collaboration between French and Russian institutions. The beta decay of ^{48}Ca was studied with a low background HPGe multi-detector spectrometer. The suppression of backgrounds was achieved with a mixture of shielding (copper against radon, and polyethylene filled with boron against neutrons) and analysis techniques. They were able to distinguish between betas and gammas using the detector pulse rise time, and also only selected events with double coincidences from neighbouring HPGe detectors. Each source was made up of a mixture of 80% $CaCO_3$ and 20% polyvinyl formal placed on a mylar support. Eight of the sources contained ^{48}Ca enriched to 78% and another eight contained natural Ca. The total weight of

the sources was 3.5 g, of which only 1g was ^{48}Ca. After 8700 hrs of data taking their results were as follows: $T^{(2\nu)} = (4.2 + 3.3 - 1.3) \times 10^{19}$ yrs, $T^{(0\nu)} > 1.5 \times 10^{21}$ yrs (at 90% C.L.).

8.2.5 ELEGANT VI

ELEGANT VI was operating in the Oto Cosmo Observatory, Nara, Japan [104]. It was a CaF_2 active source scintillator experiment, using 23 CaF_2 crystals, weighing 6.66 kg, the equivalent of $\sim 9.61 \times 10^{22}$ ^{48}Ca atoms. The detector had several different types of passive shield: two shields (copper and lead) to reduce γ-rays, and three different shields to suppress the neutron background. The 23 CaF_2 active scintillator detectors were arranged in a modular design, with the CsI(Tl) scintillators acting as veto counters. To reduce the radon background, the scintillators were sealed in an air tight box which had been purged with pure N_2 gas. The energy interval for the $0\nu\beta\beta$ decay was (4.18 - 4.38) MeV and after 5567 hrs of data taking, the results were:

$$T_{1/2}^{(0\nu)} > 1.4 \times 10^{22} \text{ yrs (at 90\% C.L.)}$$

with an experimental sensitivity of

$$T_{1/2}^{(0\nu)} > 5.9 \times 10^{21} \text{ yrs (at 90\% C.L.)},$$

which corresonds to the neutrino mass constraint $m_\nu < (7.2 - 44.7)$ eV.

8.2.6 CANDLES

CANDLES is an experiment being developed by the ELEGANT VI collaboration [118]. The aim is to reach a sensitivity to a half-life of 10^{26} yrs for the $0\nu\beta\beta$ decay of ^{48}Ca, corresponding to a neutrino mass of $\sim$30 meV.

The detector will consist of undoped 10 cm^3 CaF_2 scintillators, immersed in liquid scintillator, and surrounded by large PMTs. The light emitted from the CaF_2 crystals is in the UV , and so the liquid scintillator not only acts as a wavelength shifter, converting the UV light to visible light, but also as an active shield.

8.3 Background Model and Measurement

In order to estimate the background for this ^{48}Ca analysis, two methods were used: HPGe measurements and measurements made by NEMO 3 using controlled channels, such as the 1e and 1e1γ channels, which are discussed in Sec. 7.5. A list of the internal backgrounds and their activities is given in Table 8.1.

Background	**Activity (Bq)**
^{228}Ac	1.46×10^{-5}
^{212}Bi	1.46×10^{-5}
^{214}Bi	4.45×10^{-6}
^{137}Cs*	4.95×10^{-5}
^{152}Eu*	5.25×10^{-4}
^{40}K	8.00×10^{-4}
^{214}Pb	4.60×10^{-6}
^{208}Tl	5.25×10^{-6}
^{90}Y	0.03

Table 8.1: Internal background activities in the ^{48}Ca source foils. The starred activities are HPGe measurements, all other activities were found by the NEMO 3 detector. The ^{90}Y activity is discussed in Sec. 8.3.1.

The sample of ^{48}Ca inside NEMO 3 is known to be contaminated with ^{90}Sr, which may have happened during the production process. ^{90}Sr has a low Q_β value (0.546 MeV) and a half-life of 28.79 yrs and so is not a major background for the ^{48}Ca analysis, however its daughter, ^{90}Y, has a Q_β value of 2.282 MeV and a half-life of 64 hrs, making it a difficult background source. Both ^{90}Sr and ^{90}Y decay by emitting a single electron, and imitate $\beta\beta$ events through Möller scattering. This is illustrated in Fig.8.8 where the majority of the internal background is from ^{90}Y, and the plot of the two electron angular distribution ($\cos\theta_{ee}$) shows that most of these events have small angles due to the low energies of the electrons involved in the Möller scattering process.

There are other β^- emitters with high Q_β values such as ^{208}Tl and ^{214}Bi but

their contributions to the internal backgrounds, as well as the contributions from external backgrounds, are insignificant compared to the ^{90}Sr contamination. This is shown in the 1e background measurement which is described in Sec. 8.3.1 where we can see that ^{90}Y is the main background from the fit of ^{90}Y and ^{214}Bi in Fig. 8.3.

A break-down of expected background events for the preselection cuts (see Sec. 7.4.1) is given in Table 8.2 showing the total of all other backgrounds to be 2.3% of the total ^{90}Y contribution. The background MC (including some components not listed here) are run through the selection programs (preselection and final selection) and are then normalised to the activities obtained through the HPGe measurements and measurements from the 1e and 1e1γ channels. Table 8.3 gives the expected background events for the final selection cuts, which are discussed in Sec. 8.4.4. Because of this ^{90}Y background dominance, and the absence of a radon contribution in the final selection of background events, for this analysis Phase 1 and Phase 2 are studied together without distinction.

Background	**Generated Events**	**Efficiency**	**Expected Events**
^{214}Bi sfoil	$2.80e^{+07}$	$3.28e^{-07}$	0.37 ± 0.13
^{214}Pb sfoil	$9.46e^{+07}$	$7.77e^{-07}$	0.89 ± 0.11
^{210}Bi swire	$1.11e^{+09}$	$1.04e^{-09}$	0.43 ± 0.43
^{214}Bi swire	$1.13e^{+08}$	$7.15e^{-08}$	1.99 ± 0.75
^{214}Pb swire	$5.48e^{+08}$	$8.60e^{-08}$	2.39 ± 0.37
^{208}Tl pmt	$2.00e^{+10}$	$1.15e^{-10}$	0.51 ± 0.36
^{60}Co iframe	$7.05e^{+09}$	$1.63e^{-10}$	0.67 ± 0.67
^{228}Ac intbgr	$1.00e^{+07}$	$9.33e^{-05}$	0.111 ± 0.004
^{214}Bi intbgr	$2.00e^{+07}$	$3.62e^{-04}$	0.131 ± 0.002
^{152}Eu intbgr	$3.00e^{+06}$	$3.83e^{-06}$	0.16 ± 0.05
^{208}Tl intbgr	$1.00e^{+07}$	$2.34e^{-04}$	0.1010.002
^{90}Y intbgr	$1.00e^{+08}$	$1.39e^{-04}$	341.38 ± 3.10

Table 8.2: Background components which give more than 0.1 2e events after preselection cuts in ^{48}Ca, compared to 743 data events.

Background	Generated Events	Efficiency	Expected Events
^{214}Bi sfoil	$2.80e^{+07}$	$2.87e^{-07}$	0.33 ± 0.12
^{214}Bi swire	$1.13e^{+08}$	$2.04e^{-08}$	0.57 ± 0.40
^{90}Y intbgr	$1.00e^{+08}$	$6.60e^{-06}$	16.13 ± 0.67

Table 8.3: Background components which give more than 0.1 2e events after final selection cuts in ^{48}Ca, compared to 133 data events

8.3.1 ^{90}Y (^{90}Sr) Activity Measurement (1e channel)

The ^{90}Y activity was calculated by selecting 1e events using the 1e preselection criteria given in Sec. 7.4.1. A first look at the spectrum Fig. 8.2 reveals that there is some undescribed background in the low and high energy regions.

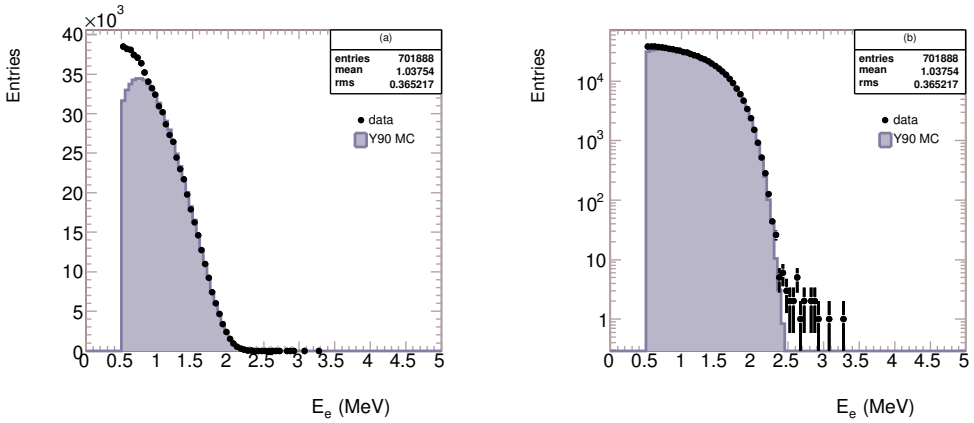

Figure 8.2: Plots of the ^{90}Y 1e spectrum showing the discrepancy between data and expected background at (a) low (linear scale) and (b) high energies (log scale).

In the high energy region, this discrepancy can be resolved by adding in components from ^{214}Bi on the surface of the source foil (sfoil) and on the surface of the Geiger wires (swire), which are normalised with the activities given in Sec. 7.5. Fig. 8.3 shows the 1e spectrum with these components added. In the low energy region, this background (or group of backgrounds) has a Q_β value in the region of 1 MeV, see Fig. 8.4 for the corresponding residual plot.

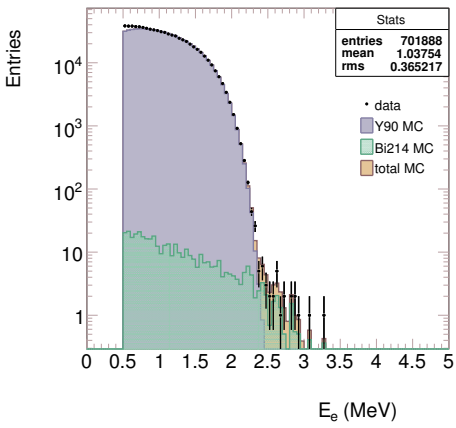

Figure 8.3: Plot of the ^{90}Y 1e spectrum with ^{214}Bi sfoil and swire.

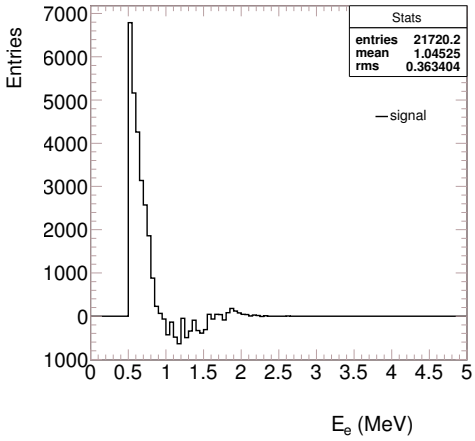

Figure 8.4: The ^{90}Y 1e residual spectrum.

To try and solve this low energy background problem, four different backgrounds were considered : ^{210}Bi (sfoil), ^{40}K (internal), ^{234m}Pa (internal), and ^{90}Y (internal). The TFractionFitter function in ROOT [140] was used to perform the fit, and the five backgrounds listed above were floated in different configurations. The two fixed backgrounds were ^{214}Bi (sfoil and swire). Fits for ^{90}Y and each of the three main floating backgrounds are shown in Figs. 8.5 and 8.6, and activities for these combinations are also listed in Table 8.4. The first entry of Table 8.4 gives the activities

found when the four main backgrounds are floated together, and Fig. 8.5 shows a plot of this fit. The low energy plot of this fit is shown in Fig. 8.7. The plots for the last two entries of Table 8.4 are shown in Fig. 8.6. It should also be noted from Table 8.4 that the ^{90}Y activity results are stable for each configuration, apart from the final result in Table 8.4 which has a large chi square.

Backgrounds	^{90}**Y**	^{210}**Bi**	^{40}**K**	^{234m}**Pa**	χ^2**/d.o.f.**
Y Bi K Pa	0.03	4.12 ± 0.13	1.08×10^{-8}	1.49×10^{-9}	98/94
Y Bi	0.03	4.13 ± 0.11	/	/	68/96
Y K	0.030	/	0.005	/	162/96
Y Pa	0.024	/	/	0.010	1121/96

Table 8.4: Activity results for different configurations of floating backgrounds using ^{90}Y, ^{210}Bi, ^{40}K, and ^{234m}Pa . All activities are given in Bq. For some of the results the errors calculated by the ROOT function are negligible.

This type of low energy background is difficult for the NEMO 3 dectector to resolve due to the energy resolution of the calorimeter; in fact a good description of the very low energy background below 0.5 MeV is a challenging task. The activity measured for ^{210}Bi (sfoil) may therefore be an exagerated result, as the activity gives a higher contribution than that of ^{214}Bi, but ^{210}Bi could be out of equilibrium as it is the daughter of the relatively long lived isotope ^{210}Pb.

Because of the ambiguity of these activity measurements, the activity for ^{90}Y was measured using a cut of 1 Mev on the 1e energy. After 22421 hrs of data taking, 701888 events were selected, and the activity for ^{90}Y in the ^{48}Ca foil is found to be

$$A(^{90}Y) = 1695 \pm 2(stat.)\text{mBq/kg}$$

The systematic error on this measurement will be discussed in Sec. 8.5 and the final result with the systematic error is given in Sec. 8.6.

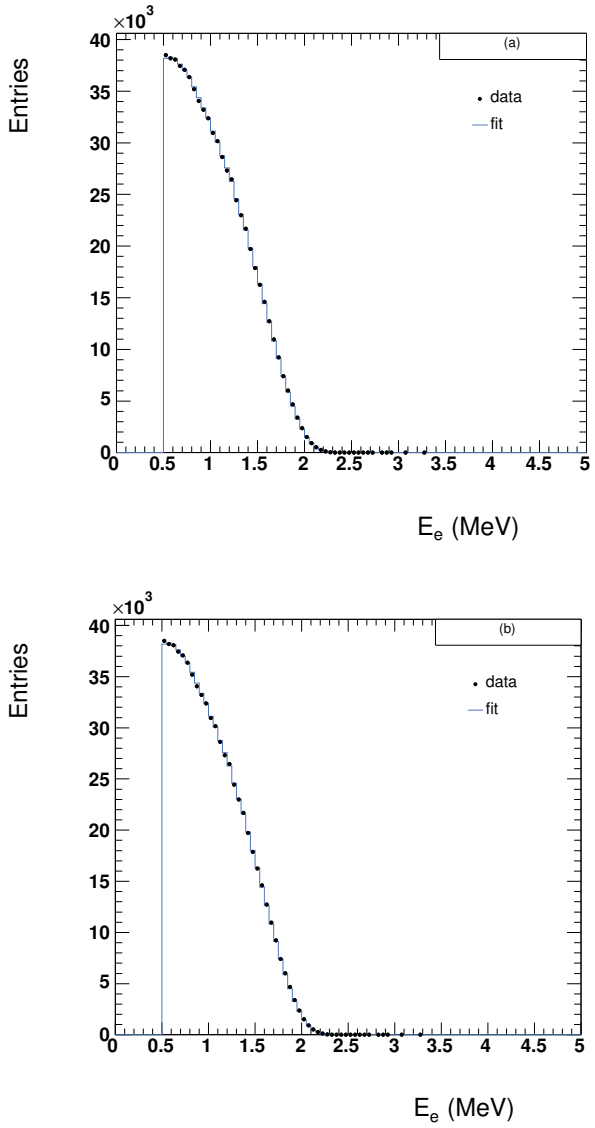

Figure 8.5: Plots of the ^{90}Y 1e spectrum fits with different configurations of backgrounds. The floating backgrounds for each plot are: (a) ^{90}Y, ^{210}Bi, ^{40}K and ^{234m}Pa (b) ^{90}Y and ^{210}Bi.

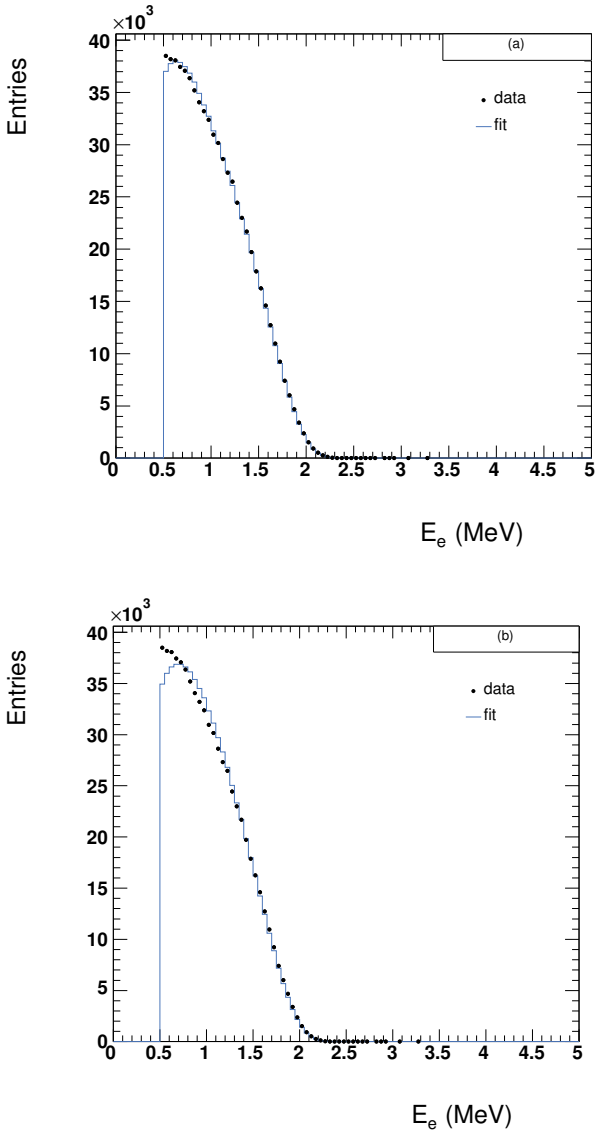

Figure 8.6: Plots of the ^{90}Y 1e spectrum fits with different configurations of backgrounds. The floating backgrounds for each plot are: (a) ^{90}Y and ^{40}K (b) ^{90}Y and ^{234m}Pa.

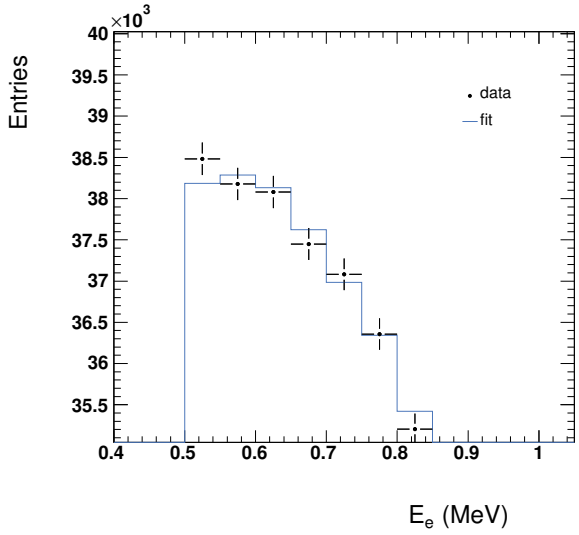

Figure 8.7: Plot of the ^{90}Y 1e spectrum fit with ^{90}Y, ^{210}Bi, ^{40}K and ^{234m}Pa highlighting the discrepancy between data and MC at low energy.

8.4 $2\nu\beta\beta$ Decay of ^{48}Ca Analysis

8.4.1 Preselection Analysis in the 2e Channel

The low energy background problem is not just confined to the 1e channel. The 2e preselection spectra in Fig. 8.8 reveal a discrepancy between the data and MC at low energies, and specifically for the electron sum spectrum, between 0.5 and 1 MeV. As already mentioned in Sec. 8.3, the plot of $\cos\theta_{ee}$ in Fig.8.8 also shows the prevalence of the ^{90}Y $\beta\beta$ type events from Möller scattering as the majority of these events have small angles. For this reason we can see how selecting events with a $\cos\theta_{ee} < 0$ cuts out these ^{90}Y events.

Although, as shown in Fig. 8.9, the situation with the low energy background problem is further exacerbated with this cut, as the deficit between data and MC is more obvious. These plots indicate we are looking for a background (or group of backgrounds) with large angles between the two electrons. This low energy background discrepancy is specific to ^{48}Ca and probably from an internal source, consequently the 1e and 1e1γ channels were studied to try to understand this background.

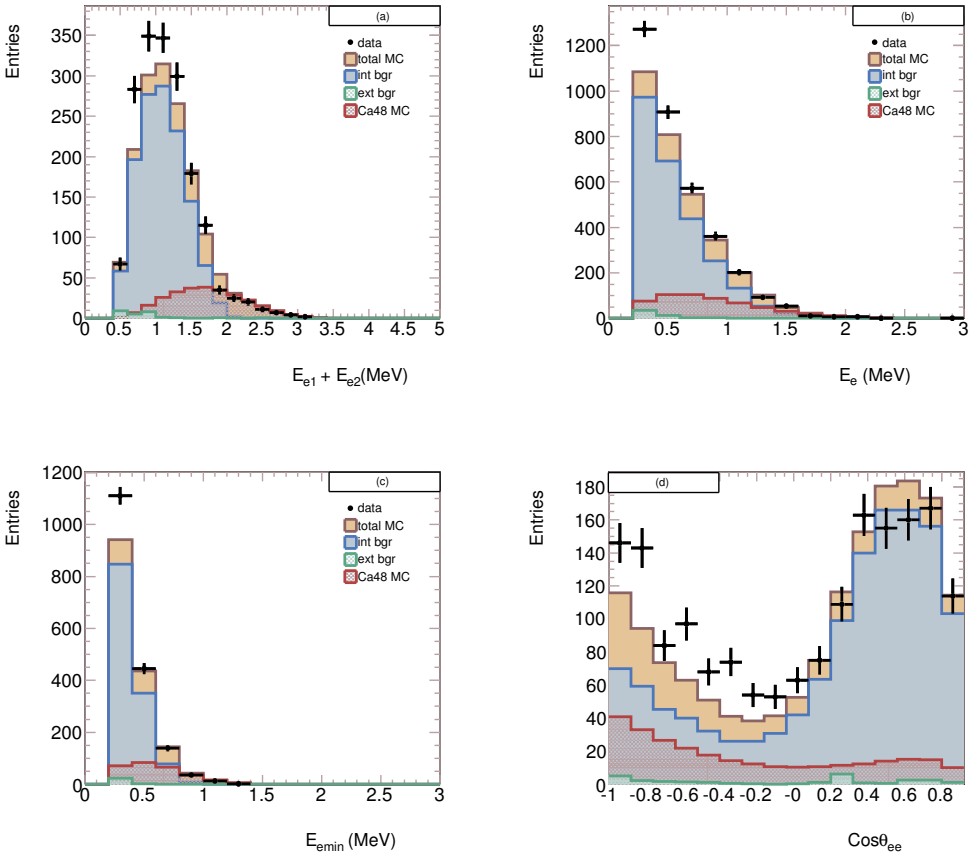

Figure 8.8: 2e preselection plots (all $\cos\theta_{ee}$): (a) Electron sum spectrum (1743 data events) (b) Single electron spectrum, (c) Minimum electron energy spectrum (d) Cosine of the angle between two electrons. The prevalence of the ^{90}Y background is clearly shown in (d) where the Möller scattering of the β particles from ^{90}Y results in $\beta\beta$ type events with small angles. Because of the deficit between the data and MC in these plots, the ^{48}Ca MC is normalised to the activity calculated with the final measured half-life for ^{48}Ca.

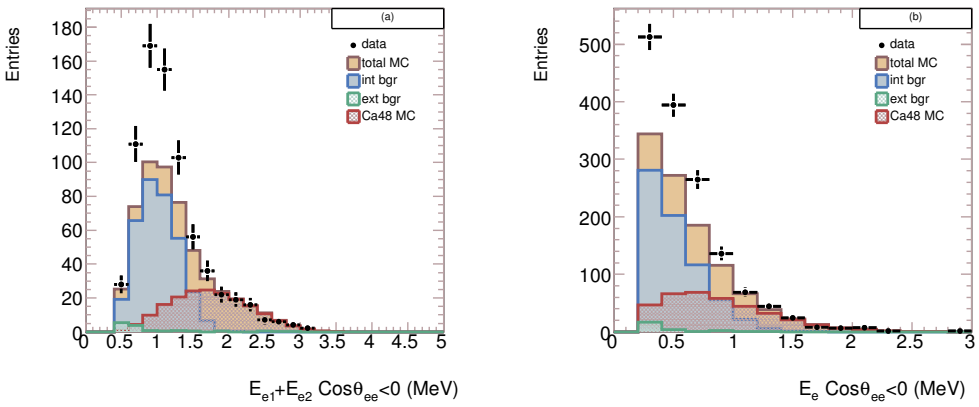

Figure 8.9: 2e preselection plots ($\cos\theta_{ee} < 0$): (a) Electron sum spectrum (743 data events) (b) Single electron spectrum. These plots highlight the existence of an unknown background in the low energy region of the electron sum and single electron spectra. Because of the deficit between the data and MC in these plots, the ^{48}Ca MC is normalised to the activity calculated with the final measured half-life for ^{48}Ca.

8.4.2 Another Look at the 1e Channel

If the contamination of the ^{48}Ca discs is from an internal source, it may be possible to pinpoint an area of the discs where the contamination originates from. The plot of the Z vertex vs sector in Fig. 8.10 reveals an area of contamination on the right-hand side of the ^{48}Ca discs. This is the calibration tube adjacent to the ^{48}Ca and ^{96}Zr foils. Clearly there is some residual contamination around the areas of the tube where the calibration sources are introduced. It is possible (although unlikely) these areas of the tube are contaminating the ^{48}Ca discs.

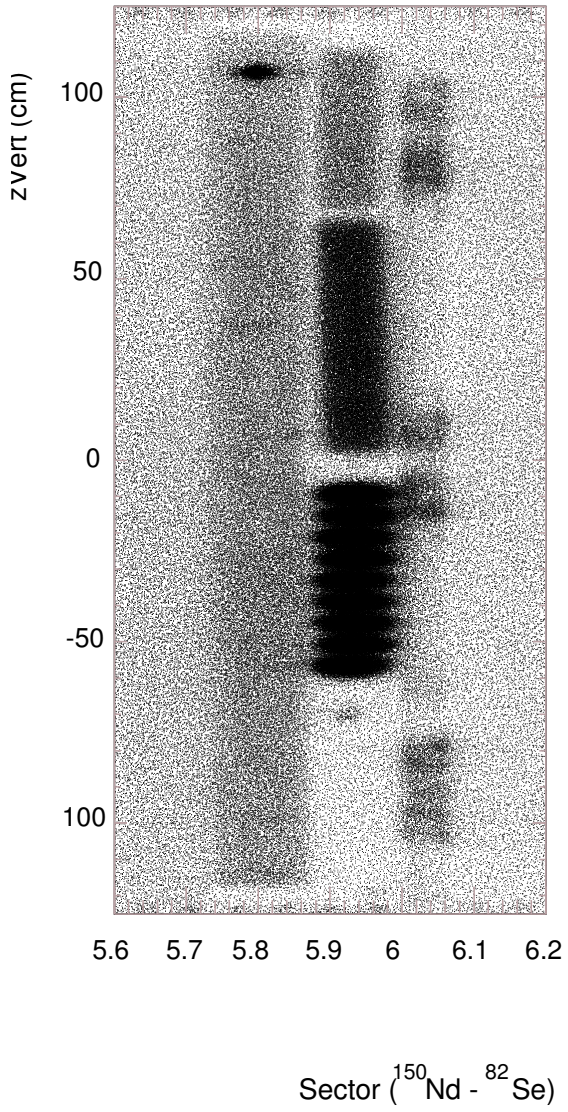

Figure 8.10: Plot of Z vertex vs sector using the 1e channel of sector 5 in the detector. The first dark strip on the left is the ^{150}Nd foil, next to this are the two ^{96}Zr foil strips and directly underneath these, the ^{48}Ca discs. The calibration tube is clearly visible adjacent to the ^{96}Zr foil strips and ^{48}Ca discs.

The two background subtracted plots of the Z vertex vs sector, Fig. 8.11, and sector vs E_e, Fig. 8.12 show spurious 'hotspot' areas on the left-hand side of the discs. These areas of activity are due to a difference in the description of the positions of the ^{48}Ca discs inside the detector between the data and MC, which can also be seen in Fig. 8.13. This misalignment between data and MC is a source of systematic error and is addressed in Sec. 8.5.

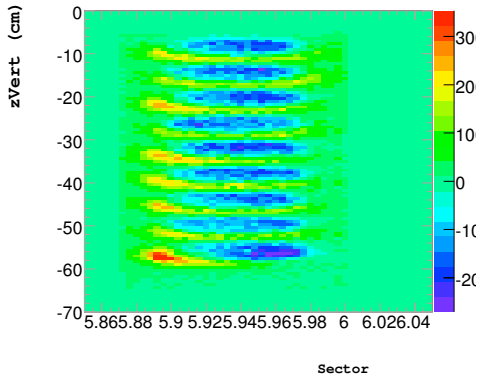

Figure 8.11: 2D plot of Z vertex vs detector sector 1e channel.

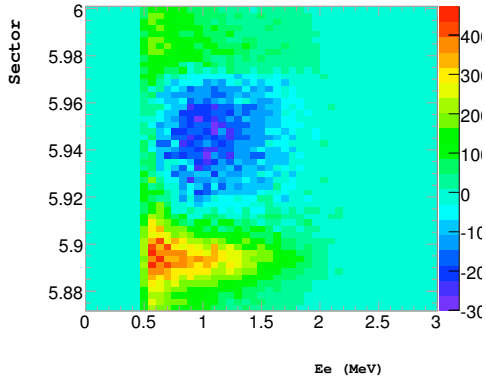

Figure 8.12: 2D plot of detector sector vs electron energy 1e channel.

Fig. 8.11 shows that in the 1e channel the ^{90}Y background completely dominates and masks any potential hotspot areas, thus it is not possible to isolate any specific area of contamination using this channel.

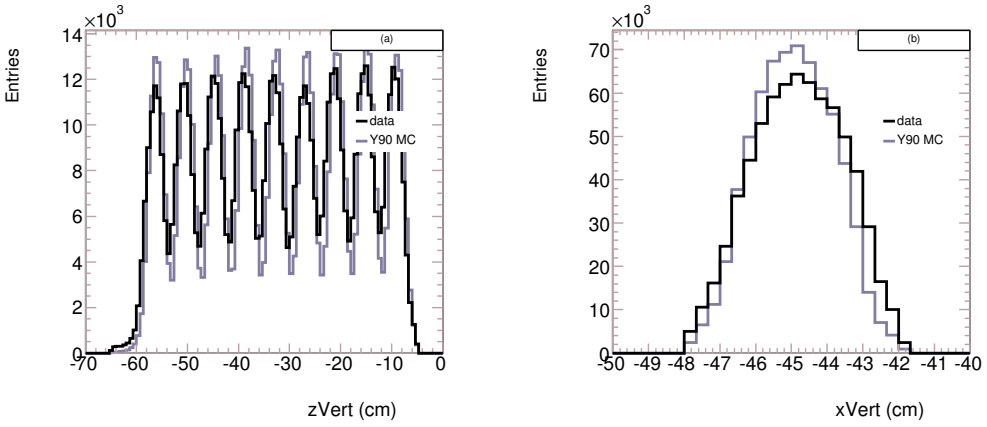

Figure 8.13: Plots of (a) Z vertex, (b) X vertex (data and ^{90}Y) showing the misalignment between the data and MC of the ^{48}Ca discs in the detector 1e channel.

8.4.3 The 1e1γ Channel

The preselection cuts for the electron in the 1e1γ channel are the same as in the 1e channel in Sec. 7.4.1. For the gamma the preselection cuts are the same as those discussed in Sec. 7.4.2, with no additional cuts on the energy. The minimum distance between the vertex and the scintillator (for both the electron and gamma) is 50 cm. With a maximum of two scintillator hits, only isolated scintillator hits from the gamma are selected.

Following on from the previous section, it was thought that with the reduced dominance of ^{90}Y in this channel, any localised areas of internal contamination might be seen. Fig. 8.14 is a background subtracted plot of the Z vertex vs sector for this channel, showing the contamination is uniformly distributed throughout the discs. Although there are no hotspot areas, internal contamination is still likely and cannot be ruled out.

The preselection plots in Fig. 8.15 show the same low energy discrepancy between data and MC as in the 2e channel. After subtracting all the expected background from the data events, the residual plot in Fig. 8.16 shows there is an excess below 1.5 MeV, and any attempt to introduce an additional background (such as ^{40}K) to describe the 1e1γ spectra was found to be inconsistent with the 1e channel activity

measurements. The residual plot gives the motivation for a cut in the 2e channel on the electron sum energy of 1.5 MeV and reduces the systematic error due to the uncertainty on the background.

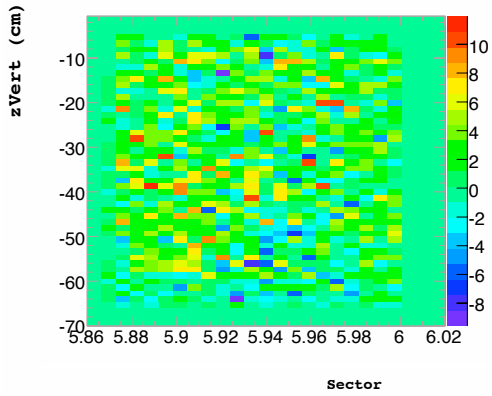

Figure 8.14: Z vertex vs sector background subtracted plot for the 1e1γ channel.

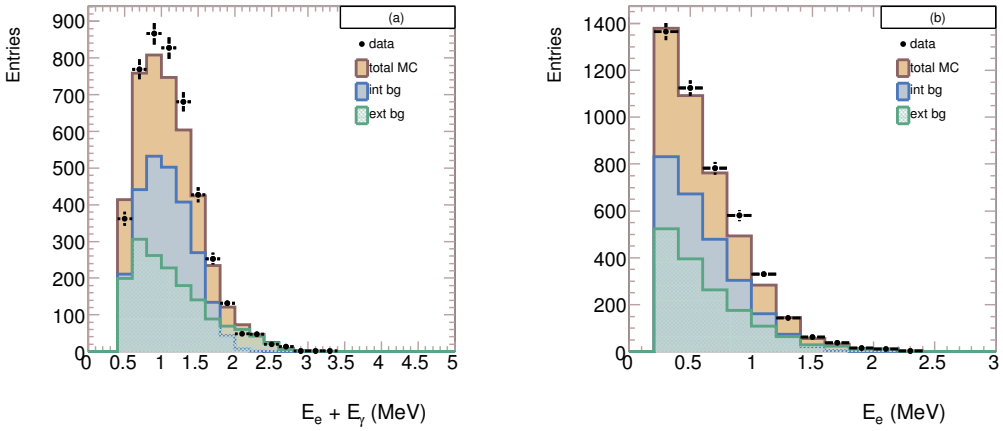

Figure 8.15: 1e1γ preselection plots: (a) Total energy, (b) Single electron spectrum.

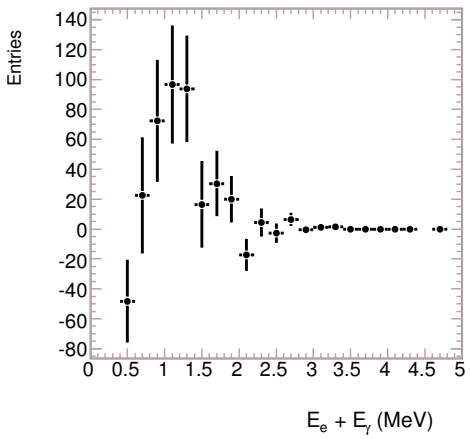

Figure 8.16: 1e1γ residual plot after subtraction of all expected backgrounds.

8.4.4 Final Selection Cuts in the 2e Channel

There are two main cuts that are considered for the final selection analysis. Firstly the ^{90}Y contamination is suppressed by selecting all data and MC events with a $\cos\theta_{ee} < 0$. This cut has already been discussed in Sec. 8.4.1.

Secondly, it has also been shown in previous sections of this thesis, that there is a consistent problem with the description of the background below 1.5 MeV in both the 2e and 1e1γ channels, showing there is an internal background that cannot be identified. It is possible that the 1e channel may have provided some answers, but the channel is clearly dominated by the ^{90}Y contamination, and it is not possible to resolve different backgrounds at this low energy. Therefore the electron sum energy is cut at 1.5 MeV, which in the case of ^{48}Ca is not that limiting as it has a high $Q_{\beta\beta}$ value.

In addition to the preselection cuts, these two cuts yield 133 data events and 17.13 expected background events. The efficiency from the MC is 3.3%. Using Eq. 7.15 in Sec. 7.6, this gives a half-life of

$$T^{2\nu}_{1/2} = 4.44^{+0.49}_{-0.40}(stat.) \times 10^{19} \text{ yrs}$$

The systematic error is discussed in Sec. 8.5 and the final half-life result with this

error is given in Sec. 8.6. The final selection plots for the $2\nu\beta\beta$ decay of ^{48}Ca are shown in Fig. 8.17. In these plots the $2\nu\beta\beta$ ^{48}Ca MC is normalised to the half-life given above.

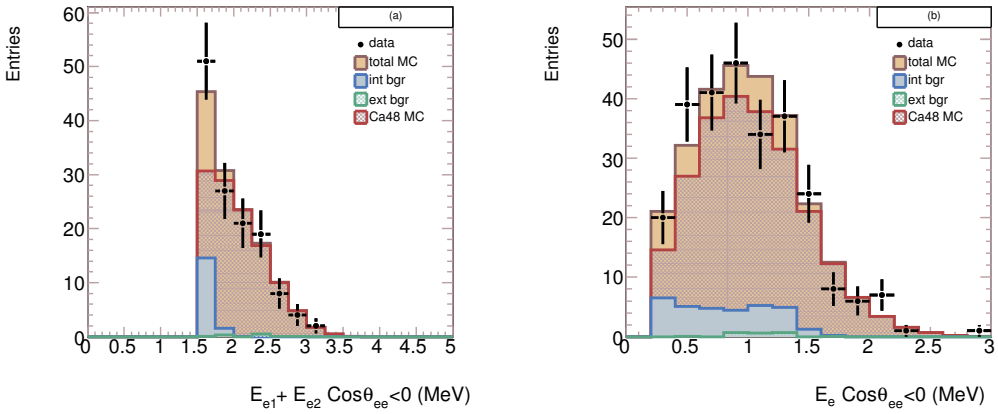

Figure 8.17: 2e channel final selection plots ($\cos\theta_{ee} < 0$ and $E_{e1} + E_{e2} > 1.5$ MeV): (a) Electron sum spectrum, (b) Single electron spectrum.

8.5 Systematic Error Analysis

The following is a breakdown of all the errors and uncertainties attributed to the systematic error.

- The uncertainty due to the ^{90}Y activity measurement is 1.7%. This will be discussed further in Sec. 8.5.1
- The uncertainty in the X vertex is found to be 2.5% and in the Z vertex, 0.5%. This is estimated by comparing half-life results after changing the position of the ^{48}Ca discs in the final analysis program, based on the plots shown in Fig. 8.13.
- The uncertainty in the enrichment of ^{48}Ca is 2.2%.

Further contributions to the systematic error come from estimations made by the NEMO 3 analysis team and published in a previous work [154]. The contributions are:

- 5% from the error on the efficiency calculation due to the inaccuracy of the GEANT simulation and the tracking program. It is found by measuring the activity of calibration sources.

- 2% from the uncertainty in the energy calibration coefficients. This is estimation from the variation in the energy scale of the data.

This gives the overall systematic error of 6.57%.

As the ^{90}Sr contamination is such a dominant feature of the ^{48}Ca analysis, the systematic error on the background is taken from the measurement of the ^{90}Y activity. Verification of the ^{90}Y activity measurement using an independent source is possible as there are three special ^{90}Sr calibration runs.

8.5.1 ^{90}Sr Calibration Runs

The ^{90}Sr calibration runs were carried out in July 2004. The calibration tubes in sectors 6 and 16 were used for this purpose. Table 8.5 lists the sources, their measured activities, and their orientation inside the detector. The activities were measured in May 2003 using an HPGe detector with an accuracy of 12.5%. The uncertainty in these measurements is used to estimate the systematic error on the ^{90}Y activity in the ^{48}Ca foil, which is then propagated through to find a systematic error of 1.7% on the background for the ^{48}Ca $2\nu\beta\beta$ decay analysis.

Source	Activity (Bq)	Detector Position
198	40 ± 5	Sector 6
199	31 ± 4	Sector 16

Table 8.5: ^{90}Sr source activities measured by an HPGe detector and source positions in the NEMO 3 detector.

It is also possible to verify the accuracy of the ^{90}Y MC with these runs. Taking into account the time elapsed since the HPGe measurements and the calibration runs, the expected activities can be calculated using

$$A = A_0 e^{-\Delta T ln2/T_{1/2}}. \tag{8.1}$$

With $\Delta T = 1.2\,\text{yrs}$ and $T_{1/2} = 28.78\,\text{yrs}$, the expected activities of the two sources are $A^{exp}(198) = 38.94 \pm 4.87(syst.)\,\text{Bq}$ and $A^{exp}(199) = 30.18 \pm 3.77(syst.)\,\text{Bq}$. These can now be compared to activities measured in the 1e channel.

The preselection criteria described in Sec. 7.4.1 is used for this analysis. The precise location of the sources within the detector also needs to be determined. The Z vertex and sector positions (azimuthal position of the sources in the detector) of each of the sources are shown in Fig. 8.18 and Fig. 8.19 respectively, with arrows highlighting the cuts on these parameters. There is a discrepancy between the data and MC most noticeable in Fig. 8.19, which may be because of the uncertainty in the geometrical description of the calibration tube, or possibly due to the description of the shape of the ^{90}Y distribution in the MC.

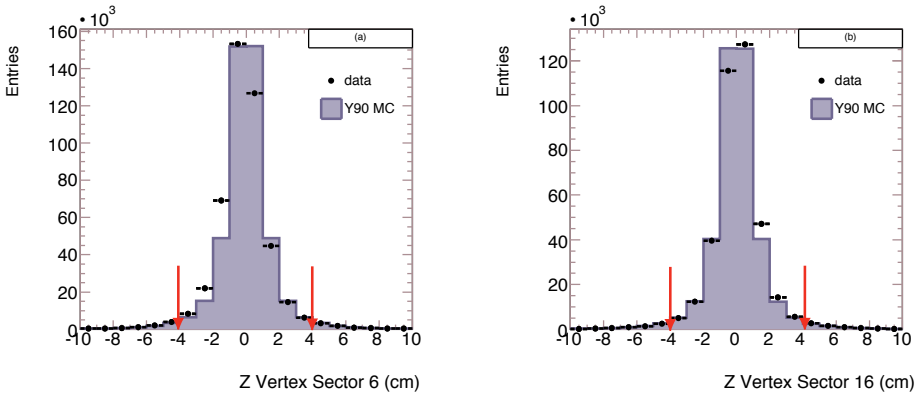

Figure 8.18: Z vertex positions for sectors 6 and 16.

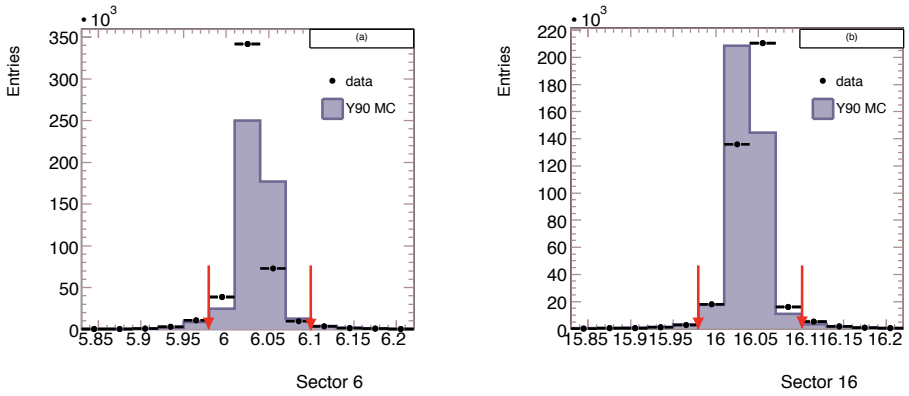

Figure 8.19: Sector (azimuthal) positions for sectors 6 and 16.

The total experimental time for the three runs is 39448 s and the activities for each of the sources are as follows

$$A(198) = 36.98 \pm 0.05(stat.) \pm 4.62(syst.)\text{Bq}$$

$$A(199) = 28.76 \pm 0.05(stat.) \pm 3.60(syst.)\text{Bq}.$$

The results are in good agreement with the expected activities. The spectra for these measurements are shown in Fig. 8.20. There is a small discrepancy between the data and expected background in the low energy region for both spectra, this is not due to backgrounds as the total events found in other areas of the detector total about 1% of the data. It may be that the 1e spectrum shape in the MC is not fully understood, and although it may contribute, it is not large enough to fully explain the discrepancy found in the ^{48}Ca 1e channel.

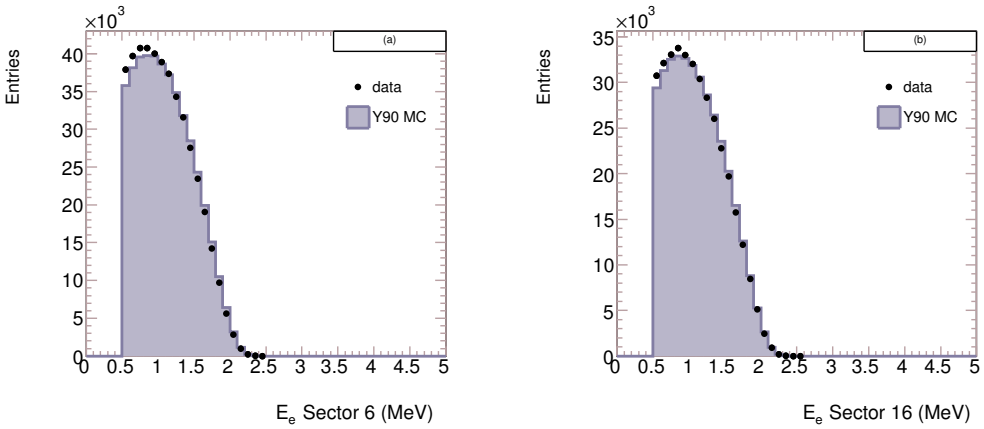

Figure 8.20: 1e spectra for the special ^{90}Sr calibration runs for (a) source 198 in sector 6 and (b) source 199 in sector 16.

8.6 Final Results

The final result with the systematic error for the measurement of the ^{90}Y activity in the ^{48}Ca foil is,

$$A(^{90}Y) = 1695 \pm 2(stat.) \pm 212(syst.) \text{ mBq/kg}.$$

The half-life result with the systematic error for the $2\nu\beta\beta$ decay of ^{48}Ca to the ground state is,

$$T^{2\nu}_{1/2} = 4.44^{+0.49}_{-0.40}(stat.) \pm 0.29(syst.) \times 10^{19} \text{ yrs}.$$

Using the phase space value $G = 4.0 \times 10^{-17}\,\text{yrs}^{-1}$ [141] and the half-life result above, the NME for the $2\nu\beta\beta$ decay of ^{48}Ca to the ground state is

$$M_{2\nu} = 0.024 \pm 0.002.$$

8.7 Search for the $0\nu\beta\beta$ decay of ^{48}Ca

For this search for the $0\nu\beta\beta$ decay of ^{48}Ca, the preselection criteria mentioned in Sec 7.4.1 were used and the energy interval $(E_{e1} + E_{e2}) > 2\,\text{MeV}$ was investigated. The backgrounds listed in Table 8.3 were taken into account, as well as the $2\nu\beta\beta$ decay of ^{48}Ca, this being the main background consideration. Fig. 8.21 shows the electron sum spectrum above 2 MeV with the MC of expected backgrounds and $0\nu\beta\beta$ signal.

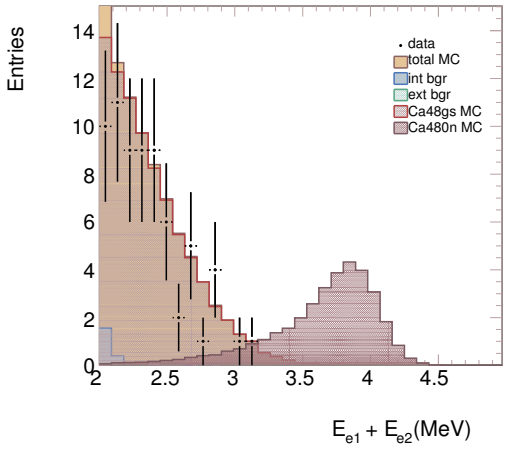

Figure 8.21: Plot of the electron sum spectrum above 2 MeV, showing no data events in the energy region of interest. The $0\nu\beta\beta$ decay spectrum is normalised to a half-life of 1×10^{21} yrs.

There were no events above the expected background and therefore a lower limit on the half-life was set using the MCLIMIT method described in [142]. The limit was calculated using the ROOT implementation of the CL_s method, the TLimit package [143]. Both the hypotheses of signal-plus-background (CL_{s+b}) and background only (CL_b) were used to compute the Modified Frequentist confidence level CL_s, which is the ratio $CL_s = CL_{s+b}/CL_b$. The signal is scaled until the CL_s reaches 90%.

This gave the upper limit on $0\nu\beta\beta$ events of 2.5. The detector efficiency is calculated to be 22% from the MC, which gives the lower bound on the ^{48}Ca $0\nu\beta\beta$ decay half-life of

$$T^{0\nu}_{1/2} > 1.3 \times 10^{22} \text{ yrs (90\% C.L.)}$$

Using the NME of 0.72 [144], the corresponding limit on the neutrino mass is $\langle m_\nu \rangle < 23\,\text{eV}$.

8.8 Summary and Discussion

The half-life of the $2\nu\beta\beta$ decay of ^{48}Ca to the ground state of ^{48}Ti has been measured using the NEMO 3 detector, $T^{2\nu}_{1/2} = 4.44^{+0.49}_{-0.40}(stat.) \pm 0.29(syst.) \times 10^{19}$ yrs which is the world's most precise measurement of this process to date. In fact it is a factor of four more accurate than the previous results given in [138] and [139]. The NME for this process was also calculated to be $M = 0.024 \pm 0.002$. The precision of this experimentally measured NME has important implications for nuclear model theory as now, with the increase in accuracy, different theories can be verified. The two most recent calculations for the ^{48}Ca $2\nu\beta\beta$ decay transition NME are given in [145] and [146], each representing different implementations of the shell model. With increasing computing power the shell model calculations are seen as the most reliable for the near future [76], and as mentioned in Sec. 8.1, ^{48}Ca offers an almost ideal test bench for these studies as it is a doubly magic nucleus.

The calculated NME results from the papers referenced above for the $2\nu\beta\beta$ ^{48}Ca $\rightarrow^{48}$Ti ground state transition are $0.051\,\text{MeV}^{-1}$ [145] and $0.054\,\text{MeV}^{-1}$ [146]. These results converted into units of electron masses (the units of the experimental result given here) are 0.026 and 0.028 respectively. The experimental result of 0.024±0.002 is in good agreement. This is a very encouraging result, as previous calculations differed from experimental values by a factor of two or more.

A limit on the $0\nu\beta\beta$ decay was also obtained, $T^{0\nu}_{1/2} > 1.3 \times 10^{22}$ yrs (90% C.L.), which is comparable to the previous value obtained by ELEGANT VI of $T^{0\nu}_{1/2} > 1.4 \times 10^{22}$ yrs (90% C.L.) [104] and gives the same limit on the neutrino mass of $\langle m_\nu \rangle < 23\,\text{eV}$.

Chapter 9

$2\nu\beta\beta$ decay of ^{100}Mo to the 0_1^+ Excited State

9.1 Introduction and Previous Experiments

As already mentioned in Sec 4.2 the dependence of the NME on the g_{pp} is different for all modes of $\beta\beta$ decay, so the study of the excited states (0_1^+ and 2^+) of isotopes such as ^{100}Mo probes different areas of the QRPA nuclear model than that of the decay to the ground state, or $0\nu\beta\beta$ decay. It was originally thought the $2\nu\beta\beta$ decay to the 2^+ excited state is very strongly suppressed, and that because of this, experiments would never reach the sensitivity required to detect it [86], [147], but there is now some evidence the suppression of this transition may not be as large as previously thought. Half-lives for some isotopes (including ^{100}Mo) may be in the region of (10^{22} - 10^{23}) yrs [141], [148], and so it may be possible for future experiments to detect this mode. NEMO 3, however, has not reached the sensitivity needed to see this process. As already mentioned in Sec. 7.2, the data studied in this analysis is from Phase 1 with run status 1.

9.1.1 Event Topology for the $\beta\beta$ Decay of ^{100}Mo to the 0_1^+ Excited State

Although the decay to excited states is less likely than the ground state decay because of the reduced phase space, it has a very distinct signature, and with NEMO 3

we are able to carry out the study of this decay using the complete topological signature for the first time. The topology of the 0_1^+ excited states decay is two electrons with a $Q_{\beta\beta}$ of 1904 MeV and two γ-rays one with energy 539.53 keV and the other with energy 590.37 keV. The decay scheme is shown below in Fig. 9.1.

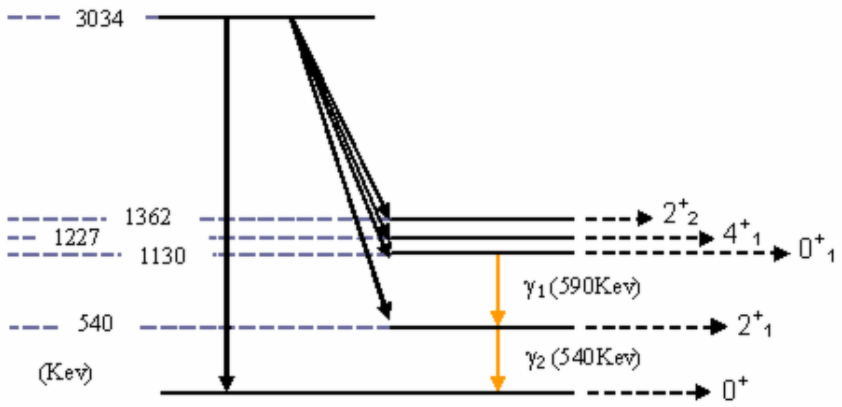

Figure 9.1: Decay scheme for ^{100}Mo.

9.1.2 Previous Experiments

The idea for detecting the $2\nu\beta\beta$ decay to the 0_1^+ excited state of ^{100}Mo was first proposed in 1990 [149]. An experiment followed shortly in the same year [150], which used a low background HPGe detector, built for measuring ultralow activities for isotopes such as ^{238}U. The detector contained 310 g of ^{100}Mo enriched to 98%. It was surrounded by an active anti-coincidence shield, which consisted of a NaI detector, and plastic scintillators. It was not shielded from cosmic rays as the experiment was carried out at sea level, and although the experiment did not obtain a positive result, it was the first to put a limit on the process of $T_{1/2}^{2\nu}(0^+ \rightarrow 0_1^+) > 4.2 \times 10^{19}$ yrs. Fig. 9.2 shows two of the spectra taken for the experiment with the absence of a peak at 539 keV.

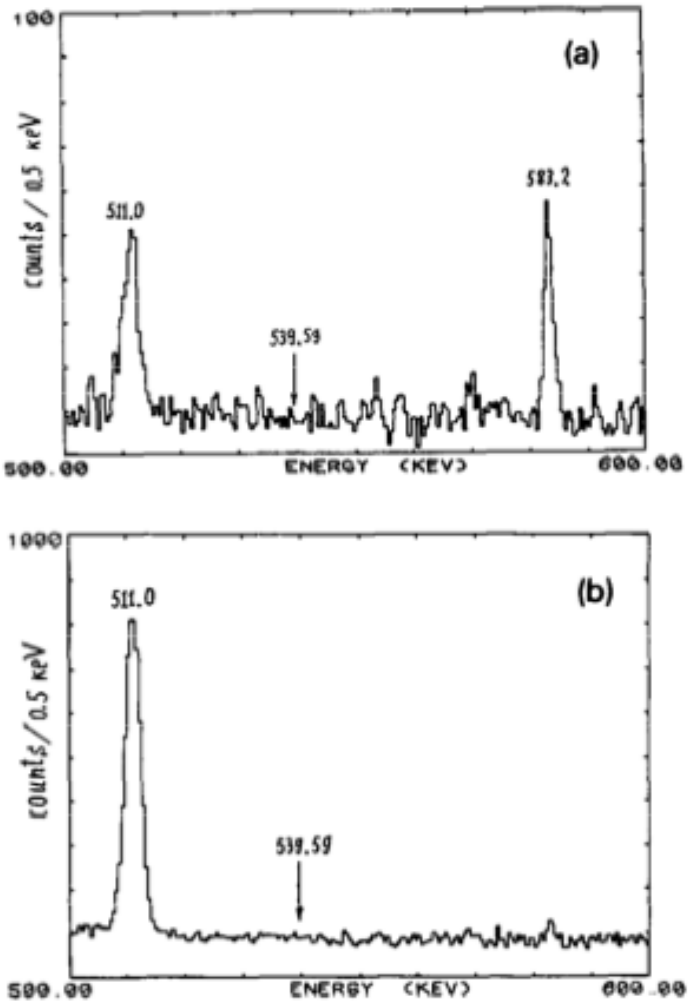

Figure 9.2: Spectra from the ^{100}Mo sample of the 1990 experiment carried out by A. Barabash and coworkers. (a) HPGe detector in anti-coincidence with the NaI detector and plastic scintillators. (b) HPGe detector in anti-coicidence with the plastic scintillators [150].

Five years later, the first positive result was recorded by A. S. Barabash and colleagues [151]. The detector was situated at the Soudan Mine in Minnesota at the depth of 2090 mwe (thus giving the required shielding from cosmic rays). The 956 g of powdered metallic ^{100}Mo was contained in a Marinelli beaker. This is a cylindrical beaker with a hole at one end for the HPGe detector. The Marinelli beaker and HPGe detector were surrounded by a cryostat consisting of low-background

copper components, all of the detector components were then surrounded by a thick lead shield. They obtained the half-life result of $T^{2\nu}_{1/2}(0^+ \rightarrow 0^+_1) = 6.1^{+1.8}_{-1.1} \times 10^{20}$ yrs (68% C.L.). Fig 9.3 shows the spectra from this experiment, with clear signals from the 539.53 and 590.37 keV 0^+_1 excited state gammas.

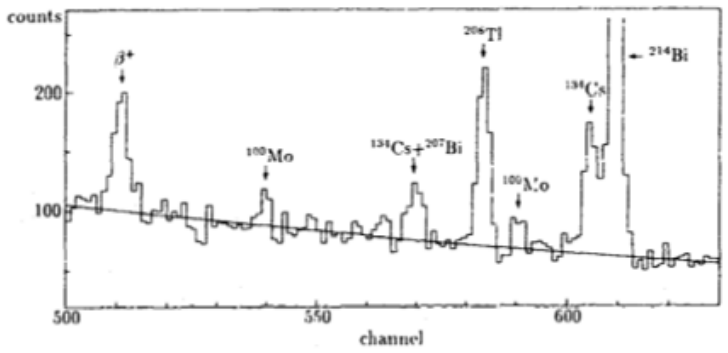

Figure 9.3: Spectra from the ^{100}Mo sample of the 1995 experiment [151].

Since then two more experiments have obtained positive results. The Modane experiment [152] used samples of powdered metallic ^{100}Mo enriched for the NEMO 3 experiment. The samples were measured using low-background HPGe detectors of varying volumes. 17 measurements were taken, with the final result of $T^{2\nu}_{1/2}(0^+ \rightarrow 0^+_1) = 7.6^{+1.6}_{-1.1} \times 10^{20}$ yrs calculated with a systematic error of 15%.

In 2001, the TUNL (Triangle University Nuclear Laboratory) experiment [153] used a new method which did not require the detector to be housed deep underground. The technique was to use two detectors to simultaneously detect the two excited state γ-rays. A 1.05 kg disc of ^{100}Mo (enriched to 98.4%) was sandwiched in between two HPGe detectors with an NaI detector as an active veto shield. This was then surrounded by a thick shield of lead bricks. The spectra are shown in Fig. 9.4 and after 440 days, 22 events were detected giving a half-life of $T^{2\nu}_{1/2}(0^+ \rightarrow 0^+_1) = 5.9^{+1.7}_{-1.1}(stat.) \pm 0.6(syst.) \times 10^{20}$ yrs.

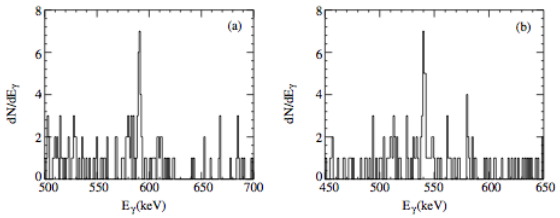

Figure 9.4: Spectra from the ^{100}Mo sample of the TUNL experiment, (a) with 540 ± 2.5 keV and (b) with 591 ± 2.5 keV [153].

9.1.3 NEMO 3 and the Excited States Decay

Although the energy resolution of NEMO 3 is a somewhat limiting factor in the excited states decay measurement, the ability to discriminate against backgrounds using particle identification is a distinct advantage over the HPGe detectors. In fact NEMO 3 holds a unique place in the history of these excited states measurements, as it is the only detector to date that is able to detect the two excited state electrons and obtain an energy sum spectrum and single energy spectrum from them, as well as the sum spectrum and single spectrum of the two gammas and angular distributions.

9.2 Background Estimation

For the excited states analysis the main backgrounds come from:

- $2\nu\beta\beta$ decay of ^{100}Mo ground state to ground state.
- The internal and external background from ^{214}Bi and ^{208}Tl (from different sources including radon in the tracking chamber).

There are two different methods that are used to estimate the background for the ^{100}Mo excited states analysis. The first method, the *MC method*, which uses MC simulations to estimate the contributions from measured backgrounds, and the second method, the *non-Mo method*, is a proportional method based on event analysis in foils not containing ^{100}Mo.

9.2.1 MC Method of Background Estimation

For the MC method analysis, previously measured background activities are used to obtain expected background events. The external background sources are discussed in Sec. 6.2 and the background model for this is in Sec. 7.5 with the activities for the separate background components. Some of the activities of the internal backgrounds were measured with HPGe detectors and are listed in Table 9.1 along with activities found by the NEMO 3 detector.

Background	**Foil Type**	**Activity (mBq/kg)**	**HPGe (mBq/kg)**
^{228}Ac	Composite	0.319	< 0.3
^{228}Ac	Metallic	0.256	< 0.5
^{212}Bi	Composite	0.319	
^{212}Bi	Metallic	0.256	
^{214}Bi	Composite	0.050	< 0.34
^{214}Bi	Metallic	0.104	< 0.39
^{234m}Pa	Composite	9.200	
^{234m}Pa	Metallic	16.500	
^{211}Pb	Composite	8.100	
^{211}Pb	Metallic	12.300	
^{214}Pb	Composite	0.050	< 0.34
^{214}Pb	Metallic	0.104	< 0.39
^{207}Tl	Composite	8.100	
^{207}Tl	Metallic	12.300	< 0.10
^{208}Tl	Composite	0.115	< 0.11
^{208}Tl	Metallic	0.092	
^{100}Mo (gs)	/	0.125	

Table 9.1: Activities measured by NEMO 3 and by HPGe detectors of the internal backgrounds in the ^{100}Mo source foils.

Table 9.2 lists the background components with more than 0.1 events after preselection cuts (see Sec. 7.4.1 for the preselection criteria for electrons and Sec. 7.4.2 for photons (the threshold energy for the single electron and electron sum energy is 0.1 MeV, instead of 0.2 MeV) with the relevant number of generated events, efficiency and number of expected events. Table 9.3 lists the background components with more than 0.1 events after the final selection cuts discussed in Sec. 9.3.

We can see from both Table 9.2 and 9.3 that the main background sources are from radon on the surface of the Geiger wires and surface of the source foils. As already discussed in Sec. 6.2 these radon events are characterised by alphas emitted from ^{214}Po. During the event selection process alphas are tagged and rejected. For the final analysis 8 alpha type data events are rejected.

Background	**Generated Events**	**Efficiency**	**Expected Events**
^{214}Bi sfoil	$5.55e^{+07}$	$3.06e^{-05}$	10.29 ± 1.03
^{214}Bi swire	$1.23e^{+08}$	$2.66e^{-06}$	45.69 ± 4.17
^{208}Tl swire	$1.00e^{+08}$	$1.41e^{-05}$	1.14 ± 0.05
^{214}Bi air	$4.38e^{+10}$	$3.72e^{-10}$	7.50 ± 3.06
^{214}Bi pmt	$2.60e^{+10}$	$3.14e^{-09}$	3.37 ± 1.94
^{208}Tl pmt	$2.38e^{+10}$	$2.63e^{-09}$	5.06 ± 1.06
^{60}Co iframe	$5.00e^{+09}$	$3.80e^{-09}$	5.54 ± 2.09
^{228}Ac intbgr (com)	$2.00e^{+06}$	$8.15e^{-06}$	0.42 ± 0.17
^{214}Bi intbgr (com)	$4.00e^{+05}$	$4.07e^{-05}$	0.33 ± 0.13
^{208}Tl intbgr (com)	$1.00e^{+06}$	$3.58e^{-04}$	6.61 ± 0.58
^{228}Ac intbgr (met)	$2.00e^{+06}$	$9.5e^{-06}$	0.18 ± 0.07
^{214}Bi intbgr (met)	$2.00e^{+06}$	9.50^{-05}	0.72 ± 0.09
^{208}Tl intbgr (met)	$2.00e^{+06}$	$1.55e^{-04}$	0.72 ± 0.09
^{100}Mo gs	$6.00e^{+06}$	$1.81e^{-06}$	6.50 ± 3.25

Table 9.2: Background components which give more than 0.1 events after preselection cuts. The total number of selected expected background events is 94.42 ± 17.81 compared to a total of 268 data events.

Background	Generated Events	Efficiency	Expected Events
^{214}Bi sfoil	$5.55e^{+07}$	$5.48e^{-06}$	1.84 ± 0.21
^{214}Bi swire	$1.23e^{+08}$	$4.43e^{-07}$	7.61 ± 1.70
^{214}Bi air	$4.38e^{+10}$	$6.20e^{-11}$	1.25 ± 1.25
^{208}Tl pmt	$2.38e^{+10}$	$3.43e^{-10}$	0.66 ± 0.38
^{208}Tl intbgr (com)	$1.00e^{+06}$	$1.36e^{-05}$	0.25 ± 0.11
^{214}Bi intbgr (met)	$2.00e^{+06}$	$1.36e^{-05}$	0.10 ± 0.03
^{208}Tl intbgr (met)	$2.00e^{+06}$	$1.49e^{-05}$	0.10 ± 0.03

Table 9.3: Background components which give more than 0.1 events after final selection cuts. The total number of background events is 11.88 ± 3.73 compared to 57 data events.

9.2.2 Non-Mo Method of Background Estimation

Because the decay to the excited states of some of the isotopes inside NEMO 3 (such as ^{nat}Te, ^{130}Te, ^{82}Se, and ^{116}Cd) can be neglected as their mass inside the detector is much lower than that of ^{100}Mo, events from these isotopes, and also the copper foils, can be used to estimate the background for the ^{100}Mo excited states decay.

Internal events contributing to the 2e2γ channel from these 'non-Mo' foils is negligible (this is estimated from MC simulations of the internal backgrounds) so all data events in these sectors are presumed to be external background events. The events selected from the non-Mo foils are then scaled. There are several ways to do this: scaling proportionally to the foil surfaces (i.e. just by a simple ratio of sectors) or scaling using the contribution to the background from radon for each foil, or scaling using the contribution from all external backgrounds.

Using this method means that the MC is indirectly taken into account, and so the systematic uncertainty is lower than for the MC method. This is the great advantage of this method, although the downside is that the accuracy is limited because of the low statistics in the non-Mo foils.

9.3 Final Selection Cuts (MC Method)

The final selection cuts on the electrons and photons are given in Table 9.4. A cut on the cosine of the angle between the two photons ($\cos\theta_{\gamma\gamma}$) is considered first as there is an excess of data events with respect to the MC at small angles shown in Fig. 9.5. These small angle events could be from 2e1γ events, where the photon re-scatters off the scintillator and is detected by a neighbouring scintillator. The re-scattering of photons is not modeled well in the MC, so $\cos\theta_{\gamma\gamma}$ is cut at 0.9 to reduce this uncertainty. The preselection plots before the cut on $\cos\theta_{\gamma\gamma}$ are shown in Fig. 9.6, and show that there is a discrepancy between data and MC at high energies for all the energy spectra. The preselection plots after the cut on $\cos\theta_{\gamma\gamma}$ are shown in Fig. 9.7 with the final selection cuts highlighted with arrows. The cuts on the energies of the electrons and photons are essentially loose cuts based on the knowledge of the ^{100}Mo excited states decay scheme. The fit of these plots has improved with the $\cos\theta_{\gamma\gamma}$ cut, although there is still some discrepancy between data and MC at high energies in both of the gamma spectra.

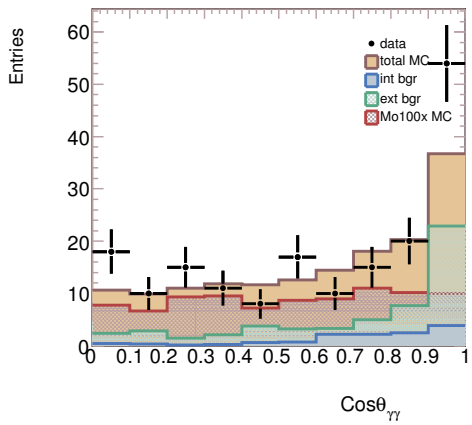

Figure 9.5: Preselection plot (MC method) of $\cos\theta_{\gamma\gamma}$ showing an excess of data events with respect to the MC near $\cos_{\gamma\gamma} = 1$.

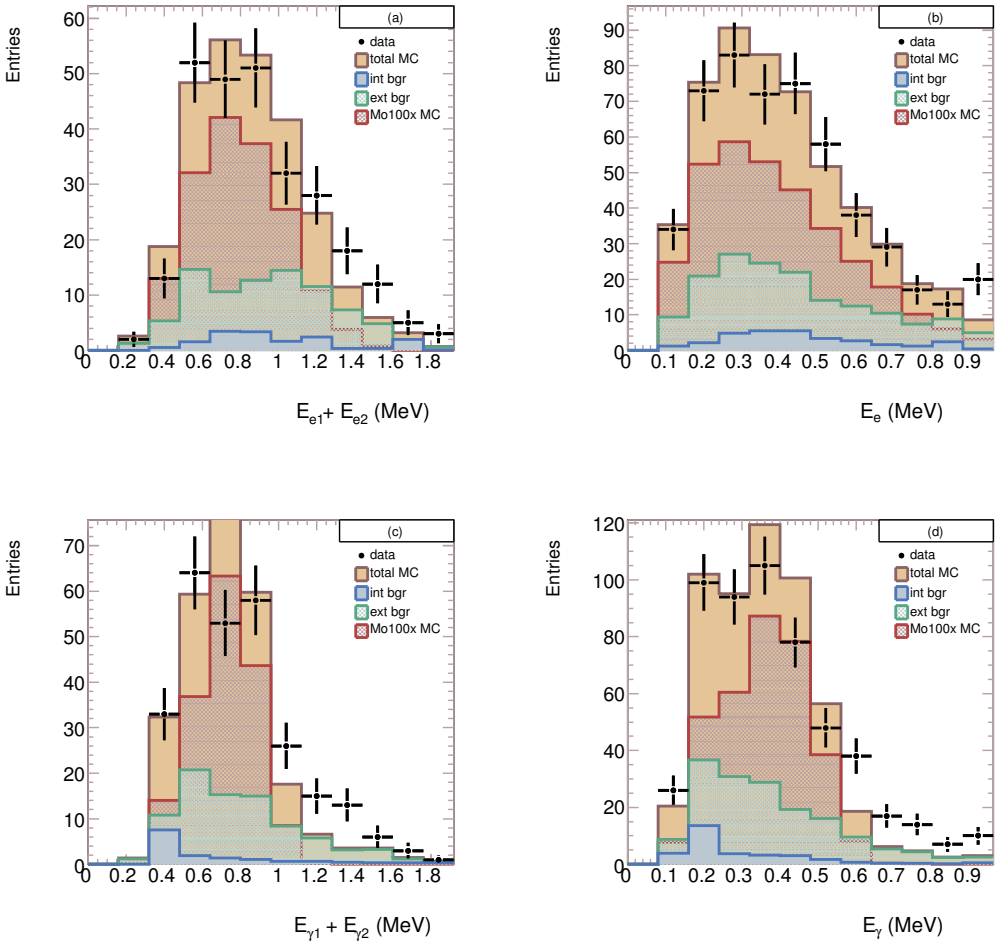

Figure 9.6: Preselection spectrum plots before the cut on $\cos\theta_{\gamma\gamma}$ of: (a) the electron sum energy (b) the single electron energy (c) the gamma sum energy (d) the single gamma energy (MC method). The ^{100}Mo excited states MC is normalised to the number of signal events.

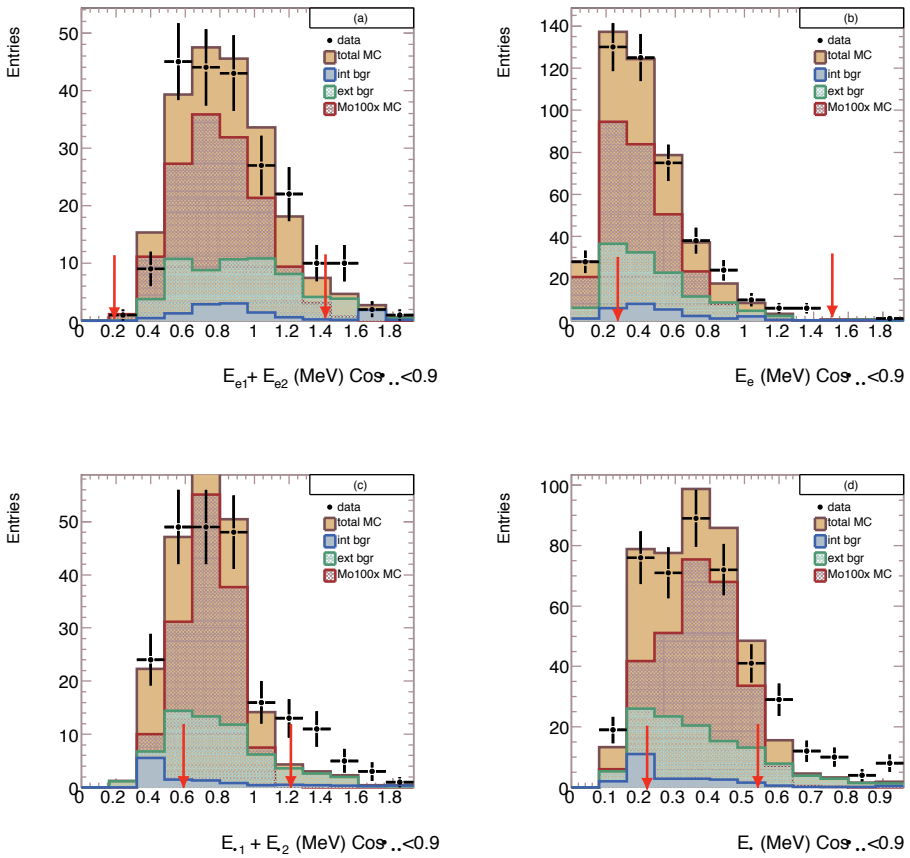

Figure 9.7: Preselection spectrum plots after the cut on $\cos\theta_{\gamma\gamma}$ of: (a) the electron sum energy (b) the single electron energy (c) the gamma sum energy (d) the single gamma energy (MC method). The final energy cuts are highlighted with arrows. The ^{100}Mo excited states MC is normalised to the number of signal events. The total number of expected background events is 69.58±13.41 compared to 217 data events.

Parameter	Min	Max
E_e	0.22 MeV	1.5 MeV
E_{ee}	0.2 MeV	1.4MeV
E_γ	0.22 MeV	0.55MeV
$E_{\gamma\gamma}$	0.6MeV	1.2MeV
$\cos_{\gamma\gamma}$	-1.0	0.9

Table 9.4: Summary of final selection energy and kinematic cuts.

After the preselection and final energy and kinematic cuts the excited states MC is normalised to the number of signal events and the number of decays extracted from the normalised MC. The number of observed events is 57 and 11.89 ± 3.73 background events were selected. From Eq. 7.15 the result for the $2\nu\beta\beta$ $0^+ \rightarrow 0_1^+$ excited states decay of ^{100}Mo for Phase 1 is then

$$T_{1/2}^{2\nu} = 5.70^{+1.15}_{-0.82}(stat.) \times 10^{20}\,\text{yrs}$$

The plots of the angular distributions are in Fig. 9.8 and the spectra of the electron and gamma energies after all cuts are shown in Fig. 9.9 and .

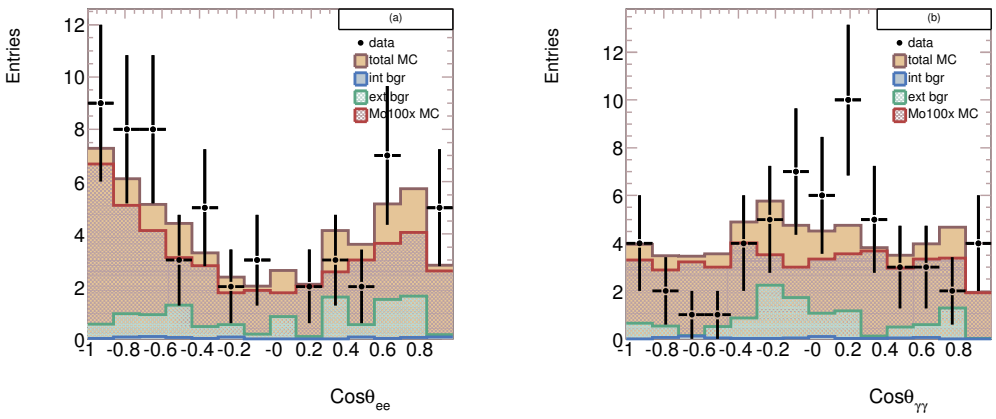

Figure 9.8: Plots of: (a) $\cos_{ee}$ and (b) $\cos_{\gamma\gamma}$ after all cuts (MC method).

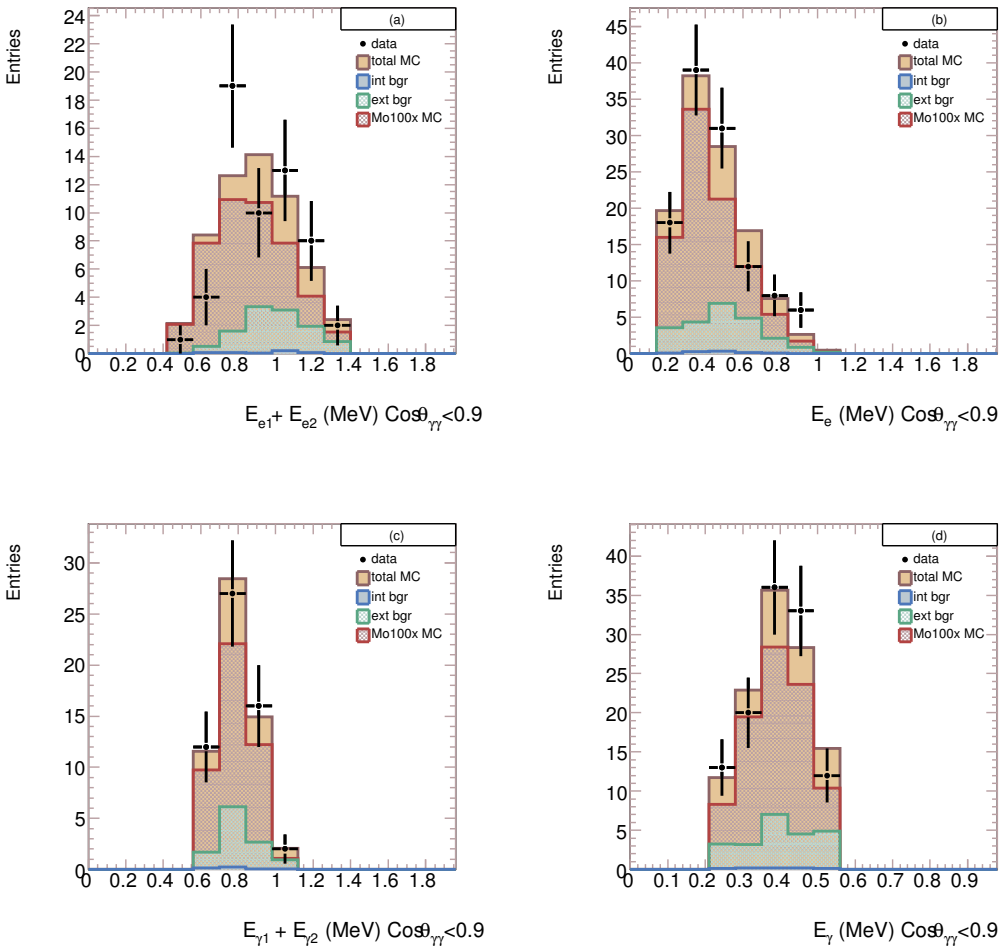

Figure 9.9: Energy spectrum plots after all cuts of: (a) the electron sum energy (b) the single electron energy (c) the gamma sum energy (d) the single gamma energy (MC method). The excited states MC is normalised to the number of signal events in these plots.

9.4 Final Selection Cuts (Non-Mo Method)

Figs. 9.11 and 9.10 show the preselection plots for events in the non-Mo sectors. These show a reasonable agreement between data and MC although statistics are a limiting factor. After all cuts (preselection and final selection) there are 7 events in the non-Mo foils. Using the radon background ratio these non-Mo events are scaled to 8.77 ± 3.32 external background events and using the sector ratio the events are scaled to 10.50 ± 3.97 external background events. Subtracting the number of scaled background events from the total number of data events (57) the $2\nu\beta\beta$ $0^+ \rightarrow 0_1^+$ excited states decay half-life of ^{100}Mo is then calculated from Eq. 7.15, which gives $T_{1/2} = 5.33^{+1.07}_{-0.77}(stat.) \times 10^{20}$ yrs for the radon ratio and $T_{1/2} = 5.53^{+1.19}_{-0.83}(stat.) \times 10^{20}$ yrs using the sector ratio. A more detailed breakdown of results is shown in Table 9.5 which lists the number of expected events and corresponding half-life for the different scaling methods of the radon background ratio and sector ratio. Fig. 9.12 show the energy spectra of the electrons and gammas after all cuts. Although the agreement between data and MC is good, it is difficult to make comments, good or bad, as again the statistics in these plots are very low.

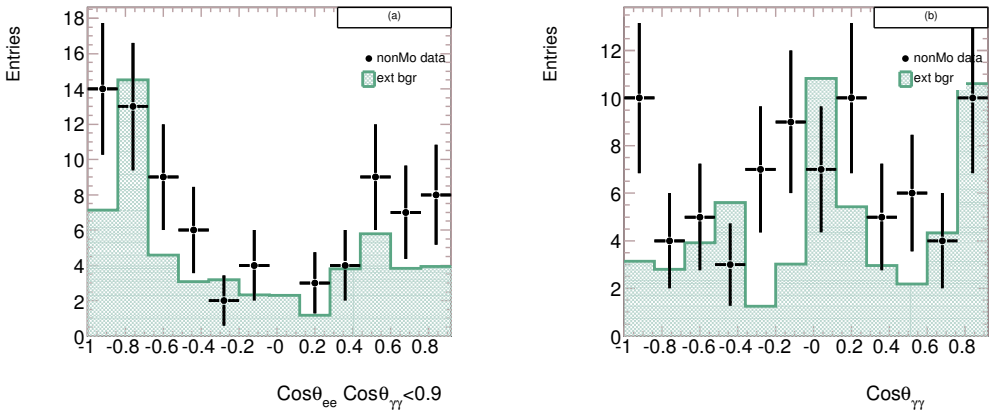

Figure 9.10: Preselection plots in the non-Mo sectors of: (a) $\cos_{ee}$ and (b) $\cos_{\gamma\gamma}$.

It is also possible with NEMO 3 analysis tools to view the Non-Mo data events in event displays, one of these events is shown in Figs 9.13 and 9.14. As there are so few data events, this is a viable way of checking the events have the correct topological criteria.

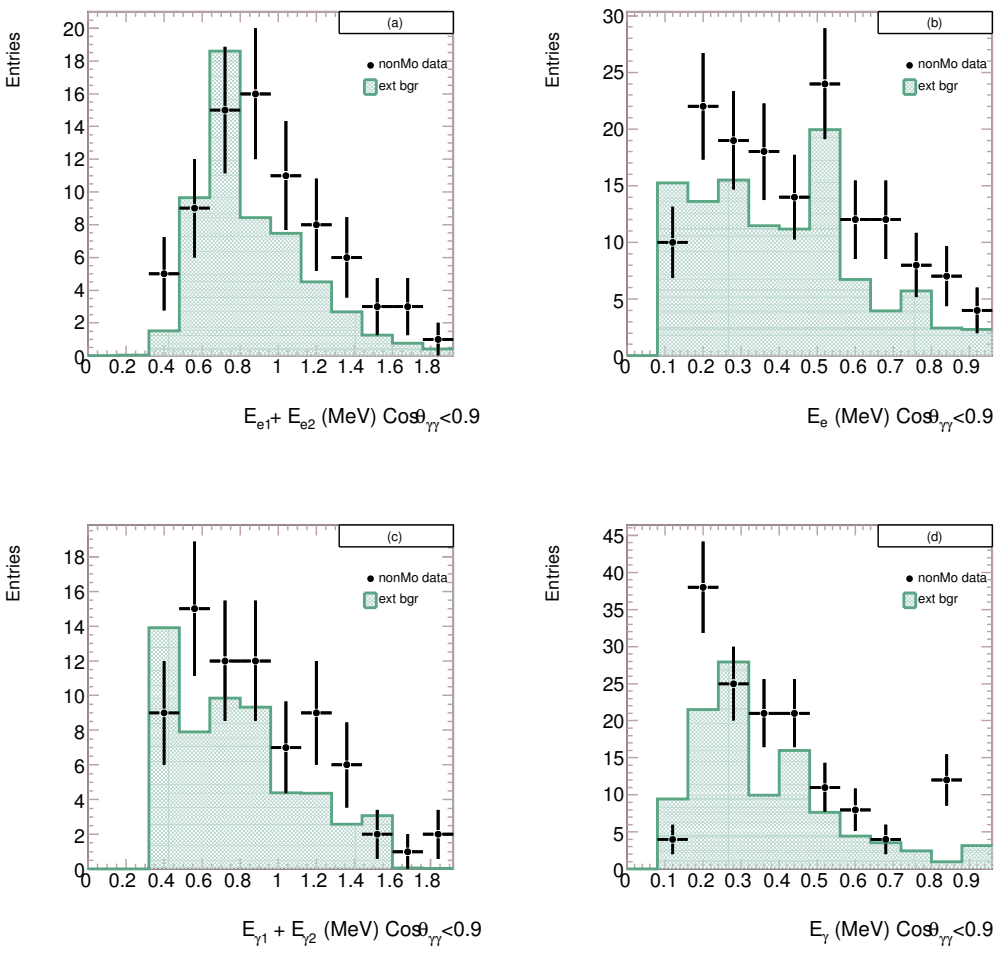

Figure 9.11: Preselection energy spectrum plots in the non-Mo sectors of: (a) the electron sum energy (b) the single electron energy (c) the gamma sum energy (d) the single gamma energy.

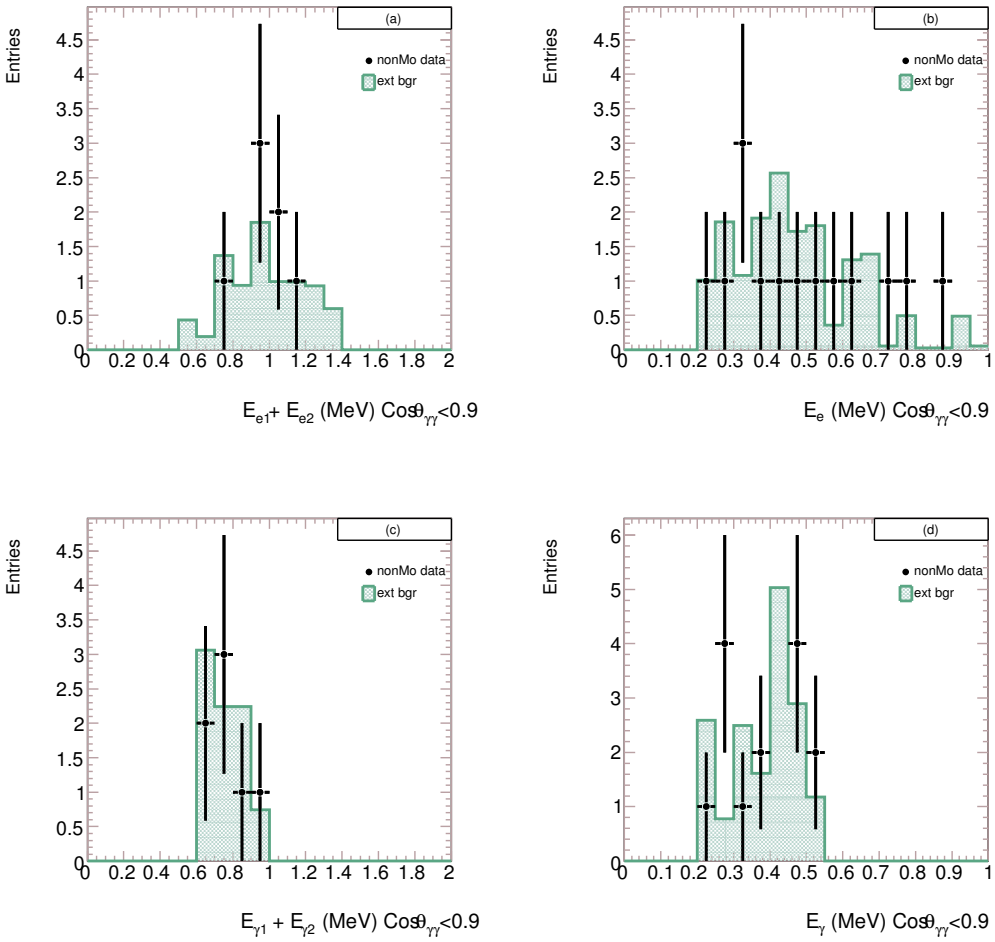

Figure 9.12: Final selection spectrum plots in the non-Mo sectors of: (a) the electron sum energy (b) the single electron energy (c) the gamma sum energy (d) the single gamma energy.

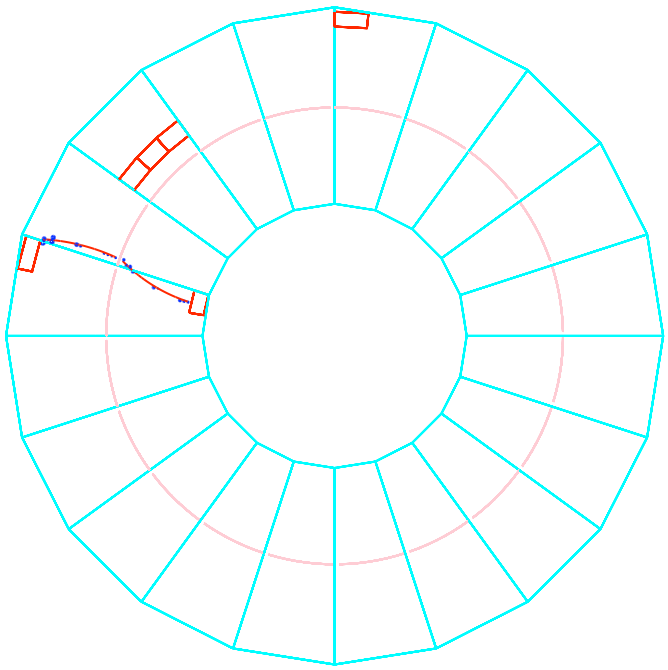

Figure 9.13: Top view of non-Mo event run number: 2053 event number: 59390. The event display clearly shows the two electron tracks coming from the source foils and their associated scintillator hits, and two other isolated scintillator hits from the two photons.

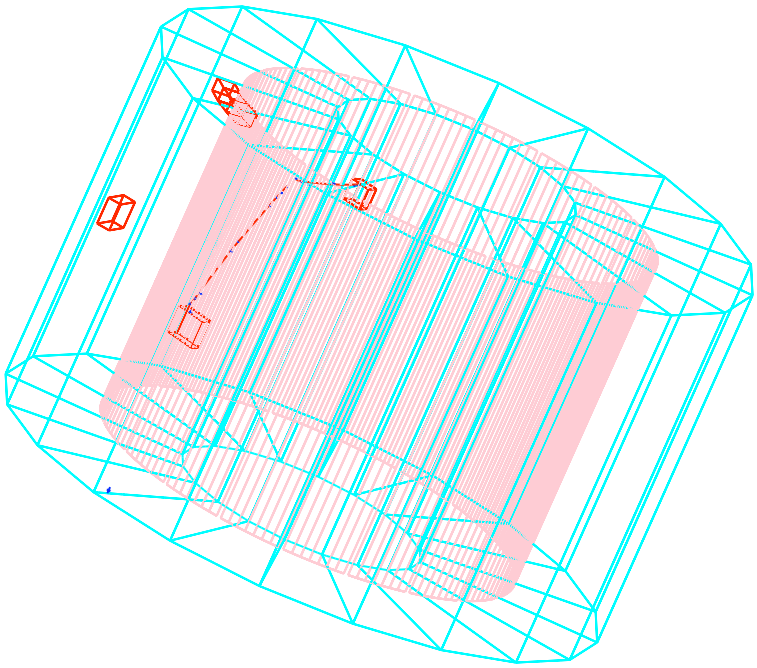

Figure 9.14: 3D view of a non-Mo event, run number: 2053 event number: 59390.

9.5 Systematic Errors

The systematic errors for this analysis have been studied in depth by the NEMO 3 analysis team [154]. The main contributions are:

- 5% from the error on the efficiency calculation due to the inaccuracy of the GEANT simulation and the tracking program. It is found by measuring the activity of calibration sources.
- 10% from the error on the efficiency calculation from the inaccuracy of the GEANT simulation of γ-rays.
- 2% from the uncertainty in the energy calibration coefficients. This is an estimation from the variation in the energy scale of the data.
- 4% from the simulation of the thin source foils. This is calculated from a comparison of results between the metallic and composite ^{100}Mo source foils.

- 6% from the uncertainty of the radon level inside the detector. This portion of the systematic error is only included in the overall systematic error for the MC method. Contributions to the error from other backgrounds are negligible.

The total systematic error for the MC method is ∼13.5% and for the non-Mo method ∼12.0%. For the non-Mo method the systematic error on the MC is taken into account with the scaling methods discussed in Sec. 9.4 and as a second order effect, the systematic error is $< 1\%$.

9.6 Final Half-Life and Nuclear Matrix Element Results

After 332 days of data taking (only runs with run status=1 were selected) a total of 57 data events were selected. For the MC method 11.89 ± 3.73 background events were selected. The efficiency from the MC is 9.78×10^{-4}. The half-life result for the $2\nu\beta\beta$ of ^{100}Mo to the 0_1^+ excited state is,

$$T_{1/2}^{2\nu} = 5.70^{+1.15}_{-0.82}(stat.) \pm 0.77(syst.) \times 10^{20}\,\text{yrs} \tag{9.1}$$

The values obtained with the non-Mo method are given in Table 9.5.

The nuclear matrix element for this transition can be calculated using Eq. 4.10,

$$M^{2\nu}(0_1^+) = \frac{1}{\sqrt{T_{1/2}^{2\nu}(0_1^+)G^{2\nu}(0_1^+)}} \tag{9.2}$$

where $G^{2\nu}(0_1^+)$ in this case is $1.64 \times 10^{-19}\,\text{yrs}^{-1}$. Using the half-life obtained from the MC method, the matrix element for this transition is $M^{2\nu}(0_1^+) = 0.103 \pm 0.016$.

Method	**Bgr**	**S/B**	**Efficiency**	**Half-life ($\times 10^{20}$ yrs)**
Non-Mo method (radon)	8.77 ± 3.32	5.49	9.78×10^{-4}	$5.33^{+1.07}_{-0.77}(stat.) \pm 0.64(syst.)$
Non-Mo method (sector)	10.50 ± 3.97	4.43	9.78×10^{-4}	$5.53^{+1.19}_{-0.83}(stat.) \pm 0.66(syst.)$

Table 9.5: Non-Mo method final results with systematic error.

9.7 Discussion

For the first time the 0_1^+ excited state decay half-life of ^{100}Mo has been measured using the complete topological signature of two electrons and two γ-rays. All useful kinematic information of the decay has been obtained (also for the first time) with sum spectra, single spectra and angular distribution of the two electrons and two γ-rays. The results given here are in good agreement with the previous results given in Sec. 9.1.2.

The value here can be compared to theoretical predictions, which for the QRPA model are in the region of 10^{20} yrs - 10^{21} yrs ($(1.3-5.4)\times10^{19}$ yrs [141], 2.1×10^{21} yrs [155], and 10^{21} yrs [156]), which shows this experimental result is in agreement to within 30% of the NME calculation from [156], and puts constraints on certain models. Furthermore a relatively recent calculation of the $2\nu\beta\beta$ excited states decay half-life of ^{100}Mo was carried out using the single state dominance hypothesis (SSHD) [148], [157] and the EC transition of ^{100}Tc $\rightarrow^{100}$Mo [158]. The result of $T_{1/2}(0^+ \rightarrow 0_1^+) = 4.2\times10^{20}$ yrs [159] is in good agreement with the result given here. The accuracy of the calculation is $\pm$50% (which is due to the accuracy of the calculation on the EC transition). If this was improved, then a comparison between experimental and theoretical results would give a better insight into the SSDH transition.

The NME calculated here can be compared to the NME of the ground state transition, also obtained by the NEMO 3 detector. $M^{2\nu}(g.s.) = 0.126\pm0.005$ (using $T^{2\nu}_{g.s.} = 7.11\pm0.02(stat.)\pm0.06(syst.)\times10^{19}$ yrs and $G^{2\nu}(g.s.) = 8.9\times10^{-18}\,\text{yrs}^{-1}$ [160]). This shows a $\sim$20% difference in the results. This difference in results becomes an important factor in terms of the SSDH transition, and will be studied more closely in future measurements made by NEMO 3.

The results from the two different methods of determining the background contribution in the non-Mo sectors of the detector are in good agreement within errors. If the only contribution to the background is from radon then the results from using the radon ratio should be considered, however there may be contributions from other external background sources which would be proportional to the foil thickness and area. The larger the foil area, the larger the external background contribution and ^{100}Mo has the largest foil proportion inside the detector. If we also compare

the results from the MC and non-Mo methods we can see that they are also in good agreement, showing a good control of the systematics associated with the backgrounds. We can see from this analysis that radon is the dominant background, therefore analysis of the Phase 2 data should give us a better description of the process. This analysis will be done in the next few years by the NEMO 3 collaboration.

Although it is true that the decay to excited states has a lower probability than that of the ground state decay, it has a more distinct topological signature, as there are two photons emitted in coincidence with the two electrons, this means we could potentially have a background free experiment which detects topological signatures (like SuperNEMO). Then the $0\nu\beta\beta$ decay to the excited states could be studied in more detail as a way of singling out mechanisms involved in the process.

Chapter 10

Summary and Conclusions

NEMO 3 is a $\beta\beta$ decay experiment located under the Alps in the LSM, which is based in the Fréjus Tunnel linking France and Italy. It has been running since February 2003, and since that time has been routinely taking data. The NEMO 3 collaboration has produced some of the most competitive and sensitive $\beta\beta$ decay results to date for many of the isotopes housed inside the detector, including the $\beta\beta$ decay of ^{48}Ca to the ground state and the $2\nu\beta\beta$ decay of ^{100}Mo to the 0_1^+ excited state, which are the main focus of this thesis.

The backdrop to the main analysis in this thesis is a description of the history and theory behind the neutrino, which outlines the importance of all the past, present and future neutrino experiments, in which the $0\nu\beta\beta$ decay searches have their own unique role in completing the description of the elusive neutrino.

A comprehensive account of the NEMO 3 detector is given, describing the main parts of the detector: calorimeter, tracking chamber, source foils and shielding. A description of the backgrounds associated with the experiment, which play such an important role in this type of low energy experiment, is also presented. An outline of the topological signatures of electrons, positrons, α-particles and photons is given, which distinguishes NEMO 3 from other current experiments, and provides a powerful tool for background rejection, and also a unique insight into different modes of $\beta\beta$ decay. The external background model is also discussed. These sections of the thesis provide a solid foundation for the main analyses.

Two isotopes are studied: ^{48}Ca and ^{100}Mo. Each analysis has its own topological

signature and offers different challenges.

For the ^{100}Mo analysis, the external background from radon is a main consideration, along with the limitations imposed by the resolution of the scintillators in the energy region of the two excited states γ-rays, which is reflected in the loose nature of the final selection cuts.

For ^{48}Ca the topological signature of the two electrons from the ground state decay is less of a challenge. It was the internal contamination from ^{90}Sr that hindered this analysis, as well as the limitations of the NEMO 3 detector resolution at low energies. Both of the final selection cuts reflect these two considerations.

Finally the half-life result for the $2\nu\beta\beta$ decay of ^{100}Mo to the 0_1^+ excited states is:

$$T_{1/2}^{2\nu}(0^+ \rightarrow 0_1^+) = 5.70^{+1.15}_{-0.82}(stat.) \pm 0.77(syst.) \times 10^{20}\,\text{yrs},$$

For the first time the topological signature of this decay has been used to obtain half-life results. The corresponding matrix element is

$$M^{2\nu}(0_1^+) = 0.103 \pm 0.016.$$

For the $2\nu\beta\beta$ decay of ^{48}Ca to the ground state:

$$T_{1/2}^{2\nu} = 4.44^{+0.49}_{-0.40}(stat.) \pm 0.29(syst.) \times 10^{19}\,\text{yrs},$$

which is the most precise measurement of the half-life of this decay process in the world. The corresponding NME is

$$M^{2\nu} = 0.024 \pm 0.002.$$

Both $2\nu\beta\beta$ decay half-life results from ^{48}Ca and ^{100}Mo give the most precise measurements of the NME to date, providing vital constraints for NME calculations which can then be used for extracting new physics from $0\nu\beta\beta$ decay.
The $0\nu\beta\beta$ decay limit for ^{48}Ca is

$$T_{1/2}^{0\nu} > 1.3 \times 10^{22}\ \text{yrs (90\%C.L.)},$$

giving the corresponding limit on the neutrino mass of $\langle m_\nu \rangle < 23\,\mathrm{eV}$, which is at the level of the best previous result in [104].

Bibliography

[1] D. O. Caldwell (Ed), *Current Aspects of Neutrino Physics*, Berlin: Springer, 2001

[2] M. Goeppert-Mayer, *Phys. Rev.* **48** (1935) 512

[3] E. Majorana, *Nuovo Cimento* **14** (1937) 171

[4] G. Racah, *Nuovo Cimento* **14** (1937) 322

[5] W. H. Furry, *Phys. Rev.* **56** (1939) 1184

[6] H. Primakoff, *Phys. Rev.* **85** (1952) 888

[7] F. Reines and C.L. Cowan, Jr, *Phys. Rev.* **92** (1953) 830

[8] F. Reines and C.L. Cowan, Jr, *Phys. Rev.* **113** (1959) 273

[9] B. Pontecorvo, *J. Exptl. Theoret. Phys.* **33** (1957) 549, *J. Exptl. Theoret. Phys.* **34** (1958) 247

[10] Z. Maki, M. Nakagawa, and S. Sakata, *Prog. Theor. Phys.* **28** (1962) 870

[11] G. Danby et al., *Phys. Rev. Lett* **9** (1962) 36

[12] F. Reines et al., *Phys. Rev. Lett.* **15** (1965) 36

[13] C. V. Acher et al., *Phys. Rev.* **18** (1965) 196

[14] R. Davis, D.S. Harmer and K.C. Hoffman, *Phys. Rev. Lett.* **20** (1968) 1205

[15] R. Becker-Szendy et al., *Phys. Rev. D* **46** (1992) 3720

[16] Y. Fukuda et al., *Phys. Lett. B* **335** (1994) 237

[17] K. S. Hirata et al., *Phys. Rev. Lett.* **63** (1989) 16

[18] K. S. Hirata et al., *Phys. Rev. Lett.* **58** (1987) 1490

[19] K. S. Hirata et al., *Phys. Rev. D* **38** (1988) 448

[20] R. M. Bionta et al., *Phys. Rev. Lett.* **58** (1987) 1494

[21] E. N. Alekseev et al., *Phys. Lett. B* **205** (1988) 209

[22] M. Aglietta et al., *Eur. Phys. Lett* **3** (1988) 1315

[23] G. S. Abrams et al., *Phys. Rev. Lett.* **63** (1989) 2173

[24] D. Decamp et al., *Phys. Lett. B* **235** (1990) 399

[25] Y. Fukuda et al., *Phys. Rev. Lett* **81** (1998) 1562

[26] K. Kodama et al., *Phys. Lett. B* **504** (2001) 218

[27] Q. R. Ahmed et al., *Phys. Rev. Lett.* **87** (2001) 071301

[28] K. Eguchi et al., *Phys. Rev. Lett.* **90** (2003) 021802

[29] T. Araki et al., *Phys. Rev. Lett.* **94** (2005) 081801

[30] M. Fukugita and T. Yanagida, *Phys. Lett. B* **174** (1986) 45

[31] M. Gell-Mann, P. Raymond, and R. Slansky, in Proc *Supergravity*, ed. P. van Neiuwenhuizen, and D. Z. Freeman, North Holland, 1979, p. 315

[32] T. Yanagida, *Prog. Theor. Phys.* **64** (1980) 1103

[33] J. N. Abdurashitov et al., *Phys. Rev. Lett.* **77** (1996) 4708

[34] W. Hampel et al., *Phys. Lett. B* **447** (1999) 127

[35] Y. Fukuda et al., *Phys. Rev. Lett* **81** (1998) 1158

[36] Q. R. Ahmed et al., *Phys. Rev. Lett.* **89** (2002) 011301

[37] B. Aharmin, *Phys. Rev. C* **72** (2005) 055502

[38] M. Apollonio et al., *Phys. Lett. B* **466** (1999) 415

[39] S. A. Dazeley, hep-ex/0510060v1

[40] F. Adrellier et al., hep-ex/0405032

[41] K. Nakajima et al., hep-ex/08014589

[42] G. Barr et al., *Phys. Rev. D.* **39** (1989) 3532

[43] M. Honda et al., *Phys. Lett. D* **52** (1995) 4985

[44] V. Agraval et al., *Phys. Rev. D* **53** (1996) 1313

[45] T. Haines et al., *Phys. Rev. Lett.* **57** (1986) 1986

[46] M. Aglietta et al., *Eur. Phys. Lett.* **8** (1989) 611

[47] C. Berger et al., *Phys. Lett. B* **227** (1989) 489

[48] W. W. M. Allison et al., *Phys. Lett. B* **449** (1999) 137

[49] M. Ambrosio et al., *Eur. Phys. J* **36** (2004) 323

[50] Y. Ashie et al., *Phys. Rev. Lett.* **93** (2004) 10181

[51] J. Altegoer et al., *Nucl. Instrum. Meth. A* **404** (1998) 96

[52] E. Eskut et al., *Nucl. Instrum. Meth. A* **401** (1997) 7

[53] G. Drexlin et al., *Prog. Nucl. Part. Phys.* **32** (1994) 351

[54] C. Athanassopoulos et al., *Phys. Rev. Lett.* **81** (1998) 1774

[55] A. A. Aguilar-Arevalo et al., hep-ex/08064201v1

[56] A. A. Aguilar-Arevalo et al., *Phys. Rev. Lett.* **98** (2007) 231801

[57] K. Nakamura et al., *Nucl. Phys. Proc. Suppl.* **91** (2001) 203

[58] M. H. Ahn et al., *Phys. Rev. Lett.* **96** (2003) 181801

[59] D. G. Michael et al., *Phys. Rev. Lett.* **97** (2006) 191801

[60] P. Adamson et al., hep-ex/08662237v1

[61] R. Acquafredda et al., *New J Phys.* **8** (2006) 303

[62] S. Amerio et al., *Nucl. Instrum. Meth. A* **527** (2004) 329

[63] Y. Oyama et al., hep-ex/0512041v2

[64] D. Ayres et al., hep-ex/0503053v1

[65] E. Lisi et al., *Phys. Rev. D* **75** (2007) 053001

[66] S. C. Curran, J. Angus, and A. L. Cockcroft, *Nature* **162** (1948) 302

[67] S. C. Curran, J. Angus, and A. L. Cockcroft, *Phys. Rev.* **76** (1949) 853

[68] C. Kraus et al., *Eur. Phys. J. C* **40** (2005) 447

[69] V. M. Lobashev, *Nucl. Phys. A* **719** (2003) 153

[70] A. Osipowicz et al., hep-ex/0109033

[71] Image of tritium beta decay available at:
http://crio.mib.infn.it/wig/silicini/img.gif/kp.gif

[72] V. M. Lobashev et al., *Phys. Lett.* **460** (1999) 227

[73] C. E. Aalseth et al., *Phys. Rev. D* **65** (2002) 092007

[74] H. Klapdor-Kleingrothaus et al., *Eur. Phys. J. A* **12** (2001) 147

[75] O. Elgaroy and O. Lahov, *J. Cosmol. Astropart. Phys.* **0304** (2003) 004

[76] F.T. Avignone, S.R. Elliot and J. Engel, *Rev. Mod. Phys.* **80** (2008) 481

[77] W. M. Yao et al., *J. Phys. G* **33** (2006) 1, Particle Data Group

[78] Y. Chikashige, R. N. Mohapatra, R. D. Peccei, *Phys. Lett. B* **98** (1981) 265.

[79] A. S. Barabash, *Phys. At. Nucl.* **67** (2004) 438.

[80] J. Schechter and J. Valle, *Phys. Rev. D* **24** (1981) 1883

[81] Ilias main website: http://www-ilias.cea.fr/

[82] J.A. Hableib and R.A. Sorensen, *Nucl. Phys. A* **98** (1967) 542

[83] A.H. Huffman, *Phys. Rev. C* **2** (1970) 742

[84] J. Suhonen, *From Nucleons to Nucleus: Concepts of Microscopic Nuclear Theory*, Berlin: Springer, 2007

[85] P. Vogel and M. R. Zirnbauer, *Phys. Rev. Lett.* **57** (1986) 3148

[86] W. C. Haxton and G. J. Stephenson Jr., *Prog. Part. and Nucl. Phys.* **12** (1984) 409

[87] A. Poves, Ilias 5th Annual Meeting, Jaca, Spain: http://ilias.in2p3.fr/ilias_site/meetings/documents/ILIAS_5th_Annual_Meeting/200208_Poves.pdf

[88] F. Simkovic et al., *Nucl. Phys. A* **766** (2006) 107

[89] S.R. Elliot and P. Vogel, *Ann. Rev. Nucl. Part. Sci.* **52** (2003) 115

[90] V. I. Tretyak and Y. G. Zdesenko, *At. Data Nucl. Data Tables* **80** (2002) 83

[91] A. S. Barabash, nucl-ex/0602009

[92] O. K. Manuel, *J. Phys. G: Nucl. Part. Phys.* **17** (1991) S221

[93] M. G. Inghram and J. H. Reynolds, *Phys. Rev.* **76** (1949) 1265

[94] M. G. Inghram and J. H. Reynolds, *Phys. Rev.* **78** (1950) 822

[95] T. Kirsten, W. Gentner and O. A. Shaeffer, *Z. Phys.* **202** (1967) 273

[96] T. Kirsten and H. W. Müller, *Earth Planet Sci. Lett.* **6** (1969) 271

[97] T. Kirsten et al., *Proc. Nuclear Beta Decay and Neutrinos Osaka* (World Scientific, Singapore, 1986) p.81

[98] S. R. Elliot, A. A. Hahn and M. K. Moe, *Phys. Rev. Lett* **59** (1987) 2020

[99] C.A. Levine, A. Ghiorso and G.T. Seaborg, *Phys. Rev.* **77** (1950) 296s

[100] H. Klapdor-Kleingrothaus et al., *Nucl. Instum. Meth. A* **511** (2003) 341

[101] H. Klapdor-Kleingrothaus et al., *Phys. Lett. B* **586** (2004) 198

[102] H. L. Harney, *Mod. Phys. Lett. A* **16** (2001) 2409

[103] C. E. Aalseth et al., *Phys. Rev. D* **70** (2004) 078302

[104] I. Ogawa et al., *Nucl. Phys. A* **730** (2004) 215

[105] A. S Barabash et al., hep-ex/0610025

[106] F. A. Danevich et al., *Phys. Rev. C* **68** (2003) 03550

[107] T. Bernatowicz et al., *Phys. Rev. C* **47** (1993) 806

[108] C. Arniboldi et al., *Phys. Rev. Lett.* **95** (2005) 142501

[109] R. Bernabei et al., *Phys. Lett. B* **546** (2002) 23

[110] A. S Barabash, *Phys. At. Nucl.* **68** (2005) 414

[111] S. Schönert et al., nucl.ex/0311013

[112] R. Gaitskell et al., *Phys. Rev. D* **70** (2004) 078302

[113] K. Zuber, *Phys. Lett. B* **519** (2001) 1

[114] E. Fiorini and T. Ninikoski, *Nucl. Instum. Meth.* **224** (1984) 2139

[115] C. Arniboldi et al., *Phys. Lett. B* **557** (2003) 167

[116] C. Arniboldi et al., *Phys. Rev. C* **78** (2008) 035502

[117] C. Arniboldi et al., *Nucl. Instrum. Meth. A* **518** (2004) 775

[118] S. Umehara et al., *J. Phys. Conf.* series **39** (2006) 256

[119] M. Chen, *Nucl. Phys. Proc Suppl.* **145** (2005) 65

[120] Y. Takuechi, Presentation at ICHEP 04 (2004)

[121] H. Ejiri et al., *Nucl. Instrum. Meth. A* **164** (1991) 447

[122] H. Ejiri, *Prog. Part. Nucl. Phys.* **57** (2006) 153

[123] N. Ishihara et al., *Nucl. Instrum. Meth. A* **443** (200) 101

[124] M. Danilov et al., *Phys. Lett. B* **480** (2000) 12

[125] Y. Shitov, nucl-ex/0807.3078

[126] R. Arnold et al., *Nucl. Instrum. Meth. A* **536** (2005) 79

[127] D. Dassie et al., *Phys. Rev. D* **51** (1995) 2090

[128] G. Audi and A.H. Wapstra, *Nucl. Phys. A* **595** (1995) 409

[129] Nuclear Database. Masses and Q Values. Retrieved June 7, 2005 from: http://nucleardata.nuclear.lu.se/database/masses.

[130] A. Nachab, *AIP COnf. Proc.* **897** (2007) 35

[131] Y. Takeuchi, et al., *Phys. Lett. B* **452** (1999) 418-424

[132] R. Brun et al., CERN Report CERN DD/EE/84-1 (1984)

[133] O. A. Ponkratenko, V. I. Tretyak and Y. G. Zdesenko, *Phys. At. Nucl.* **63** (2000) 1282

[134] V. Vasiliev, External Background in the NEMO 3 Experiment, http://www.hep.ucl.ac.uk/∼vv/extbgr/

[135] V. Vasiliev, Radon in the NEMO 3 Tracking Chamber, http://www.hep.ucl.ac.uk/∼vv/radon/

[136] E. der Mateosian and M. Goldhaber, *Phys. Rev.* **146** (1966) 810

[137] K. You et al., *Phys. Lett. B* **265** (1991) 53

[138] A. Balysh et al., *Phys. Rev. Lett.* **77** (1996) 5186

[139] V.B. Brudanin et al., *Phys. Lett. B* **495** (2000) 63

[140] F. Filthaut, TFractionFitter Source File, http://root.cern.ch/cgi-bin/print_hit_bold.pl/root/html/src/TFractionFitter.h.html

[141] J. Suhonen and O. Civitarese, *Phys. Rep.* **300** (1998) 123

[142] T. Junk, *Nucl. Instr. and Meth. A* **434** 435

[143] C. Delaere, TLimit Source File,
http://root.cern.ch/cgi-bin/print_hit_bold.pl/root/html/src/TLimit.h.html

[144] E. Caurier et al, *Nucl. Phys. A* **654** (1999) 973c

[145] E. Caurier et al., *Int. J. Mod. Phys. E* **16** (2007) 552

[146] M. Horoi et al., *Phys. Rev. C* **75** (2007) 034303

[147] M. Doi, T. Kotani, E. Takasugi, *Prog. Theor. Phys.* **83** (1985) 1

[148] O. Civitarese and J. Suhonen, *Nucl. Phys. A* **653** (1999) 321

[149] A. S. Barabash, *JETP Lett.* **51** (1990) 207

[150] A. S. Barabash et al., *Phys. Lett. B* **249** (1990) 186

[151] A. S. Barabash et al., *Phys. Lett. B* **245** (1990) 408

[152] A. S. Barabash et al., *Phys. At. Nucl.* **62** (1999) 2039

[153] L. De Braeckeleer et al., *Nucl. Phys. A* **781** (2001) 3510

[154] R. Arnold et al., *Nucl. Phys. A* **781** (2007) 209

[155] S. Stoica and I. Mihut, *Nucl. Phys. A* **602** (1996) 197

[156] A. Griffiths and P. Vogel, *Phys. Rev. C* **46** (1992) 181

[157] J. Abad et al., *Ann. Fis. Ser. A* **80** (1984) 9

[158] A. Garcia et al., *Phys. Rev. C* **47** (1993) 2910

[159] P. Donin et al., *Nucl. Phys. A* **753** (2005) 337

[160] R. Arnold et al., *Phys. Rev. Lett.* **95** (2005) 182302